Carnegie Mellon University

CARNEGIE INSTITUTE OF TECHNOLOGY

THESIS

SUBMITTED IN PARTIAL FULFILLMENT OF THE REQUIREMENTS

FOR THE DEGREE OF Doctor of Philosophy

TITLE Micro-scale Approaches to the Bench-scale Evaluation of CO_2 Capture System Properties

PRESENTED BY Alexander Hallenbeck

ACCEPTED BY THE DEPARTMENT OF

Chemical Engineering

JOHN KITCHIN	4/19/16
JOHN KITCHIN, ADVISOR	DATE
LORENZ BIEGLER	4/19/16
LORENZ BIEGLER, DEPARTMENT HEAD	DATE

APPROVED BY THE COLLEGE COUNCIL

VIJAYAKUMAR BHAGAVATULA	4/19/16
DEAN	DATE

Micro-scale Approaches to the Bench-scale Evaluation of CO_2 Capture System Properties

Submitted in partial fulfillment of the requirements for the degree of

Doctor of Philosophy

Department of Chemical Engineering

Alexander P. Hallenbeck

B.S., Chemical Engineering, University of Delaware

Carnegie Mellon University
Pittsburgh, Pennsylvania

May, 2016

Acknowledgments

The completion of this dissertation is the culmination of a long and rewarding journey, and is something that I could not have accomplished without the assistance of many individuals. I have been very fortunate to have had many influential role models and mentors over the years that have guided me along a path of academic success.

I would like to first thank my parents, David and Kasia, for being my earliest role models and mentors. I am eternally grateful for their support in all my endeavors. As two math professors, they nurtured in me a spirit of intellectual curiosity and encouraged my interest in science and engineering. I would like to also thank my sister, Michelle, for her continuing support and friendship.

I thank the numerous professors that I was fortunate to be taught and mentored by during my undergraduate studies at the University of Delaware. I would like to thank my undergraduate research advisor, Antony Beris, for his support and patience in guiding me as a beginning researcher. I would like to thank professors Antony Beris, Eric Furst, Norman Wagner, and Gilberto Schleiniger for writing letters of recommendation for my graduate school applications and for their advice in my graduate school search that ultimately led me to CMU.

During my time at CMU I've gotten to know many other graduate students and formed several friendships that have greatly enriched my graduate school experience. I thank past Kitchin group members, Rich Alesi, Anita Lee, Ethan Demeter, who, during the early years of my time at CMU, were very helpful and supportive of me as I adjusted to working in the laboratory. Many of the friendships I've formed have extended beyond the academic setting. For example, I'll never forget bicycling from Pittsburgh to

Washington D.C. with John Michael and Jake Boes. I'm very grateful to them and Zhongnan Xu, Matthew Curnan, Yash Puranik, among others for their camaraderie.

I would like to thank my thesis advisor, John Kitchin. He has always been present and eager to help during my time at CMU as I've developed as a researcher. I am very grateful for the numerous conversations we have had that have helped guide the direction of my doctoral work and enhanced my understanding of carbon dioxide capture and the process of scientific research.

I've been fortunate during my thesis work to have had several valuable collaborations. I would like to thank the members of the Anna Lab that have shared their workspace and resources with me and lent their advice in helping me conduct microfluidic experiments. I would like to thank the researchers at NETL that at various points during my doctoral work provided constructive criticism and feedback and experimental resources. I thank Adefemi Egbebi, Kevin Resnik, and David Hopkinson for their help and the use of their laboratory to carry out CSTR absorption capacity measurements.

I thank the department of chemical engineering, the National Energy Technology Laboratory-Regional University Alliance (NETL-RUA), and the Lawrence Livermore National Laboratory (LLNL) for providing the funds necessary to carry out this work. This work would not have been possible without their support.

I also would like to acknowledge and thank all the members of my thesis committee: professors John Kitchin (chair), Shelley Anna, Neil Donahue, and Newell Washburn for the time and effort they put into reviewing this work.

Abstract

The development of cost-effective CO_2 capture and sequestration technologies is likely to play a critical role in mitigating anthropogenic CO_2 emissions linked with global climate change. The identification of improved novel CO_2 capture materials has potential to reduce the costs of both the monoethanolamine post-combustion CO_2 capture process and the Selexol® pre-combustion CO_2 capture process. Determining the efficacy of a CO_2 capture solvent or sorbent necessitates the measurement of a large number of chemical and physical properties. Furthermore, the design space of potential CO_2 capture materials is quite large and includes several classes of materials with a high degree of structural tunability. Within this context, a reduction in the volume and time requirements of the measurement of such variables such as the CO_2 absorption capacity and absorption rate greatly enhances the experimental capability for screening large numbers of potential CO_2 capture materials. The work in this thesis is focused on the application of microfluidic experimental techniques to the characterization of both post-combustion and pre-combustion CO_2 capture solvents.

Post-combustion CO_2 capture systems that are studied include a primary amine-based solid sorbent, alkanolamines such as monoethanolamine and methyldiethanolamine, and aqueous potassium salts of glycine, taurine, proline, and lysine. The SO_2 and O_2 tolerance of a primary amine-functionalized polymeric CO_2 solid sorbent is investigated with a packed bed reactor. The working CO_2 capture capacity of the sorbent was measured over the course of several adsorption/desorption cycles of continuous exposure to simulated flue gas streams. The sorbent exhibited no loss in CO_2 capacity over the course of 17 cycles of adsorption/desorption when exposed to a flue gas stream containing 4% O_2 and no SO_2. However,

irreversible competitive SO_2 adsorption was observed in the presence of 431 ppm SO_2 resulting in a nearly complete loss of CO_2 capacity over the course of only 9 adsorption/desorption cycles.

The absorption capacity and rate of aqueous potassium salts of glycine, taurine, proline, and lysine was measured and compared with monoethanolamine by conducting image analysis of segmented gas plug - liquid slug flow in a microfluidic channel. The microfluidic measurements were shown to be accurate predictions of trends in the CO_2 absorption capacity of the various solvents as measured in a continuously stirred-reactor (CSTR). The potassium salt of lysine exhibited the highest CO_2 absorption capacity, >50% higher than that of monoethanolamine in the microfluidic reactor. The aqueous salt of lysine was compared with monoethanolamine both on a constant molar concentration of amine basis as well as on a constant weight fraction of water basis. The higher CO_2-lysine stoichiometry was offset by the lower molecular weight of monoethanolamine. CSTR equilibrium absorption capacity measurements revealed that although 0.5 M potassium lysinate absorbed more CO_2 than 0.5 M monoethanolamine, 30 wt% monoethanolamine absorbed more CO_2 than 1.48 M potassium lysinate on a moles of CO_2 per gram of absorbent solution basis.

Raman spectroscopy is coupled with a μL-scale silica capillary cell and utilized as a tool for quantitative microfluidic measurement of properties such as CO_2 solubility, H_2 solubility, CO_2 diffusivity, the heat of CO_2 dissolution in a physical solvent, and the heat of CO_2 absorption in an amine solvent. The CO_2 solubility, CO_2/H_2 selectivity, and heat of CO_2 dissolution was measured for a hydrophobic polydimethylsiloxane-polyethylene glycol dimethyl ether hybrid solvent and compared with Selexol®. The CO_2 solubility and CO_2/H_2 selectivity of the hybrid solvent were found to be

comparable with those of Selexol®. The heat of CO_2 dissolution was also determined using Henry's Law constant data and a van't Hoff expression to be lower (less negative) for the hybrid solvent than for Selexol®. This along with the hybrid's hydrophobic nature make it an excellent pre-combustion CO_2 capture candidate as it is well suited for high temperature CO_2 absorption. The CO_2 diffusivity of water and three polydimethylsiloxane derivates was also experimentally measured using similar Raman spectroscopic μL-scale techniques. The method was demonstrated to be capable of estimating the CO_2 diffusivity of a physical solvent within one order of magnitude. Raman spectroscopy and a heated silica capillary cell was also developed based on the traditional Gibbs-Helmholtz equation used for relating vapor-liquid equilibrium measurements with calorimetric data. The heats of absorption were measured for a 30 wt% monoethanolamine aqueous solution and a 27 wt% methyldiethanolamine aqueous solution at various CO_2 loadings. The method is shown to be capable of correctly measuring the difference between the heat of absorption associated with a primary amine-CO_2 reaction and that associated with a tertiary amine-CO_2 reaction. However, a systematic underestimation of the literature heats of reaction for both amines is observed.

Contents

List of Tables

List of Figures

1 Introduction

1.1 The Need for CO_2 capture

Concern over the long-term negative environmental impacts associated with global climate change has grown significantly in recent decades. There has also been an increasing global recognition and alarm over the connection between anthropogenic greenhouse gas, CO_2 in particular, emissions and rising global temperatures.[1] Consequently there has been a large push among the international community for governments to enact CO_2 emissions reduction targets. This environmental concern has been a major driving force behind recent scientific research and public policy regarding energy. Reducing our dependence on fossil fuels for electricity generation has been a major focus of these efforts. In 2013, electricity production was the largest contributing U.S. economic sector to greenhouse gas emissions, constituting 31% of the total 6673 million metric tons of CO_2 equivalent in the United States.[2] Also in 2013, 67.4% of world electricity generation came from either coal, oil, or natural gas, with the largest percentage, 41.3%, coming from coal.[3] A transition away from fossil fuels and towards renewable energy sources such as solar, wind, geothermal, biomass, etc, will involve solving significant technological challenges and is not likely to occur in the short-term future.

In this context, the development of carbon capture and sequestration (CCS) technologies is essential to mitigate CO_2 emissions due to the continued utilization of coal and other fossil fuels for electricity generation while research is conducted to develop renewable energy technologies. In an effort to balance the economic costs of CO_2 capture, the U.S. department of energy (DOE) has defined a target CO_2 capture rate of 90% and a target

increase of the cost of electricity of less than 35% for both new and existing coal-fired power plants.[4] Recent estimates are that CCS will increase the cost of electricity generation by approximately 60-80% at new coal combustions plants.[5] In order to lower the cost of CO_2 capture, scientific research is predominantly divided between three CO_2 capture approaches: post-combustion CO_2 capture, pre-combustion CO_2 capture, and oxy-fuel combustion.[5] Oxy-fuel combustion, not yet available commercially, involves the combustion of the coal with a purified O_2 gas instead of air so that the flue gas produced is free of N_2 and the resulting flue gas is primarily CO_2 and H_2O suitable for compression and sequestration. The research conducted in this dissertation pertains directly to post-combustion and pre-combustion CO_2 capture, both of which are available at a commercial scale and are described in detail below.

1.2 Post-Combustion CO_2 capture

Post-combustion CO_2 capture (PCC) at a pulverized coal (PC) power plant involves the selective separation of CO_2 from the flue gas produced by the combustion of coal and following the removal of other low-concentration pollutants, such as NO_x and SO_x. It is the only CCS approach that can be retro-fitted to existing PC power plants.The typical flue gas stream entering a PCC unit at a PC plant has a nominal gas composition of 12 vol% CO_2, 6% H_2O, 4% O_2, 400 ppm SO_2 and balance N_2.[6] The current state of the art technology for PCC is chemical absorption via an amine solvent, such as monoethanolamine (MEA).[7]

MEA and other amines selectively and reversibly absorb CO_2 through exothermic chemical reactions. Amines and CO_2 react through two main chemical pathways to form either carbamate or bicarbonate depending on

the structure of the amines and the presence or absence of H_2O. Primary and secondary amines preferentially react with CO_2 to form carbamate as can be seen in Equations 1.1 and 1.2. These reactions typically involve rapid kinetics, are limited to a 2 moles of amine per 1 mole of CO_2 stoichiometry, can occur in wet or dry conditions, and possess a large heat of reaction.

$$2RNH_2 + CO_2 \rightleftharpoons RNH_3^+ + RNHCO_2^- \tag{1.1}$$

$$2RR'NH + CO_2 \rightleftharpoons RR'NH_2^+ + RR'NCO_2^- \tag{1.2}$$

A consensus on a single correct mechanism for carbamate formation has not been reached. However, the leading proposed candidates include 2-step carbamic acid formation[8] (Equation 1.3), 2-step zwitterion formation[9,10] (Equation 1.4), and the 1-step termolecular mechanism[11] (Figure 1.1).

$$RNH_2 + CO_2 \rightleftharpoons RNHCO_2H + RNH_2 \rightleftharpoons RNHCO_2^- + RNH_3^+ \tag{1.3}$$

$$RNH_2 + CO_2 \rightleftharpoons RNH_2^+CO_2^- + RNH_2 \rightleftharpoons RNHCO_2^- + RNH_3^+ \tag{1.4}$$

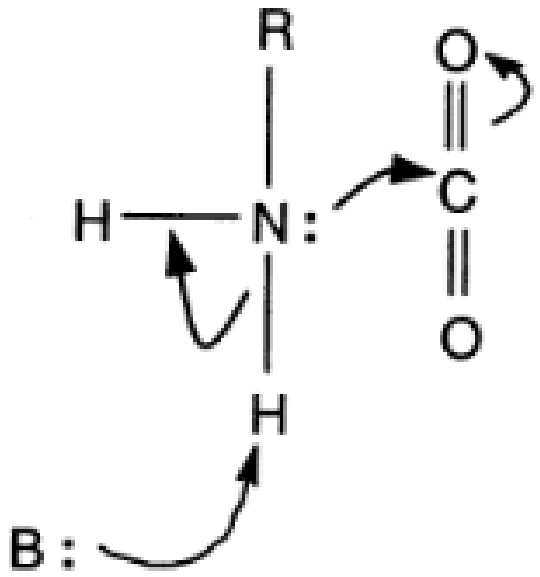

Figure 1.1: Termolecular mechanism for carbamate formation as proposed by Crooks and Donnellan, 1989

Due to steric hindrance and the lack of a N-H bond, sterically hindered amines and tertiary amines do not react with CO_2 to form carbamate, but do react to form bicarbonate (Equation 1.5). In contrast with carbamate formation, the bicarbonate reaction pathway possesses slower kinetics, a lower heat of reaction, requires the presence of H_2O, and is not limited to a 1 mole of CO_2 absorbed per 2 moles of amine stoichiometry. Bicarbonate formation can be mediated by other bases, such as potassium carbonate, as well.

$$RR^{'}R^{"}N + CO_2 + H_2O \rightleftharpoons RR^{'}R^{"}NH^{+} + HCO_3^{-} \tag{1.5}$$

In a typical PCC process the flue gas is cooled to 40-65 °C and contacted in an absorber with an aqueous amine solution with an amine concentration of 30-40 wt% producing a CO_2-rich amine solution that is transferred to a stripper vessel where the CO_2-rich solution is heated to temperatures typically near 130-140 °C which releases a purified gas stream of wet CO_2 for compression

and sequestration and regenerates the amine solution which is recycled back in CO_2-lean form to the absorber.[12] There are several drawbacks to the use of MEA in the PCC process. The high heat of reaction between MEA and CO_2 means that there is a large parasitic energy penalty in order to reverse the MEA-CO_2 reaction. The viscosity and corrosivity of MEA necessitates the dilution of MEA to a 30 wt% aqueous solution, and the high heat capacity of water also contributes to the total parasitic energy penalty of the regeneration process. The absorbent solution gradually loses MEA over time due to MEA's volatility[13] as well as its susceptibility to oxidation[14] and thermal degradation and irreversible reaction with SO_2 to form heat-stable-salts.[14] All of these factors contribute to the costs of PCC. Much of current PCC-research is on identifying substitute solvents that address these drawbacks of MEA and other alkanolamines such as ammonia,[15] aqueous piperazine solutions[16] , promoted carbonate aqueous solutions,[17–19] aqueous amino acid salt solutions,[20–23] and non-aqueous amine-functionalized ionic liquids[24] among other liquid solvents. A significant body of research has been conducted on the use of solid CO_2-sorbents[25] and membrane-based CO_2 capture methods[26] as well.

1.3 Pre-Combustion CO_2 capture

In order to mitigate the CO_2 emissions from the generation of electricity, Integrated Gasification Combined Cycle (IGCC) power plants have been designed and developed as an alternative to the traditional PC power plant. A simplified block flow diagram of the IGCC process can be seen below in Figure 1.2.

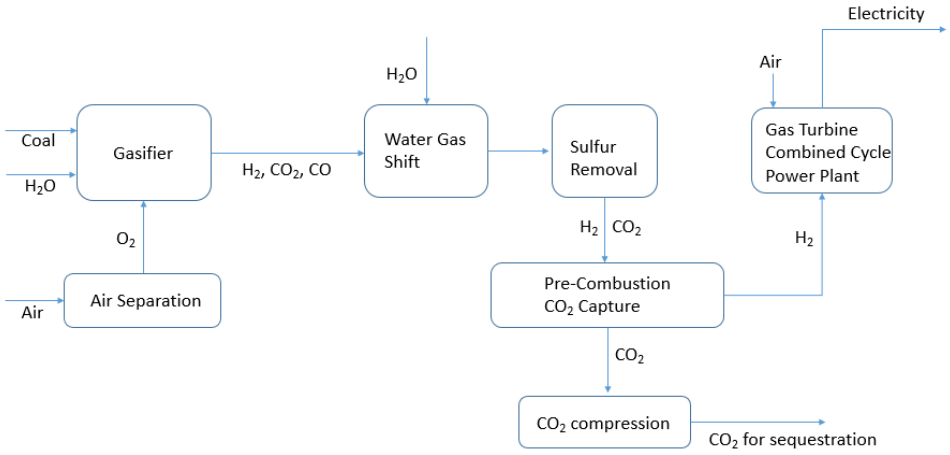

Figure 1.2: Schematic of IGCC including Pre-combustion CO_2 capture

Instead of the direct combustion of coal with air, the coal is gasified with O_2 to create a synthesis gas mixture (syngas) of H_2, CO, and CO_2. A water-gas shift reaction is conducted to convert the CO to CO_2 and then the pre-combustion CO_2 capture process is carried out to separate the H_2 which is combusted to produce steam to drive a turbine to produce electricity from the CO_2 which is sequestered. The IGCC plant has a higher plant efficiency than the traditional PC power plant (43.5% vs. 38-39%).[27,28] The critical separation is of a high pressure (up to 50 bar) 38-45 mol% CO_2 and 50-55 mol% H_2 gas stream.[29,30] Due to the high partial pressure of CO_2 a chemical reaction such as is involved in the PCC amine scrubbing process is not needed and the energetically costly thermal regeneration can be replaced with regeneration via a pressure swing. Physical solvents with a high CO_2 physical solubility and low H_2 physical solubility are typically used to separate CO_2 selectively from the syngas stream.

The current state of the art solvent to do this is a proprietary blend known as Selexol® which is rich in polyethylene glycol dimethyl ether (PEGDME) of a variety of molecular weights. Selexol®'s main advantages are a high CO_2 solubility and selectivity over H_2 as well as a low volatility.

Its main deficiency is its hydrophilic nature as well as decreased CO_2 solubility at high temperatures. Both of these factors explain why the typical Selexol® pre-combustion CO_2 capture process conducts absorption at low (40 °C and below) temperature. This is not desirable and causes a thermal energy penalty as the syngas stream leaving the water gas-shift reactor has to be cooled from high temperatures (200 °C and above) to the temperature of the Selexol® absorber (40°C). Some, but not all, of this energetic inefficiency can be mitigated by process heat integration, but it is desirable to avoid the added process complexity if possible. Consequently a major focus of pre-combustion CO_2 capture solvent research is aimed at identifying hydrophobic physical solvents with improved high temperature CO_2 solubility and selectivity. A variety of physical solvents have been proposed for pre-combustion CO_2 capture. These include room temperature ionic liquids (RTILs), and CO_2-philic oligomers such as polydimethylsiloxane (PDMS) and polypropyleneglycol dimethylether (PPGDME).[31–33]

1.4 Thesis Aims

As described above, considerable scientific and engineering efforts are being directed towards the design and discovery of PCC and pre-combustion CO_2 capture materials. The design space of potential available materials for each covers a wide range. In order, to assess the effect of substituting a novel CO_2 capture material for the current state-of-the-art (i.e. MEA, Selexol®) several variables have to be experimentally measured. The optimal PCC solvent would possess a high CO_2/N_2 selectivity, a high CO_2 working capacity (i.e. a high absorption capacity and an equivalently high desorption capacity), react with CO_2 with rapid kinetics and a low heat of reaction, exhibit excellent resistance to thermal and oxidative degradation, and

possess resistance towards flue gas pollutants such as SO_2 to name a few. It would also exhibit other physical properties such as a low volatility, low corrosivity, low toxicity, and a low viscosity among others. Many of these properties apply to the optimal PCC solid sorbent as well. The optimal pre-combustion solvent would also possess a host of properties including a high CO_2/H_2 selectivity, hydrophobicity, a high CO_2 diffusivity, and a high CO_2 physical solubility, particularly at high temperature. It would also have a low volatility, low corrosivity, low toxicity, and a low viscosity. There is considerable interest in classes of materials with a high degree of structure-specific tunability (e.g. ionic liquids, amino acids, piperazine derivatives). Within this context, the experimental measurement of variables such as the CO_2 absorption rate and capacity or CO_2 physical solubility with traditional experimental methods (e.g. CSTR, wetted wall column) becomes a significant bottle-neck in the screening of newly-synthesized novel solvents. In recent years, the advent of the field of microfluidics has enabled considerable progress in reducing the volume-requirements of CO_2 capture characterization as well as expedited the high throughput screening of novel CO_2 capture materials. This trend in research is illustrated in Figure 1.3.

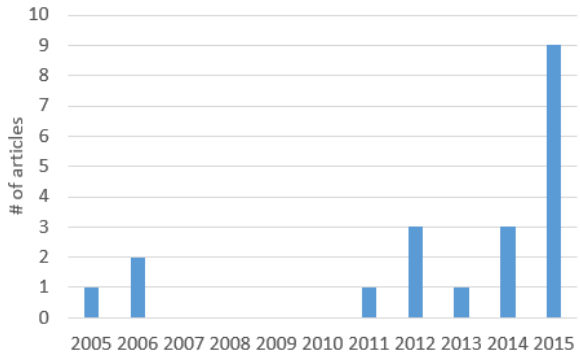

Figure 1.3: Web of science search results for "microfluidic" and "CO_2 capture"

The main focus of this thesis is addressing the experimental measurement of thermodynamic and kinetic CO_2 capture variables with microliter-scale volumes of solvent. A variety of both PCC and pre-combustion CO_2 capture systems are investigated. This thesis focuses on primarily amine-based PCC systems with the goal of identifying important chemical considerations for their capture performance, although the microfluidic techniques illustrated are general to other PCC solvents. The investigation of pre-combustion CO_2 capture systems in this thesis relies heavily on Raman spectroscopy and quantitative analysis methods for obtaining the solvent's CO_2 capture characteristics are illustrated. This thesis is organized as follows. Chapter 2 addresses long-term oxidative and thermal stability considerations for amine-based PCC systems. The effects of flue gas O_2 and SO_2 on the cyclic CO_2 capture capacity of a primary amine-functionalized polymeric solid sorbent are investigated using a packed bed reactor. Chapter 3 investigates the performance of a hydrophobic polymeric pre-combustion CO_2 capture solvent. Raman spectroscopy is used to measure the CO_2 solubility, heat of CO_2 solution, and CO_2/H_2 selectivity of the solvent at room temperature up to 100 °C using less than 5 μL of solvent. Chapter 4 addresses the use of a microfluidic reactor to characterize the chemical absorption of CO_2 by a PCC solvent. The CO_2 absorption capacity and rate of four aqueous amino acid salt solutions and a MEA solution are measured through image analysis of segmented gas-liquid flow. The microfluidic measurements are compared with CSTR measurements and the effectiveness of the microfluidic technique as a screening tool is discussed. Chapter 5 explores the use of Raman spectroscopy to measure the diffusivity of CO_2 in a pre-combustion CO_2 capture solvent. Diffusivity measurements are conducted for water and three polydimethylsiloxane (PDMS) derivatives of varying molecular weight.

Chapter 6 illustrates a Raman spectroscopic technique for measuring the heat of absorption of CO_2 in a PCC chemical solvent. The heat of CO_2 absorption is measured for MEA and methyldiethanolamine (MDEA). Lastly, Chapter 7 summarizes the main conclusions of the preceding chapters and discusses their implications for the general use of microfluidics for CO_2 capture research. Suggestions for building upon the current work are provided as well.

2 Effects of O_2 and SO_2 on the Capture Capacity of a Primary-Amine Based Polymeric CO_2 Sorbent

2.1 Introduction

As described in Chapter 1, post-combustion CO_2 capture from coal requires selective separation of CO_2 from a gas stream at 40-60 °C and nominal gas composition of 12 vol% CO_2, 6% H_2O, 4% O_2, 400 ppm SO_2, and balance N_2 as well as other contaminants such as CO and NO_x.[6] The most mature technology for post-combustion CO_2 capture is absorption via a liquid amine, such as monoethanolamine (MEA) using an absorber and stripper to capture CO_2 cyclically[7] as described in Chapter 1. In practice, MEA is used as part of an aqueous solution, typically 30 wt% MEA.[7] There are however, several drawbacks to the use of MEA. Due to MEA's high reaction energy and high CO_2 binding strength as well as the high heat capacity of water, there is a considerable parasitic energy cost incurred to regenerate the solution in the gas stripper. Additionally there are concerns over MEA losses due to volatility and through oxidation.[13] Furthermore, it has been shown that flue

gas contaminants such as SO_2 can bind with MEA and reduce its CO_2 capture capacity.[14] It has been found that SO_2 and O_2 accelerate the rate of MEA degradation, to an increasing extent as the concentration of SO_2 increases.[14]

A promising alternative to liquid amine systems that addresses some of the challenges discussed above is CO_2 capture with a solid sorbent. Most evident is the elimination of the parasitic energy cost of heating and transporting large volumes of water. A wide variety of solid sorbents can be used for CO_2 capture including physical sorbents, which adsorb primarily through van der Waals interactions, such as zeolites[34] or activated carbon[35] based sorbents as well as a wide range of chemisorbents, which involve chemical reaction between the surface sites and adsorbates. Foremost are the amine-functionalized chemisorbents which can be divided into three main types.[36] The first type is that of a porous support impregnated physically with an amine species.[6] The second type is that of a polymeric support with covalently bonded side chains containing amine functionality.[25] Lastly, the third type is that of a porous support which contains amine-containing polymers polymerized in situ.[25] These solid sorbent systems present a number of potential advantages over the traditional MEA process. They typically have lower heat capacities than aqueous amine solutions which reduces the energy cost due to support heating during the regeneration. The gas phase diffusion of CO_2 through the porous sorbent provides fast mass transfer of CO_2 to the amine sites. In certain cases, the amine being covalently bonded to the solid support reduces amine losses through volatility when compared with aqueous amine solutions. However, the amine functionality means that these solid sorbent systems are susceptible to the same thermal and chemical stability issues as their liquid amine counterparts. Considering the minimum 1000 cycles needed for an effective

sorbent lifetime,[37] it is vital that the active amine loading of the sorbent be stable over many cycles of exposure to high temperature oxidant-rich environments as occurs in the gas stripper. In this chapter we specifically address the long-term thermal and chemical stability of a solid polymeric amine sorbent, the ion-exchange resin Lewatit VP OC 1065 (Lanxess). It is a divinylbenzene polystyrene copolymer with primary amine functionality and 8-10% cross-linking for stability.

Previous research within our group has shown this material to exhibit several favorable characteristics of a CO_2 capture sorbent.[38] It has shown capture capacities from a 10 vol% CO_2 in N_2 stream in the range of 1.85 to 1.15 mol/kg depending on the adsorption temperature ranging from 30 to 70 °C.[38] OC 1065 captures CO_2 through two mechanisms, one tied to a pressure swing desorption and the other to a temperature swing desorption. In the previous study these two contributions were decoupled and it was shown that the temperature swing component is tied to a chemical reaction between CO_2 and the amine functional group on the resin to form carbamic acid and/or carbamate ion. It was also postulated that the pressure swing component is a result of the solubility of CO_2 in the resin.

Thermogravimetric analysis has shown the resin to have relatively low moisture adsorption compared to other sorbents.[38] Low moisture adsorption is important because the sorbent will be required to selectively remove CO_2 from a flue gas stream that is saturated with moisture.[39] Thermogravimetric analysis of the resin exposed to a wet N_2 stream with 9.1 vol% H_2O for 40 min at 50 °C resulted in a moisture uptake of 2.7 wt% or 1.5 mol H_2O/kg resin, which is significantly lower than other values reported in the literature.[40] For example, silica supported sorbents exposed to a lower H_2O concentration of 0.8 vol% for 1 h at 28 °C is reported to have a moisture

uptake of 9.5 wt%.[41] Previous work on supported amidine on activated carbon showed greater than 40 wt% moisture adsorption.[40] The resin also has shown to be completely regenerated under an inert N_2 gas stream at 120 °C and under a 100% CO_2 gas stream at 200 °C.[38] In a packed bed reactor, the resin was exposed to a 10 vol% CO_2 stream as the temperature of the reactor was changed back and forth from 50 and 120 °C for 18 cycles. The working capacity remained stable over this time scale.

The key issues that were not addressed fully in the previous work are the chemical and thermal stability of OC 1065. In particular the effect of O_2 and SO_2 on the CO_2 capture capacity is of crucial importance for the successful implementation of the sorbent due to the presence of these contaminants in the post-combustion flue gas. SO_2 is of great concern for amine-based sorbents as much work has shown it to react strongly with amines and inhibit CO_2 adsorption in amine-based sorbents as well as to form heat stable salts with amine solvents.[14,42,43] O_2 is also a major concern because amine oxidation has been shown to have a negative impact on CO_2 capture capacity making it a significant factor in determining the useful lifetime of the amine for CO_2 capture from oxidative environments such as post-combustion flue gas .

The aim of this chapter is to address the issue of long-term chemical and thermal stability by investigating the tolerance of the OC 1065 resin to O_2 and SO_2. In particular, this work focuses on identifying the effects of these constituents on the working capacity of OC 1065 and seeks to characterize any degradation that is observed. Whether the resin is poisoned by these constituents reversibly or irreversibly as well as the means necessary to restore its activity are important information to determine the feasibility of the sorbent for large-scale CO_2 capture from flue gas. The remainder of this chapter is organized as follows: we first present elemental analysis on OC

1065 and comment on the total nitrogen-loading and available amine adsorption sites of the resin. We then show the effect of 4% O_2 in simulated flue gas on the capture capacity of the resin. We then show that the CO_2 capture capacity of the resin decreases as a result of exposure to 431 ppm SO_2 in simulated flue gas. We then investigate the nature of the observed SO_2-poisoning as well as means for regenerating the SO_2-poisoned resin. Finally we comment further on the long-term thermal stability of the resin. A majority of this work has been published in Hallenbeck and Kitchin.[44]

2.2 Methods

The CO_2 capture capacity of OC 1065 was measured under a variety of controlled conditions in a custom-built packed bed reactor apparatus.[38,45] The apparatus is equipped to control and measure key variables such as reactor temperature, flow rate, CO_2 concentration, and pressure drop via a LabVIEW acquisition module. The CO_2 concentration in the reactor effluent is measured simultaneously using both a (Valtronics 2015SP3) OEM CO_2 analyzer and a high-resolution mass spectrometer (Hiden HPR-20). Quantitative measurement of the CO_2 concentration from the mass spectrometer intensity is done through a calibration procedure done prior to every experiment with three gases of known concentrations, typically 0%, 100% CO_2, as well as the test gas, typically either 10 or 12 vol% CO_2 (see Appendix 8).

During a typical packed bed reactor experiment, a sample of resin (3-4 g) is first dried in the oven at 120 °C to constant mass (typically 2-3h) to eliminate excess water it contains in its shipped state. A sample of the dried resin of known mass is loaded into the tubular reactor (0.375 in. i.d.) suspended between two pieces of glass wool making a column approximately 5 in. high.

The resin has a bulk density of 630-710 g/L with a column porosity between 0.42 and 0.48 according to the manufacturer's specifications. A purge step is then conducted by passing N_2 at a nominal flow rate of 200 cc/min through the reactor at elevated temperature (up to 120 °C) as the resin captures up to 1 mol CO_2 per kg from exposure to ambient air. The typical pressure drop through the bed is about 0.2 psi. Following the purge step, the reactor is switched offline and the mass spectrometer calibration is conducted. Following calibration, adsorption is carried out at a fixed temperature (50 °C in this work). The simulated flue gas is passed through the reactor until breakthrough is observed and the effluent gas composition has returned to the influent concentration, indicating that the resin has been saturated with CO_2. The reactor is switched offline to prepare for the desorption step. The amount of CO_2 adsorbed is calculated from the average volumetric flow of CO_2 in the effluent stream over the period following breakthrough when the concentration of CO_2 has stabilized to determine a baseline value. The volumetric flow of CO_2 is then subtracted from the baseline value and integrated over the adsorption time to give the volume of CO_2 adsorbed by the resin using equation 2.1

$$V_{CO_2} = \int (Qb_{CO_2} - Q(t)C_{CO_2}(t))dt \tag{2.1}$$

where Qb_{CO_2} (mL/min) is the baseline value of the volumetric CO_2 flow, Q(t) is the measured total volumetric gas flow (mL/min), and $C_{CO_2}(t)$ is the measured CO_2 concentration (vol%) in the effluent stream. This calculated volume of adsorbed CO_2 is converted to a molar quantity using the ideal gas law at the temperature and pressure (25 °C, 1.01325 bar) of the effluent gas stream and normalized by dividing by the mass of the resin to calculate the adsorption capacity in units of mol/kg. Desorption is carried out via both a pressure swing

and temperature swing by first passing inert N_2 through the reactor at the constant adsorption temperature for 20 min then increasing the temperature at a rate of 3 °C/min until CO_2 stops desorbing as can be seen in Figure 2.1.

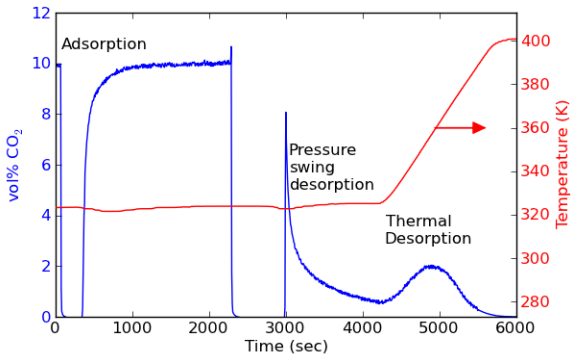

Figure 2.1: Typical adsorption and desorption data used for capacity calculation.

The dead volume, or void space due to the volume of gas trapped within the reactor upon valve changes, correction was taken into account in the capacity calculations. This correction was empirically derived from experiments with an inert support with an equivalent bulk density to OC 1065.[45] The void space was found to contribute 0.12 mol of CO_2 to the apparent capacity. All values reported in this chapter have taken this into account where appropriate.

Equation 2.2 is used to calculate the volume of CO_2 desorbed.

$$V_{CO_2} = \int Q(t) C_{CO_2}(t) dt \tag{2.2}$$

The calculated volume of CO_2 is converted to a molar quantity with the ideal gas law and normalized by the mass of the resin to calculate the desorption capacity in units of mol/kg.

The packed bed reactor apparatus can also be used to measure the CO_2 capture capacity over multiple consecutive cycles of adsorption and desorption from a continuous gas stream by simply cycling the reactor

temperature without changing the feed stream to the reactor. The capture capacity (both adsorption and desorption) is then calculated by integrating the flow rate and CO_2 concentration data about the baseline CO_2 flow present in the inlet gas stream.

Elemental analysis was used to identify any changes in chemical composition of the resin as a result of exposure to O_2 and SO_2. The mass-based analysis was carried out by Micro Analysis Inc. and done using combustion for C, H, N, and S and using pyrolysis for O. Surface area and pore size measurements were conducted following packed bed stability tests from N_2 adsorption isotherm experiments using a Nova 2100 (Quantachrome). Samples were degassed at 125 °C for 2.5 h prior to measurement. The surface area was determined through the BET method, and the pore volume and pore size was determined through the BJH method.[46,47]

2.3 Results and Discussion

2.3.1 Estimating Available Amine Sites

In previous research, the maximum theoretical amine loading of OC 1065 was deduced from energy-dispersive X-ray spectroscopy measurements to be 6.7 mol N/kg.[38] However, elemental analysis provides another complementary estimate of the amine loading of the resin. In this work, the value of 7.9% N averaged over four measurements (Table 2.1) represents an amine loading of 5.9 +- 0.1 mol N/kg.

Table 2.1: Mass-Based Elemental Analysis of OC 1065 As Received and Dried (Precision: +-0.30%)

Sample	%C	%H	%N	%O	%S
1	81.79	8.25	8.00	3.48	0.00
2	82.09	8.36	7.97	4.13	0.00
3	81.11	8.26	7.94	4.19	0.00
4	81.28	7.85	7.77	3.15	0.00

However, since only a fraction of the total amine sites are accessible to reaction with CO_2, the more critical value is the number of accessible amine sites. This value can be estimated from the sulfate loading on the resin following saturation with sulfuric acid, which based on the average of three measurements (Table 2.2) was 2.7 mol H_2SO_4/kg.

Table 2.2: Mass-Based Elemental Analysis of OC 1065 Following Saturation with 1.5 M H_2SO_4 Aqueous Solution (Precision: +-0.30%)

Sample	%C	%H	%N	%O	%S
1	64.31	7.12	6.03	15.22	6.59
2	63.66	7.08	6.08	16.60	7.00
3	63.15	6.87	6.13	15.16	6.47

Assuming a 1:1 molar stoichiometry, the amine loading available to reaction is 2.7 mol/kg. This suggests that the measured CO_2 capture capacity of the resin at 50 °C from a pure CO_2 stream, 2.5 mol/kg, is approaching the capacity limit of this sorbent.

2.3.2 Effect of O_2 in Flue Gas on OC 1065

The tolerance of OC 1065 to O_2 was studied by conducting 17 continuous cycles of adsorption and desorption with a test gas of 12 vol% CO_2, 4% O_2, 84% N_2. This gas was passed continuously through the loaded reactor during the entire course of the experiment, and adsorption and desorption occured via a thermal swing between 50 and 127 °C. Each cycle lasted 2 h and 12 min. All

capacity calculations are calculated using the baseline concentration of 12% CO_2 for the entire experiment. The resulting calculated capture capacities can be seen in Figure 2.2.

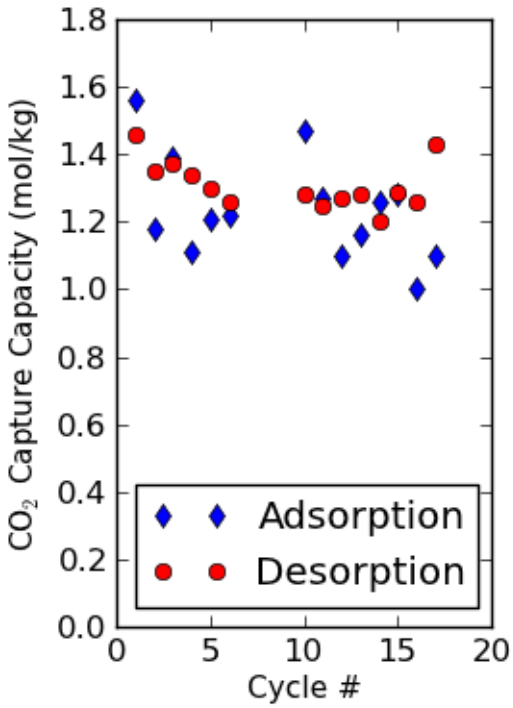

Figure 2.2: CO_2 capture capacity of resin over 17 temperature swing regeneration cycles in the presence of O_2

The average capacity was 1.27 mol/kg. Past work indicated a reproducibility of 0.1 mol/kg,[45] thus we believe that the variations in capacity here are due to precision and not due to any degradation of the resin under these conditions.

2.3.3 Effect of SO_2 on OC 1065 CO_2 Capture Capacity

A similar experiment was conducted to determine the effect of SO_2 at concentrations typical of coal flue gas, on the CO_2 capture capacity of OC 1065. A test gas of 12.5 vol% CO_2, 4% O_2, 431 ppm SO_2, balance N_2 was

passed continuously through the reactor with a thermal swing between 50 and 127 °C conducted as done with the O_2 stability test. This experiment was repeated twice, and the CO_2 capture capacity throughout all three experiments can be seen in Figure 2.3.

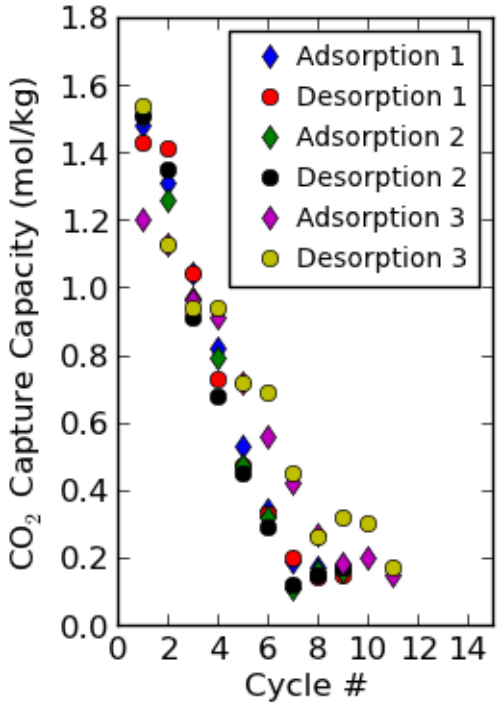

Figure 2.3: CO_2 capture capacity of resin in presence of SO_2. Experiments 1 and 2 tested a 3 g sample of resin, while experiment 3 tested a 4 g sample of resin

The CO_2 capture capacity of OC 1065 decreased in each cycle of exposure to SO_2 until the capacity was practically gone. The loss of activity occurred rapidly and in a near linear fashion throughout the first seven cycles before stabilizing at a minimal capacity of approximately 0.2 mol/kg. The mass spectrometer intensity of SO_2 and the concentration of CO_2 in the effluent gas stream was tracked with the analyzer and mass spectrometer throughout experiment 1 and can be seen in Figure 2.4.

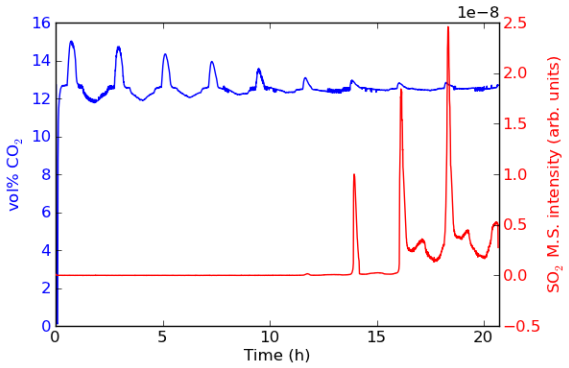

Figure 2.4: CO_2 and SO_2 variation throughout experiment 1

It can be seen that during the course of the first six temperature swing regeneration cycles, practically no SO_2 is detected by the mass spectrometer, suggesting that all of the SO_2 is captured by the resin until the resin becomes saturated around the sixth cycle where the first tiny peak is shown for SO_2 in the mass spectrometer signal. After that there are peaks in the SO_2 spectrum that indicate thermally reversible SO_2 species on the resin. During the period prior to the first small peak in the SO_2 intensity, observed at approximately 11.8 h, the amount of SO_2 adsorbed on the resin can be approximated from the SO_2 flow rate into the reactor as 0.82 mol/kg. This value is less than the reduction of CO_2 capture capacity during the same six temperature swing regeneration cycles.

This reduction in CO_2 capture capacity could be a result of both physical and chemical effects. To determine whether exposure to SO_2 caused a reduction in either the surface area or pore size of the resin which in turn would decrease the CO_2 capture capacity of the resin, a series of nitrogen adsorption isotherm measurements were carried out on the resin both before and after the SO_2 packed bed experiment. The results of these measurements can be seen in Table 2.3.

Table 2.3: Surface Area and Pore Size Analysis of SO_2-Poisoned Resin

	Untreated Resin	SO_2-poisoned resin
BET surface area (m^2/g)	34	40
BJH pore volume (cc/g)	0.23	0.23
BJH pore radius (nm)	15.4	15.3

A small increase in surface area was observed for the SO_2-poisoned resin, but we do not believe that this is significant (for small surface areas such as these, the surface area is reproducible to approximately 5 m^2/g). The results do not show any significant differences in the surface area, pore volume or pore radius of the as received and SO_2-poisoned resin. Thus, a reduction in surface area or pore volume is not responsible for the reduction in CO_2 capture capacity and so the reduction in CO_2 capture capacity is predominantly a result of an interaction between SO_2 and the primary amine functional groups in OC 1065.

The adsorption of SO_2 onto the resin was confirmed by the results of mass-based elemental analysis done on the resin following the experiments with O_2 and SO_2, which can be seen in Table 2.4.

Table 2.4: Elemental Composition of Resin Following SO_2 Poisoning (mass percent reported with precision of +-0.3%)

Sample	%C	%H	%N	%O	%S
Following SO_2 experiment no. 1	76.0	6.9	6.8	6.0	2.9

The increase in the % S after the SO_2 experiment corresponds to a loading of 0.98 mol/kg. This value is higher than the loading of 0.82 estimated from the flow rate prior to the first tiny peak in SO_2 intensity, indicating that additional SO_2 adsorbed onto the resin during the seventh, eighth, and ninth temperature regeneration cycles. The reduction in CO_2 capture capacity during the same experiment was 1.31 mol/kg. The exact mechanism of degradation aside, it is clear that SO_2 at the concentrations typical of flue gas from coal is a

contaminant of great concern if OC 1065 is to be used for post-combustion CO_2 capture applications. Furthermore, it is likely that all sorbents with primary amines will be similarly poisoned by SO_2 as well.

2.3.4 Regeneration of SO_2-Poisoned OC 1065

It is of interest to determine whether it is possible to reclaim the activity of the poisoned resin through either thermal or chemical means. This is an advantage for solvents, which can be reclaimed by treatment with activated carbons and ion-exchange resins to remove heat-stable salts.[48] We first examined the feasibility of poisoned sorbent regeneration via a thermal swing by exposing a sample of poisoned resin to a N_2 environment in the packed bed reactor at temperatures up to 208 °C. We hypothesized that being a stronger acid gas, it could take a higher temperature to desorb SO_2 than CO_2. No significant increase in the mass spectrometer intensity of SO_2 was observed during this experiment (see Appendix 8). Following this treatment, the sample of resin was tested at an adsorption temperature of 50 °C with a 10 vol% CO_2, N_2 stream and did not exhibit a measurable CO_2 capacity. This shows that the adsorbed SO_2 species is stable up to 208 °C.

We next consider chemical regeneration. Since SO_2 is an acid gas and may interact with the resin through acid-base chemistry, we hypothesize that treatment of the poisoned resin with a strong base, such as aqueous NaOH, could regenerate the resin in the same way that ion exchange resins are normally regenerated. To simultaneously show that the reaction of an acid with the resin poisons the resin, and to determine whether this reaction of the resin with a strong acid can be reversed using NaOH, a sample of resin was treated with 1.5 M sulfuric acid at room temperature for 1 day, washed in distilled water for 1 day to remove excess acid, and then tested in the

packed bed reactor. The result was a complete loss of CO_2 capacity due to protonation of the amines by the acid with sulfate ions providing charge neutrality. The same sample of resin was then treated with 1.5 M NaOH at room temperature for 3 days to deprotonate the amines and remove the sulfate ions, washed in distilled water for 1 day to remove excess base, and tested in the packed bed reactor at 50 °C and 10 vol% CO_2, which determined the CO_2 capture capacity to be 1.5 mol/kg. This demonstrated that the resin could be completely poisoned by an acid (H_2SO_4) and completely regenerated by a chemical method.

This same chemical treatment with NaOH was used on the SO_2-poisoned resin from experiment no. 1. However, we only observed the reclamation of approximately 1/3 (0.49 mol/kg) of the CO_2 capture capacity at the capture conditions of 50 °C and 10 vol% CO_2. Elemental analysis (Table 2.5) of all these samples showed that the resin poisoned by sulfuric acid indeed took up a lot (6.5%) of sulfur but that the chemical regeneration was able to completely remove all the sulfur. The SO_2-poisoned resin also showed significant (2.9%) uptake of sulfur. The chemical treatment, however, was only able to remove 43% of the adsorbed sulfur which is in reasonable agreement with the 35% recovery of CO_2 capture capacity.

Table 2.5: Mass-Based Elemental Analysis of OC 1065 Following Treatment with Sulfuric Acid, As Well As Following Regeneration with NaOH (Precision: +-0.30%)

Sample	%C	%H	%N	%O	%S
SO_2-poisoned resin partially regenerated with NaOH	76.6	6.8	6.4	4.6	1.7
Treated with Sulfuric Acid	63.2	6.9	6.1	15.2	6.5
Fully Regnerated with NaOH	80.9	7.8	7.8	3.1	0.0

The increase in %O and %S from treatment with sulfuric acid solution is stoichiometrically consistent with addition of SO_4-containing species. The

CO_2 capture capacity at 50 °C and 10 vol% CO_2 of the resin before and after poisoning and regeneration can be seen in Table 2.6.

Table 2.6: CO_2 Capture Capacity Before and After Poisoning and Regeneration

	CO_2 capture capacity (mol/kg)
untreated	1.39
sulfuric acid poisoned	0.08
regenerated with NaOH	1.51
SO_2-poisoned	0.1
partially regenerated with NaOH	0.48

In all of the work presented here, the gas stream was dry due to limitations of the experimental apparatus employed. SO_2 is known to react with sodium hydroxide solutions to make sodium bisulfite ($NaHSO_3$). We conjecture that the primary amine can react with SO_2 in a similar way that is not very reversible, but were unable to obtain spectroscopic (Raman or IR) evidence of that reaction. It is possible that the presence of water could promote the formation of the bisulfite ions, which could make SO_2 sorption more reversible. Further investigation of this is outside the current scope of work and would require a different approach to humidifying the gas stream than our apparatus uses.

2.3.5 Thermal Stability of OC 1065 in Air

In the packed bed reactor experiments described above, we have investigated the stability of OC 1065 over time scales much shorter than the estimated 1000 cycles needed for a solid sorbent to be economically viable.[35,49] Long-term thermal stability in an oxidative environment is just as critical to the success of a sorbent as the chemical stability investigated above. In previous work, it was shown that OC 1065 loses its activity from exposure to the combination of high temperature (120 °C) and vacuum for a

long time such that the resin becomes completely dehydrated and a significant reduction in surface area and pore size occurs.[38] On the other hand, the packed bed reactor experiments have shown the resin to be quite stable under conditions more typical of post-combustion CO_2 capture where the resin is exposed to high temperature (120 °C) but only during temperature swing desorption where the amine is mostly reacted with CO_2. However, it is known that primary amines can become reactive at high temperatures and can either be oxidized or react with CO_2 to form stable urea groups after which the sorbent ceases to be effective.[50,51]

To assess the stability of OC 1065 in a hot oxygen-rich environment over longer time scales, a sample of resin was kept at 120 °C in air for 7 days. The CO_2 capture capacity of the sample was then measured in the packed bed reactor at 50 °C from a 10 vol% CO_2, N_2 stream and determined to be 0.28 mol/kg, which is a 79% reduction in capacity from the untreated resin. This reduction is evident in the desorption profile of the resin before and after this treatment shown in Figure 2.5.

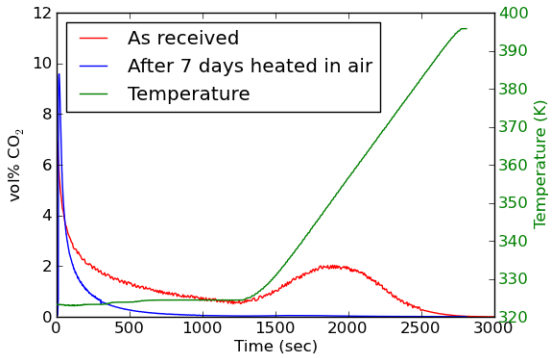

Figure 2.5: Pressure and temperature swing desorption profiles for resin before and after 7 days at 120 °C.

It can be seen that a substantial decrease in both the temperature swing and pressure swing components occurred and that the temperature swing

contribution to the desorption capacity was completely eliminated. However, this reduction in CO_2 capture capacity is not a result of a decrease in surface area and pore size as described in our past work for high temperature exposure under vacuum. We confirmed this with a series of N_2 adsorption isotherm measurements (Table 2.7).

Table 2.7: Surface Area and Pore Size Analysis of Resin Following 7 Days of Exposure to 120 °C in Air

	untreated	after 7 days
BET surface area (m^2/g)	34	42
BJH pore volume (cc/g)	0.23	0.28
BJH pore radius (nm)	15.4	15.3

Elemental analysis revealed a significant reduction in the nitrogen content of the resin (Table 2.8).

Table 2.8: Elemental Analysis of Resin after 7 Days Exposure to 120 °C in Air

sample	%C	%H	%N	%O	%S
following 7 day heating treatment	81.8	7.4	6.4	4.0	0.0

The decrease in nitrogen content corresponds to a 1.1 mol amine/kg decrease in the amine loading, which is in good agreement with the 1.11 mol CO_2/kg decrease in CO_2 capture capacity. Additionally the hydrogen content decreased by an amount corresponding to 7.6 mol H/kg, while the carbon and oxygen content of the resin remains unchanged within the 0.3% precision of the measurements. Clearly prolonged (days or more) continuous exposure to air at high temperatures (120 °C) leads to irreversible amine loss for OC 1065.

2.4 Conclusions

The tolerance of a primary amine-functionalized ion-exchange resin (OC 1065) to O_2 and SO_2 was evaluated in this work. The CO_2 capture capacity

remained stable over 17 capture cycles under continuous exposure to a 12% CO_2, 4% O_2, 84 % N_2 gas stream indicating that irreversible oxidation did not significantly occur over this time scale. The resin was, however, poisoned quickly by continuous exposure to a 12.5% CO_2, 4% O_2, 431 ppm SO_2, 84% N_2 gas stream resulting in an adsorption of 0.98 mol/kg of SO_2 and a decrease in CO_2 capture capacity of 1.31 mol/kg after only 9 temperature swing regeneration cycles. The poisoned resin was not thermally regenerable. Treating the poisoned resin with NaOH resulted in a 43% SO_2 removal and 35% reclamation of CO_2 capture capacity under 10 vol% CO_2 and 50 °C capture conditions. The difficulty in fully regenerating the poisoned resin is most likely due to an irreversible reaction between SO_2 and the amine due to the stronger acidity of SO_2 in comparison to CO_2. That the poisoned resin is partially regenerable could indicate that SO_2 is adsorbing on the resin through more than one mechanism, one of which is reversible. Additionally, evidence was found for amine oxidation during extended exposure to a hot (120 °C) oxygen-rich environment.

This chapter highlights, in particular the negative impact of SO_2 on the CO_2 capture capacity of primary amines, which strongly suggests SO_2 should be removed from the flue gas or converted to SO_4-containing species such as sulfuric acid prior to an amine-based post-combustion CO_2 capture process. Ultimately, chemical and thermal stability will be an issue with any sorbent, and the necessary degree of chemical or thermal stability is determined by the economically viable sorbent lifetime. Susceptibility to irreversible SO_2 adsorption/absorption will always require rigorous desulfurization of the flue gas prior to post-combustion CO_2 capture with primary amines which are currently the most promising capture technology. However, SO_2-induced degradation of the capture material may be less of a concern in

pre-combustion CO_2 schemes where the solvents are much less chemically reactive and the physical absorption of SO_2 is not likely to be as competitive with CO_2 as is the case for chemical absorption where CO_2 capture is dependent on the availability of amine groups. Characterization of physical solvents in pre-combustion applications is the subject of the next chapter.

3 Quantitative Measurement of CO_2 and H_2 Solubility and Selectivity in a PDMS-PEGDME Hybrid Physical Solvent Using Raman Spectroscopy

3.1 Introduction

As described in Chapter 1 pre-combustion CO_2 capture within the context of an integrated gasification combined cycle (IGCC) power plant is an alternative approach to achieving 90% CO_2 capture than post-combustion CO_2 capture. In this context CO_2 must be separated from a high pressure (up to 50 bar) syngas stream containing predominantly CO_2 (approximately 40%) and H_2 (approximately 55%).[29,30] In comparison with post-combustion CO_2 capture, the significantly higher partial pressure of CO_2 means that substantial CO_2 absorption can be achieved solely through physical solubility, and consequently the higher regeneration energy penalty associated with a chemical reaction can be avoided. The most technologically mature physical CO_2 solvent is known as Selexol®, which is a proprietary blend that is rich in polyethylene glycol dimethyl ether (PEGDME).[52] The structure of PEGDME can be seen in Figure 3.1.

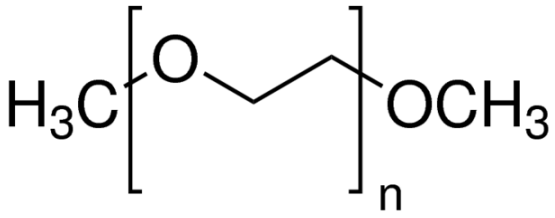

Figure 3.1: Molecular structure of PEGDME

Absorption with Selexol® is typically carried out at 40 °C due to the fact that Selexol®'s CO_2 solubility decreases with increasing temperature as well as to avoid parasitic water absorption due to Selexol®'s hydrophilic nature. Consequently the syngas must be cooled substantially in order to condense and remove any water before entering the absorber which introduces a significant energetic penalty. The CO_2 clean gas also needs to be reheated to approximately 200 °C for combustion. These additional cooling and heating steps decrease the overall efficiency of the IGCC, adds additional utility costs, and complicates process integration. A major focus of research in physical pre-combustion solvents is developing/discovering hydrophobic solvents that can achieve high CO_2 solubility at higher temperatures.

Several classes of hydrophobic physical solvents have been proposed and investigated for pre-combustion CO_2 capture. These include oligomers, such as polydimethylsiloxane (PDMS) and polypropyleneglycol dimethylether (PPGDME), as well as room temperature ionic liquids.[31–33] A significant challenge is overcoming a tradeoff between CO_2 solubility and hydrophobicity as has been demonstrated for the water-immiscible PDMS.[53] The structure of PDMS can be seen in Figure 3.2.

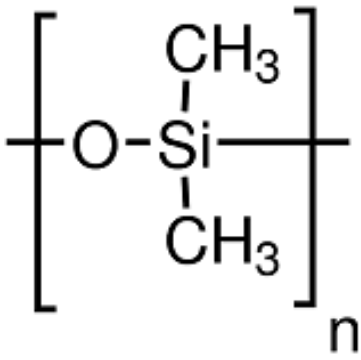

Figure 3.2: Molecular structure of PDMS

The hydrophobic nature of PDMS is counterbalanced by lower CO_2 solubility and selectivity compared with the hydrophilic PEGDME. In order to keep the desired properties of both PDMS and PEGDME, a hybrid solvent has been synthesized and investigated by NETL.[54] The molecular structure of this PDMS-PEGDME hybrid can be seen in Figure 3.3. The molecular weight of the hybrid solvent studied in this chapter is 438 g/mol.

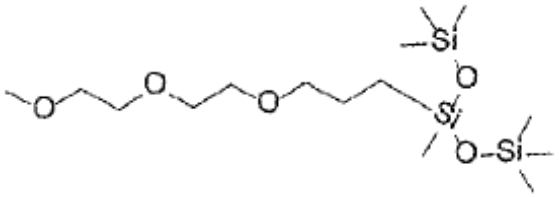

Figure 3.3: Molecular structure of PDMS-PEGDME hybrid

While PEGDME is fully miscible with water and PDMS is immiscible with water up to 120 °C and 10000 psi, the PDMS-PEGDME hybrid can be described as very hydrophobic as it absorbs less than 1 wt% water.[54] This presents an opportunity to improve upon the efficiency of the Selexol® process by designing a higher temperature absorption process with the hydrophobic hybrid solvent. However, it is critical that the CO_2 solubility and selectivity of the hybrid solvent remains competitive with that of

Selexol®. In contrast with PEGDME and PDMS, which are commercially available, the PDMS-PEGDME hybrid solvent must be synthesized[54] in-lab prior to characterization. Consequently the PDMS-PEGDME hybrid solvent represents a good example of a novel solvent for which millifluidic, and to an even further extent microfluidic, characterization methods are highly desirable.

Previous research in the Kitchin group has developed a capillary-based method for the measurement of gas solubilities using Raman spectroscopy that only requires $\approx\mu$L volume of solvent.[55] While the method is general to any gas, prior to the work presented in this chapter, the method was only applied experimentally to CO_2. The aim of this chapter is to use the capillary-based Raman spectroscopic method to determine the CO_2 and H_2 solubilities and CO_2 / H_2 selectivity of the PDMS-PEGDME hybrid solvent. The measured solubilities for CO_2 and H_2 will be compared with those of Selexol® across a range of temperatures (23 to 100 °C).

3.2 Methods

3.2.1 Experimental description

The methodology of measuring the Henry's law constant of CO_2 and a physical solvent using Raman spectroscopy used in the current work was explained and validated in Anita Lee's dissertation.[55] Here we present a brief summary of this methodology and its extension to non-room temperature conditions and the solubility of H_2.

Raman spectroscopy was carried out on a Horiba LabRamHR spectrometer using a Spectra Physics 532 nm Nd:Yag laser with an operating power of 0.2 W as the excitation source. Spectra were taken using an Olympus 50xLWD objective and were recorded as the average of eight one-second exposures.

Samples were contained in a microliter sample volume size apparatus consisting of a fused silica capillary to carry a small microliter sized solvent sample with a head space, and a Swagelok system that can be directly pressurized by a gas cylinder up to 60 bar in this work. The capillary can be heated externally with a CAP500 capillary pressure stage and a T95 system controller manufactured by Linkam. The stage is capable of heating the capillary in the range of -196 to 500 °C. The stage contains a 50 mm silver block as the heating source whose surface temperature is measured to an accuracy of 0.1 °C. The entire stage is placed underneath the microscope objective for the acquisition of Raman spectra.

Solvent samples were prepared by first cutting silica capillary (320 μm ID/430 μm OD Polymicro Inc. LLC) to approximately 11 cm in length. As purchased, the surface of the capillary is coated with a polyimide coating that greatly enhances the durability of the capillary but produces a fluorescence signal that conceals the Raman spectra of the sample inside the capillary. Consequently the polyimide coating on the 2-3 cm portion of the capillary containing the solvent was removed with a butane torch. The capillary is filled with 1-2 cm (about 1-2 μL) of solvent through capillary action, the clear end is fused closed with a small tip acetylene torch, and the fused capillary is then centrifuged to remove the air trapped between the solvent and the fused end resulting in all the solvent being located at the fused clear end with a single gas-liquid interface clearly visible through the uncoated section of the capillary. The polyimide coated open end of the capillary is then epoxied to 1/16 in. stainless steel tubing. Once the epoxy sets, the tubing is connected to the rest of the high pressure Swagelok assembly, and the capillary is threaded through the opening in the CAP500 so that the entire uncoated section of the capillary containing the solvent and an additional 0.5 to 1 cm of head space

is placed in contact with the silver block heater. The CAP500 and pressure assembly are both placed on a motorized microscope stage which enabled the movement of the sample in the x,y,z directions relative to the microscope objective during experiments.

Prior to each Raman experiment the spectrometer was calibrated using a silicon standard. The capillary apparatus was then pressurized and heated to the desired pressure and temperature. The system was then allowed to equilibrate over a period of time, approximately 2 hours, and the z-position focal length was then selected as the position that yielded the highest sample Raman peak intensity from a z-axis Raman spectral scan. Spectra were then collected of the solvent phase, 50 μm away from the gas-liquid interface, and of the gas phase, 500 μm away from the interface. The system pressure was then increased to a new pressure and spectra acquisition was repeated.

3.2.2 Data analysis

A typical Raman spectrum for gaseous CO_2 (figure 3.4) exhibits two main peaks located at 1388 and 1286 cm^{-1}.

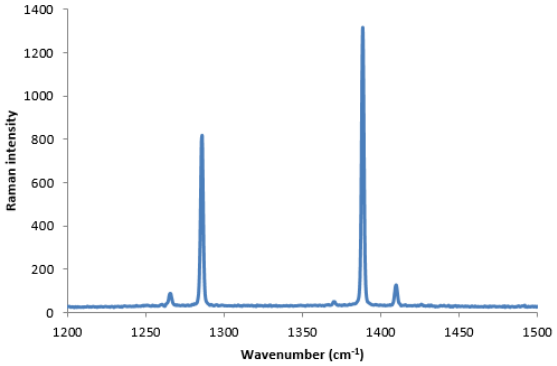

Figure 3.4: Raman spectrum of gaseous CO_2

The peak locations for CO_2 dissolved in Selexol® are shifted to 1381 and 1275 cm^{-1} as can be seen in Figure 3.5.

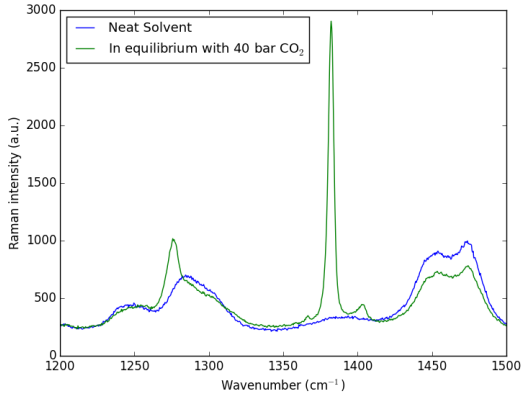

Figure 3.5: Raman spectrum of CO_2 dissolved in Selexol®

The Raman spectrum of H_2 gas can be seen below exhibiting 1 main peak at 4157 cm^{-1}.

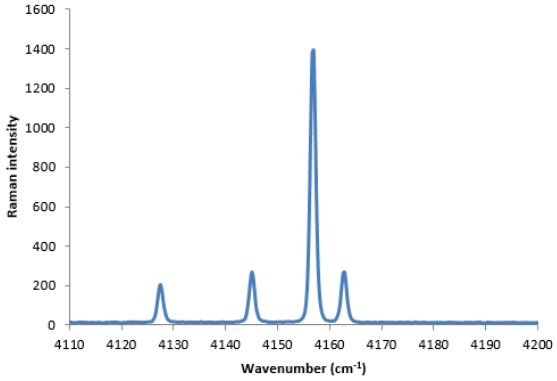

Figure 3.6: Raman spectrum of gaseous H_2

The Raman spectrum of Selexol® in equilibrium with 60 bar of H_2 can be seen below. Only 1 broad peak is evident at 4130 cm^{-1}.

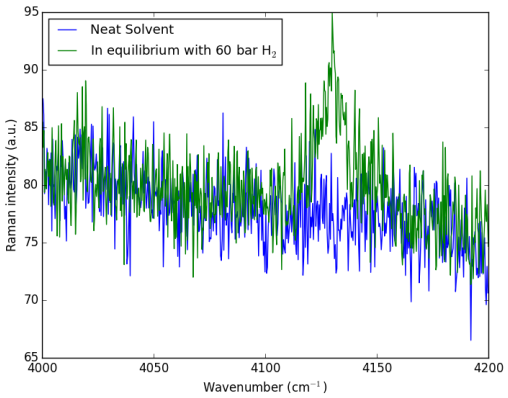

Figure 3.7: Raman spectrum of H_2 dissolved in Selexol®

The concentration of CO_2 in the sample is directly proportional to the area underneath the CO_2 peak located at 1388 cm^{-1} and 1381 cm^{-1} in the gas and solvent phases respectively by equation 3.1 where σ is the Raman cross section of the CO_2 molecule. For the case of H_2 the Raman peak at 4157 cm^{-1} in the gas phase and 4130 cm^{-1} in the solvent phase is used.

$$A = \sigma C \tag{3.1}$$

In order to quantify the CO_2 solubility, a dimensionless Henry's Law constant, equation 3.2 , is calculated from the Raman spectra data.

$$K_H^{cc} = C_{CO_2,g}/C_{CO_2,s} \tag{3.2}$$

This is done by first numerically integrating the area underneath the gas phase and solvent phase CO_2 (or H_2) peaks at multiple pressures and plotting the areas in the gas phase against the areas in the solvent phase as seen in Figure 3.8.

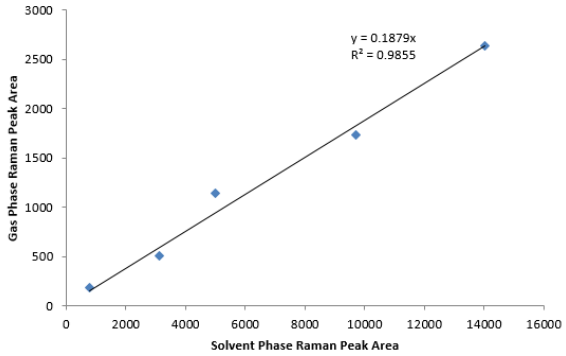

Figure 3.8: Raman peak areas for CO_2-Selexol® system at room temperature

A linear regression is performed with a y-intercept constrained to be zero, and the slope, m, is related to the Henry's Law constant through Equation 3.3.

$$K_H^{cc} = C_{CO_2,g}/C_{CO_2,s} = m * (\sigma_{CO_2,s}/\sigma_{CO_2,g}) \tag{3.3}$$

The cross section enhancement factor can be related to the refractive index of CO_2 and the solvent through Equation 3.4.

$$\sigma_{CO_2,s}/\sigma_{CO_2,g} = ((n_{CO_2}^2 + 2)/((n_{CO_2}/n_{solv})^2 + 2))^4 \tag{3.4}$$

Equation 3.4 is meant for a liquid solute molecule. Since CO_2 and H_2 are gases at room temperature and pressure, an effective n is calculated for both using the Clausius-Mosotti equation as outlined in Berger et. al. which results in values of 1.18 for n_{CO_2} and 1.12 for n_{H_2}.[56] The refractive index of the hybrid solvent and the Selexol® were measured at room temperature and 40 °C using a Reichert AR7 Series Automatic Refractometer. The refractive index of the Selexol® was 1.4355 at room temperature and 1.4282 at 40 °C, and the refractive index of the hybrid was 1.4209 at room temperature, and 1.4125 at 40 °C. The values at 100 °C were then calculated through linear extrapolation due to the limited measurement temperature range of the refractometer.

3.3 Results and Discussion

3.3.1 CO_2 Solubility

Raman spectra of the PDMS-PEGDME hybrid solvent in equilibrium with atmospheric conditions up to 40 bar of CO_2 taken at room temperature are shown in Figure 3.9.

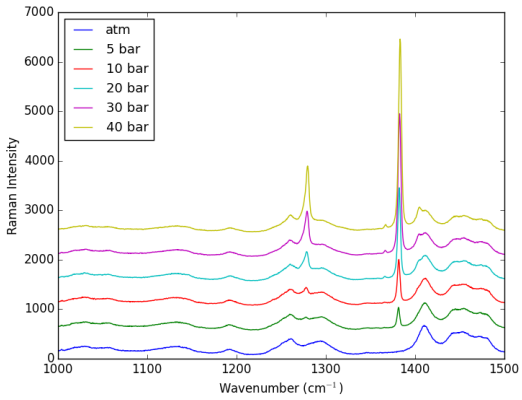

Figure 3.9: Raman spectra for PDMS-PEGDME hybrid in equilibrium with CO_2 up to 40 bar at room temperature

Two peaks attributed to the Fermi diad of CO_2 dissolved in the solvent can be seen in all spectra when the solvent is in equilibrium with 5-40 bar CO_2. These peaks are located at 1279 and 1383 cm^{-1} and both increase in intensity with increasing CO_2 pressure. Comparison with the Raman spectrum of the hybrid under atmospheric conditions revealed no additional peaks as a result of CO_2 exposure. Due to the stronger intensity, the evolution of the peak located at 1383 cm^{-1} was used to quantify the CO_2 solubility. The CO_2 solubility was expressed as a dimensionless Henry's Law constant according to Equation 3.3. By this definition a solvent with a higher CO_2 solubility will exhibit a lower Henry's Law constant of this form. Measurements were conducted at room temperature (23 °C) for the PDMS-PEGDME hybrid solvent as well as for Selexol® and a PDMS with a molecular weight of 550 for comparison.

The hybrid solvent's solubility was measured with 3 independent dupilicate capillary samples to demonstrate the reproducibility of the measurement. The room temperature Henry's Law constants are reported in Table 3.1 .

Table 3.1: Henry's Law Constants for CO_2-Hybrid, CO_2-Selexol®, CO_2-PDMS at 23 °C. Errors are reported as 95% confidence intervals

Solvent	K_H^{cc}
Selexol®	0.486 +- 0.047
PDMS (MW = 550)	0.574 +- 0.030
PDMS-PEGDME Hybrid (1)	0.455 +- 0.032
PDMS-PEGDME Hybrid (2)	0.424 +- 0.058
PDMS-PEGDME Hybrid (3)	0.456 +- 0.059

As can be seen above, repeated measurement of the hybrid's solubility demonstrates a high degree of reproducibility in the Raman solubility measurement method. A comparison between the three solvents also demonstrates that the PDMS-PEGDME hybrid's CO_2 solubility is greater than PDMS and is very comparable to the Selexol® solvent. Measurements were also conducted for the PDMS-PEGDME hybrid solvent at 40 and 100 ° C to gather information about the hybrid's thermodynamics. The Henry's Law constant at 23, 40, and 100 °C for the PDMS-PEGDME hybrid can be seen in Figure 3.10.

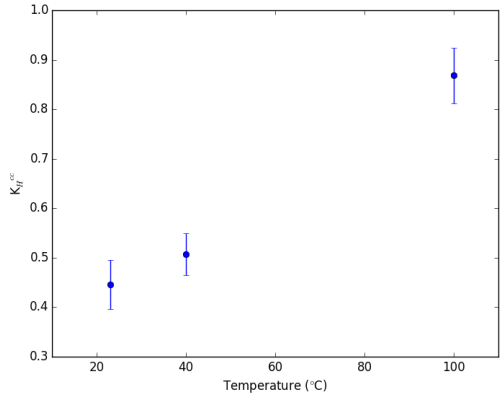

Figure 3.10: Temperature dependence of Henry's Law constant for hybrid-CO_2

As is also the case for Selexol®,[57] the CO_2 solubility of the PDMS-PEGDME hybrid decreases with increasing temperature, i.e. the absorption of CO_2 in the hybrid is exothermic. The variation of the Henry's Law constant with temperature is commonly modeled with the van't Hoff expression 3.5.

$$ln(K_{H1}^{cc}/K_{H2}^{cc}) = (\Delta H/R) * (1/T_2 - 1/T_1) \tag{3.5}$$

In keeping with the van't Hoff equation, the enthalpy of solution is expressed as $\Delta H = R * \frac{\partial ln(K_H^{cc})}{\partial(1/T)}$. The total heat associated with the absorption of a gas into a liquid with no chemical reaction can be described as the combination of a heat of solution and a heat of mixing. The enthalpy change in Equation 3.5 is the heat of solution (i.e. the enthalpy change associated with 1 mole of solute combining with a solvent to form a solution). Applying this model to the experimental data in Figure 3.10 results in an enthalpy of CO_2 solubility for the PDMS-PEGDME hybrid of -8.14 +-0.91 kJ/mol at a 95% confidence level. This value is less exothermic than previously reported for glycol ethers (as well as Selexol®) in the range of -10 to -15 kJ/mol.[58] This suggests that the combination of the PDMS and PEGDME monomer structures in the hybrid results in improved absorption at high temperatures in comparison with Selexol® not just because of increased hydrophobicity but also due to more favorable dissolution thermodynamics as well.

3.3.2 H_2 Solubility

Raman spectra of the PDMS-PEGDME hybrid in equilibrium with atmospheric conditions up to 40 bar of H_2 at room temperature can be seen in Figure 3.11.

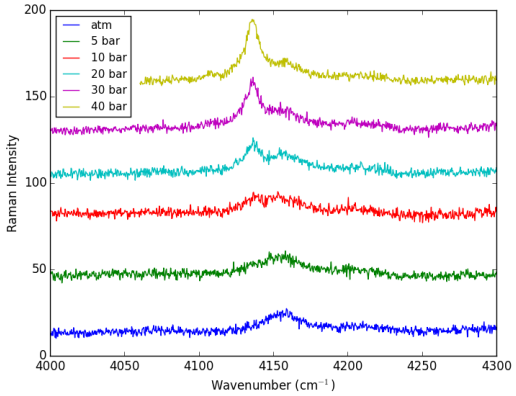

Figure 3.11: Raman spectra for PDMS-PEGDME hybrid in equilibrium with H_2 up to 40 bar at room temperature

A broad peak at 4135 cm^{-1} is evident in all the spectra at pressures of 20 bar or greater. This peak grows in intensity with increasing H_2 pressure and is the only evidence of dissolved H_2 species that can be observed from the Raman spectra. These observations are very similar to what can be observed in the Raman spectra of Selexol® in equilibrium with H_2 as can be found in the above methods section. The evolution of the intensity of this peak was tracked for five different pressures within the range of 20 to 40 bar. The Henry's Law analysis was performed using this peak and the same procedure as used for CO_2 with modifications described above. The solubility of H_2 was measured for the PDMS-PEGDME hybrid at 23, 40, and 100 ° C, and for Selexol® at 23 and 100 ° C. The Henry's Law constants, defined by Equation 3.3 , can be seen in Figure 3.12.

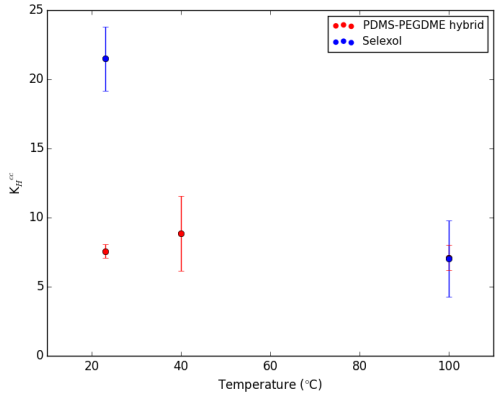

Figure 3.12: Temperature dependence of Henry's Law constant for PDMS-PEGDME hybrid-H_2 and Selexol®-H_2

A comparison between Figure 3.12 and Table 3.1 and Figure 3.10 shows that the H_2 solubility of both the PDMS-PEGDME hybrid and the Selexol® solvents are significantly (1-2 orders of magnitude) lower than their respective CO_2 solubilities. The H_2 solubility of the two solvents do not exhibit the same temperature dependence. Within a 95% confidence interval, the H_2 solubility of the PDMS-PEGDME hybrid solvent does not change significantly between 23 and 100 ° C. The H_2 solubility of Selexol®, on the other hand, increases by a factor of 3 when the temperature is increased from 23 to 100 ° C. This endothermic behavior for H_2 absorption and the exothermic nature of CO_2 absorption in Selexol® both contribute to the CO_2/H_2 selectivity of Selexol® decreasing with increasing temperature.[53] As implementation of the PDMS-PEGDME hybrid to improve upon Selexol® entails absorption with the hybrid at higher temperature, the fact that the H_2 solubilities of the PDMS-PEGDME hybrid and the Selexol® at 100 °C are nearly identical is a very important observation.

3.3.3 Absorption from CO_2 / H_2 mixed gas

In the above sections, the solubility of CO_2 was measured using a pure CO_2 gas and the solubility of H_2 was measured using pure H_2. In an industrial pre-combustion capture gas stream, post water-gas shift, the composition is approximately 40% CO_2 and 55% H_2. To assess whether the presence of H_2 affects the solubility of CO_2 in the PDMS-PEGDME hybrid and vice versa a set of solubility experiments were performed using a 50 vol% CO_2, 50 vol% H_2 mixed gas at 23, 40, and 100 °C and at total pressures up to 60 bar. Since the spectral features associated with gaseous and dissolved CO_2 are found at completely different regions of the Raman spectrum than those of gaseous and dissolved H_2, the Henry's Law analysis described above can be performed for H_2 and CO_2 independently and in parallel and without any additional experimental measurement time than as was done for pure CO_2 or H_2 gas. The Henry's Law constant for the PDMS-PEGDME hybrid and CO_2 can be seen in Figure 3.14.

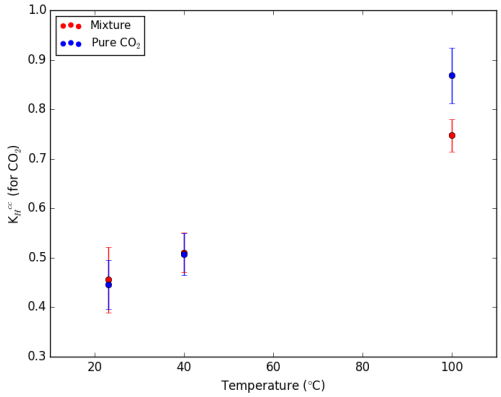

Figure 3.13: Henry's Law constants for PDMS-PEGDME hybrid and CO_2 using a pure CO_2 gas and a 50/50 CO_2/H_2 mixed gas

The close agreement between the Henry's Law constants measured using a pure CO_2 gas and a 50/50 CO_2/H_2 mixture indicates that the CO_2 solubility

of the PDMS-PEGDME hybrid is not affected significantly by the presence of H_2. The Henry's Law constants for the hybrid and H_2 was also calculated and can be seen in Figure 3.14.

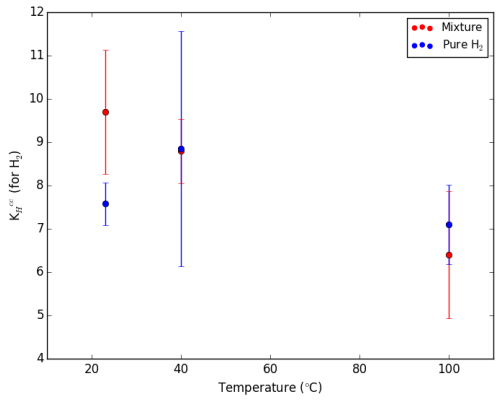

Figure 3.14: Henry's Law constants for PDMS-PEGDME hybrid and H_2 using a pure H_2 gas and a 50/50 CO_2/H_2 mixed gas

Based on a 95% confidence interval, indicated by the error bars, the presence of CO_2 does not appear to have a statistically significant effect on the solubility of H_2. The Henry's Law constant for the hybrid with H_2 appears to decrease with increasing temperature indicating that the absorption of H_2 in the hybrid, similar to the case of Selexol®, is endothermic.

3.4 Conclusions

The CO_2 and H_2 solubilities of a hydrophobic PDMS-PEGDME hybrid solvent were measured in this work and compared with Selexol®. The gas solubilities were expressed in terms of a dimensionless Henry's Law constant, Equation 3.2 , and measured for a range of temperatures up to 100 °C using a Raman spectroscopic technique and a fused silica pressure cell using <5 μL of solvent per sample. The CO_2 solubility of the PDMS-PEGDME hybrid

was found to be significantly greater than PDMS and comparable to Selexol® at room temperature. The enthalpy of solution was determined by applying a van't Hoff expression to the $K_H^{cc}(T)$ data and found to be -8.14 +-0.91 kJ/mol for the PDMS-PEGDME hybrid. This suggests that while CO_2 absorption is exothermic in both Selexol® and the PDMS-PEGDME hybrid, it is less exothermic in the case of the hybrid. The H_2 solubility of the PDMS-PEGDME was also found to be quite low and similar in magnitude to the H_2 solubility of Selexol®. While the H_2 solubilities followed an endothermic trend with temperature for the case of Selexol®, the Henry's Law constant for the H_2-PDMS-PEGDME hybrid system did not vary significantly between 23 and 100 °C. The solubility of H_2 and CO_2 was also determined for the PDMS-PEGDME hybrid solvent using a 50/50 H_2/CO_2 mixture. The solubility of either gas was not significantly affected by the presence of the other gas. These results suggest that the CO_2 and H_2 absorption characteristics of the PDMS-PEGDME hybrid are comparable with Selexol® which is an important benchmark for pre-combustion CO_2 capture viability.

Lastly, the work in this chapter is a very effective example of the application of a micro-scale physical absorption characterization technique to the evaluation of a novel candidate solvent using μL volumes of solvent. While the fused-silica capillary pressure cell and Raman spectroscopic method described in this chapter is most suitable to non-CO_2-reactive solvents, microscale and milliscale measurement techniques for determining the CO_2 absorption capacity of a CO_2-reactive solvent are equally as valuable for evaluating novel post-combustion CO_2 capture solvents as the Raman technique was for evaluating the PDMS-PEGDME hybrid for pre-combustion CO_2 capture. The following chapter will introduce and

describe the use of a glass microfluidic reactor to the measurement of CO_2 absorption capacity and rate of amines.

4 Comparative Microfluidic Screening of Amino Acid Salt Solutions for Post-combustion CO_2 Capture

4.1 Introduction

As described in Chapter 1, the most mature technology for post-combustion CO_2 capture is absorption via an aqueous alkanolamine solution, most commonly 30 wt% monoethanolamine (MEA), using an absorber and stripper to capture CO_2 cyclically with a thermal swing.[7] Amines, including MEA, react reversibly and exothermically with CO_2 to form an amine-CO_2 complex. This complex is typically either a carbamate or a bicarbonate depending on the structure of the amine, with primary and secondary amines preferring the formation of carbamate.[48] While MEA is the industry standard due to its fast reaction kinetics and high CO_2 capacity, there are several drawbacks to its use, including a high regeneration energy cost, solvent loss to oxidative degradation[14] and volatility,[13] as well as its high toxicity and corrosivity. Consequently, a major focus of current research is focused on alternative aqueous-based solvents containing piperazine,[16] promoted carbonate solutions,[17–19] and aqueous amino acid salt solutions[20–23] among others. An alternative approach that has been investigated for a non-aqueous solvent include amine-functionalized ionic liquids.[24]

Great interest has been generated in aqueous solutions of amino acid salts as a class of post-combustion CO_2 capture solvents because they have many favorable characteristics. Dissolved amino acids at neutral pH exist in the form of a zwitterion as seen in equation (4.1).

$$H_3{}^+N{-}CHR{-}COO^- \tag{4.1}$$

Consequently, the amine group of the amino acid is protonated and unavailable to react with CO_2. However, deprotonating the amine group with a metal hydroxide to form a salt (equation (4.2)) allows CO_2 to react with the amino acid along amine-CO_2 reaction pathways.

$$H_2N{-}CHR{-}COO^-M^+ \tag{4.2}$$

We refer to the salt of lysine as lysinate (LYS), the salt of glycine as glycinate (GLY), the salt of taurine as taurinate (TAU), and the salt of proline as prolinate (PRO). Potassium is the most commonly reported cation for CO_2 capture studies.[59]

Aqueous amino acid salt solutions have very low volatility (of the amino acids) and high surface tension due to their ionic nature. They react with CO_2 through the same amine functional groups present in alkanolamines. They have been shown to exhibit excellent oxidative and thermal stability as well as similar capture capacity and kinetics to alkanolamines.[60–62] Additionally, they are naturally abundant and the R-group presents tunability to the solvent selection. Consequently many investigations have been carried out to assess the efficacy of amino acid salt solutions for CO_2 capture.

Holst et. al. investigated the kinetics of several aqueous solutions of amino acid salts including those of 6-aminohexanoic acid, beta-alanine, L-arginine, L-

glutamic acid, DL-methionine, L-proline, and sarcosine.[21] Kinetic experiments were carried out in a closed stirred-cell reactor at a temperature of 298 K and an amino acid salt concentration of 0.5 M. The potassium salts of L-proline and sarcosine were found to be most promising due to their fast kinetics and low pKa.

Kumar et. al. measured the kinetics of the reaction of CO_2 with aqueous potassium salts of taurine and of glycine using a stirred cell reactor with a flat gas-liquid interface.[63] They found that the experimental data could be explained with the same zwitterion mechanism used to interpret the kinetics of CO_2 absorption with primary alkanolamines despite a few differences in kinetic behavior. Unlike for alkanolamines, the partial reaction order in amino acid salt changes from one at low salt concentration to approximately 1.5 at high salt concentration (as high as 3 M). Additionally the forward second order rate constant of the zwitterion mechanism was found to be significantly higher for the amino acid salts than for alkanolamines with similar basicity. Lastly, it was also found that water makes a larger contribution to the deprotonation of the zwitterion in the case of amino acids in comparison to alkanolamines.

More recently, the kinetics of CO_2 absorption in an aqueous solution of potassium prolinate were measured with a wetted wall reactor.[22] In this work, the authors reported higher second order rate constants for this solvent than for some alkanolamines, and for some other amino acid salts.

Aqueous amino acid salt solutions have also been investigated both experimentally and computationally at the process scale. Siemens has developed a post-combustion CO_2 capture process based on the use of an amino acid salt solution.[20] Process models were used to optimize the CO_2 capture process and predicted an efficiency loss of only 9% in comparison to a standard coal-fired plant.[20] A pilot plant was commissioned to start

process validation and solvent optimization in August, 2009.[20] Knuutila et. al. also investigated the potassium salt of sarcosine with a series of pilot plant experiments and simulations for a salt concentration of 3.5 M. Their results indicated a high absorption rate and high energy requirement for the amino acid salt solution in comparison with 30wt% MEA.[64]

One group of amino acids which has received limited attention are the amino acids with basic side-chains, such as histidine, arginine, and lysine. These amino acids contain additional nitrogen group(s) which, depending on the solution conditions (pH), can participate in the reactions with CO_2 increasing the rich CO_2 loading of the solvent. Past work has shown for the case of arginine that the rich CO_2 loading is on order 1 mole CO_2 per mole of arginine, but at the expense of a higher lean CO_2 loading and consequently a working capacity not significantly different from single amine containing molecules such as MEA.[65] Lysine is another amino acid which has only been included in one previous study that showed it to be very promising to replace and improve upon MEA.[66] Consequently the present work aims to further compare the CO_2 absorption of LYS with MEA and three other amino acid salts that have received extensive attention: GLY, PRO, and the synthetic amino acid salt: TAU. The structures of each amino acid can be seen in Figure 4.1.

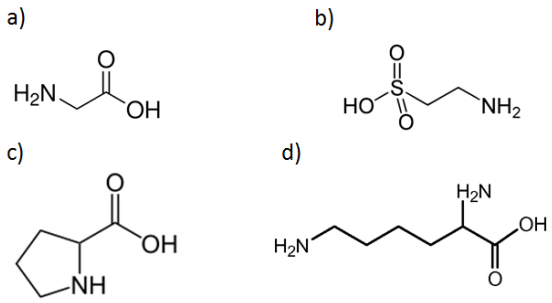

Figure 4.1: Molecular structure of a) Glycine, b) Taurine, c) Proline, d) Lysine.

Multi-phase microfluidic reactors have recently garnered much attention for the study of rapid chemical reactions. Microfluidic devices have been used in several recent studies on CO_2 physical solubility and mass transfer rate in pre-combustion capture solvents[67–70] as well as CO_2 absorption by amines.[71–75] Absorption at microfluidic length-scales occurs through a well-defined two-phase interface and with a high surface area to volume ratio. In addition to the low, 1 mL or less, volume requirements, microfluidic experiments also significantly reduce the time and complexity of CO_2 absorption experiments over conventional methods such as wetted-wall column and stirred cell reactor experiments. Consequently microfluidics is a very appropriate tool for screening new CO_2 absorbent solutions. The present work in this chapter will determine the CO_2 uptake of the aqueous amino acid salt solutions through the time dependent decrease in the volume of entrained CO_2 plugs in a microfluidic channel. A majority of this work has been published in Hallenbeck et. al.[76]

4.2 Materials and Methods

Amino acids were purchased from Sigma Aldrich at purities of at least 98.5%, potassium hydroxide was purchased with a purity of 99.9%, and MEA was purchased with a purity of 99%. All reagents were used without further purification. Deionized water was used for all solutions. Amino acid salt solutions were prepared by neutralizing the amino acid with an equimolar amount of potassium hydroxide. The actual concentration of the aqueous amino acid salt was verified through titration with a 12.1 N HCl solution (Fischer Scientific) using an Orion 4star pH meter. The concentrations of all solutions were 0.50M with the exception of potassium lysinate which was 0.53 M. CO_2 gas was supplied from a cylinder (Matheson gas) at a 99.995% purity.

4.2.1 Microfluidic apparatus

Microfluidic experiments were carried out with a commercially available all-glass microreactor from Micronit (product code:FC-R150.676.2_PACK). The reactor contains two inlets, a Y-junction, and a serpentine channel. All inlet and outlet connections were made with the Fluidic Connect Pro chip holder purchased from Micronit (product code: FC_PRO_CH4515). The flow rate of liquid into one inlet was controlled with a Harvard apparatus phd2000 syringe pump and gas was supplied to the other inlet with a ControlAir type 550x electronic to pneumatic transducer with a supply pressure range of 35-100 psig and an outlet pressure range of 0-30psig. Experiments were conducted on a light table with a Nikon Motion pro-x high speed camera. The (inlet) gas pressure was kept constant at 1.7 atm for all experiments and the liquid flow rate was adjusted in each experiment to obtain a steady production of entrained gaseous plugs at the Y-junction of the microfluidic device as can be seen in Figure 4.2.

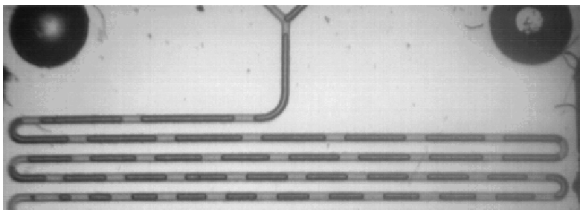

Figure 4.2: Example image used for analysis of 0.50 M K^+GLY^-

In each experiment a video was acquired with a frame rate of 500 Hz. This frame rate is sufficiently high to allow for the tracking of the size of an individual gas plug through time as it travels through the reactor. In order to measure the amount of absorbed CO_2, the length of an individual gas plug was measured as the gas plug traveled along the reactor channel using the ImageJ software and can be seen in Figure 4.3. The gas plug was selected to maintain

a constant adjacent liquid slug length (approximately 350 μm) between all experiments.

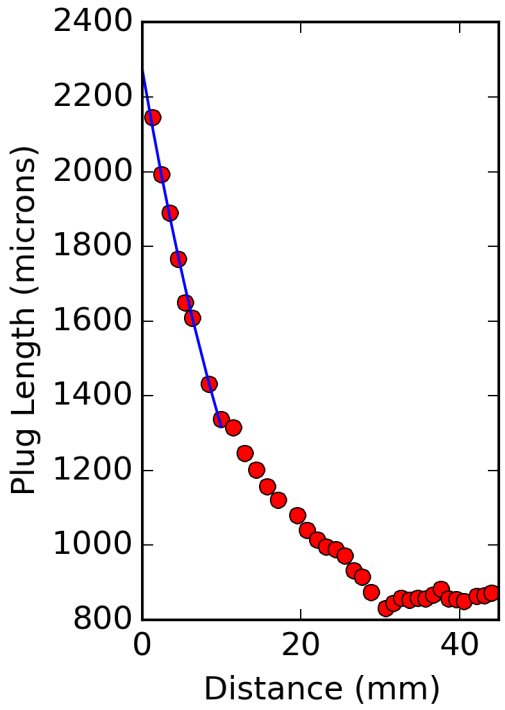

Figure 4.3: Plug length vs distance used for analysis of 0.50 M K^+GLY^- with exponential fit for determining initial plug length. The initial gas plug length was determined to be 2276 μm

The initial gas plug length was determined by extrapolating the gas plug length to the y-junction through an exponential fit as can be seen in Figure 4.3. The volume of a gas plug was calculated assuming a plug consisting of a cylinder and two hemispherical endcaps. Previous work[71] with the same microreactor determined the hydraulic diameter of the microchannel to be 125 μm through confocal fluorescence microscopy. We assumed the hydraulic diameter of each gas plug to be 121 μm to account for the thin liquid film between the plug and reactor walls as was done in Li et. al. The moles of absorbed CO_2 was then determined by applying the ideal gas law based on the measured ambient temperature (294-296 K) and an approximated linear

pressure drop across the microreactor. The precision of the resulting concentration data is within 0.02 M based on propagating the precision of the plug and slug length measurements.

4.2.2 Raman spectroscopy

Raman spectroscopy was carried out with the prepared absorbent solutions prior to microfluidic experiments and with a sample of the microreactor effluent following each microfluidic experiment. Raman spectra were acquired with a Horiba LabRamHR spectrometer using a Spectra Physics 532nm Nd:Yag laser with an operating power of 0.2 W as the excitation source. Spectra were taken using an Olympus 50xLWD objective and were recorded as an average of 10 three second exposures over each spectral range. Prior to each set of measurements, the spectrometer was calibrated using a silicon standard.

4.2.3 CSTR

The CO_2 absorption testing unit is a continuously stirred reactor vessel (300 ml EZE-Seal Stirred Reactor from Autoclave Engineers). It is equipped with a set of mass flow controllers (MFCs) allowing for control of up to five different gases/mixtures, which can be blended and directed into a single gas inlet port at the top of the reactor. Gases are introduced into the reactor via a diptube connected to the gas inlet port. Solvent is pre-loaded into the vessel, where it is continuously stirred with the impeller for adequate mixing and mass transfer. Gaseous products exit the reactor at the top through a single gas outlet port and are immediately directed into a cold trap to condense out the vapor leaving the reactor with the gases. After the cold trap, the gas stream passes through a back pressure regulator (BPR) prior to being vented. A slipstream of the gas stream is constantly being withdrawn via a

capillary connection for gas analysis by a Dycor® series Dymaxion Residual Gas Analyzer (RGA) from AMETEK.

For equilibrium CO_2 absorption measurements, the solvent is loaded into the vessel and sealed. N_2 gas is briefly directed into the vessel to purge air/O_2 from the system. The vessel is then isolated while the solvent is constantly stirred as it is gradually brought up to the 40 °C absorption temperature with the heater. At the same time the gas feed, now bypassing the vessel, is changed to 14% CO_2/N_2 at the desired flow rate to establish steady flow as measured by the RGA. When both the absorption temperature and flow rate is attained, the vessel is brought back online to start the absorption test. The solvent is saturated and equilibrium reached when the concentration of gas exiting the vessel is equal to the initial concentration as recorded by the RGA. The RGA data is reduced and numerically integrated to calculate the amount of CO_2 absorbed by the solvent.

4.3 Results

4.3.1 Microfluidic Experiments

Microfluidic absorption experiments were carried out at ambient temperature with a gas delivery pressure of 1.7 atm for MEA and GLY, TAU, PRO at a concentration of 0.50 M and for LYS at a concentration of 0.53 M. The size of a specific CO_2 gas plug was monitored as a function of time starting at the Y-junction and the molar concentration of absorbed CO_2 in the adjacent liquid slugs was calculated as described above. The resulting concentration of absorbed CO_2 can be seen in Figure 4.4 for all of the studied solutions.

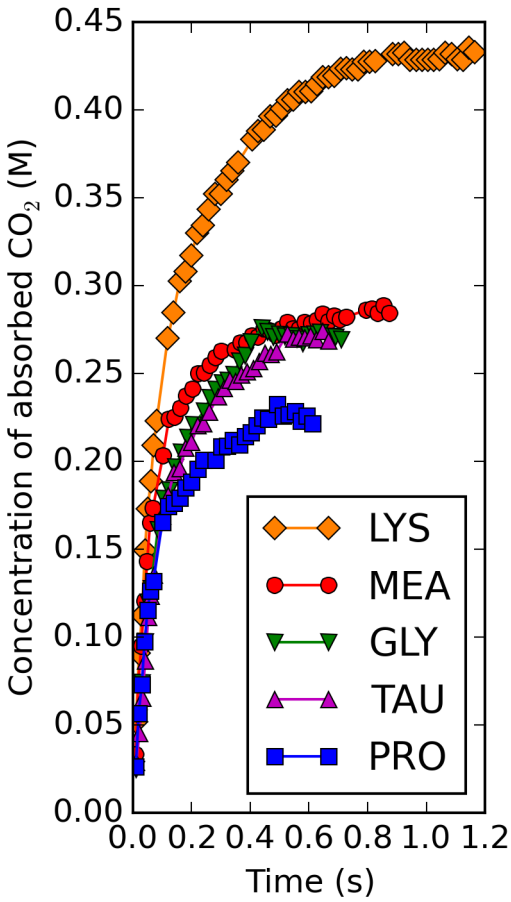

Figure 4.4: Concentration of absorbed CO_2 during microfluidic experiments as a function of time.

Since the partial pressure of CO_2 is significantly lower in the typical post-combustion flue gas, the physical solubility of CO_2 in the amine solution is typically negligible. Consequently, the reacted CO_2 loading in the microfluidic experiments was calculated by approximating the physical solubility of CO_2 in the amine or amino acid salt solution with that of water. The CO_2 loadings after subtracting the physical solubility can be seen below in Table 4.1.

Table 4.1: Maximum reacted CO_2 loadings during MF experiments.

Solvent	CO_2 loading (mol CO_2/mol Am)
LYS	0.70
MEA	0.46
GLY	0.43
TAU	0.43
PRO	0.34

As an arbitrary metric for comparing the absorption rates, the time to reach 90% of the above maximum CO_2 loadings was measured and can be seen in Table 4.2.

Table 4.2: Time to reach 90% of maximum CO_2 loading during MF experiments.

Solvent	t (s)
MEA	0.30
GLY	0.34
PRO	0.34
TAU	0.37
LYS	0.47

Another metric for comparing the absorption rates is to compare the initial absorption flux (Table 4.3) as calculated over the initial 0.02 s of the absorption assuming the mass transfer area is approximately the area of the endcaps of the gas plug.

Table 4.3: Initial Absorption flux during MF experiments.

Solvent	Initial absorption flux (mol*m^{-2}*s^{-1})
LYS	0.52
MEA	0.48
PRO	0.35
GLY	0.32
TAU	0.25

4.3.2 CSTR

In order to determine the effectiveness of the microfluidic experiments in predicting the trends in CO_2 loading and rate at larger macroscale and industrially relevant volumes and solvent concentrations a set of equilibrium CO_2 absorption experiments were conducted with a 300 mL CSTR. The equilibrium CO_2 absorption capacities of potassium lysinate and MEA were determined from integration of the CO_2 breakthrough curves. Samples of the same composition as in the microfluidic experiments were measured as well as a 30 wt% MEA solution and 1.48 M (or equivalently 70 wt% H_2O) potassium lysinate solution in order to compare the two solutions with a constant weight fraction of water. Experiments were conducted at 313.15 K and from a 10 vol% CO_2 gas stream for the low solvent concentration experiments and 14 vol% CO_2, balance N_2, gas stream for the high solvent concentration experiments. The cumulative amount of absorbed CO_2 throughout each experiment can be seen in Figure 4.5 (0.53 M) and Figure 4.6 (70 wt% water).

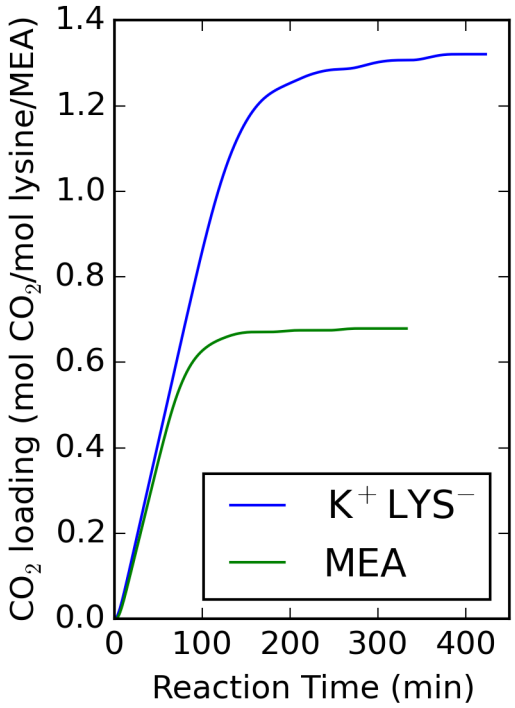

Figure 4.5: Cumulative CO_2 loading throughout CSTR breakthrough for 0.53M K^+LYS^- and MEA.

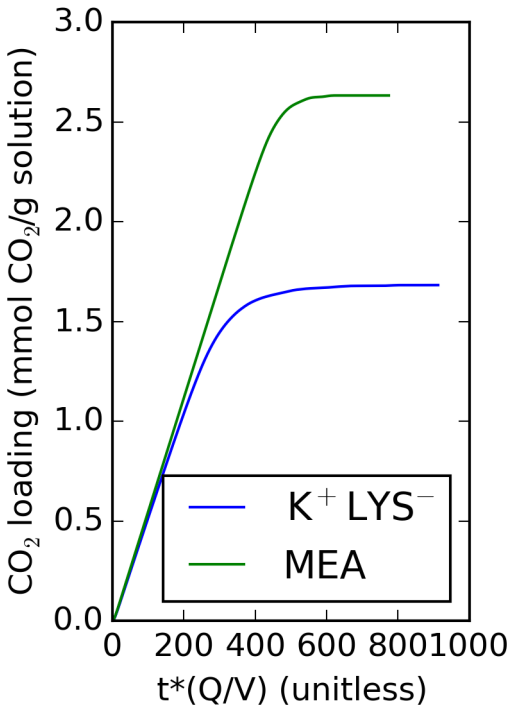

Figure 4.6: Cumulative CO_2 loading throughout CSTR breakthrough for 1.48M K^+LYS^- and 30 wt% MEA.

A comparison of the equilibrium absorption capacities can be seen in Table 4.4.

Table 4.4: Equilibrium CO_2 loadings during CSTR experiments.

Solvent	CO_2 loading mol CO_2/mol MEA/Lysine	CO_2 loading mmol/g solution
0.53M LYS	1.32	0.68
0.53M MEA	0.70	0.37
1.48M LYS	1.19	1.68
30wt% MEA	0.53	2.63

The viscosities of the 1.48 M LYS solution and the 30 wt% MEA solution were determined by a RheoSense micro viscometer. The viscosities were nearly identical as can be seen in Table 4.5 and Table 4.6.

Table 4.5: Viscosity of 1.48M Potassium Lysinate.

Temperature (K)	Viscosity (mPas)
293.14	3.078
293.13	3.069
303.29	2.27
313.21	1.723

Table 4.6: Viscosity of 30 wt% MEA.

Temperature (K)	Viscosity (mPas)
293.17	3.159
293.16	3.161
303.22	2.277
313.03	1.751

These values are consistent with previously reported viscosity measurements of 30 wt% MEA solution.[77]

4.3.3 Raman spectroscopy

Raman spectra for each absorbent solution both before and after absorbing CO_2 in the microfluidic reactor can be seen below in Figures 4.7 — 4.11.

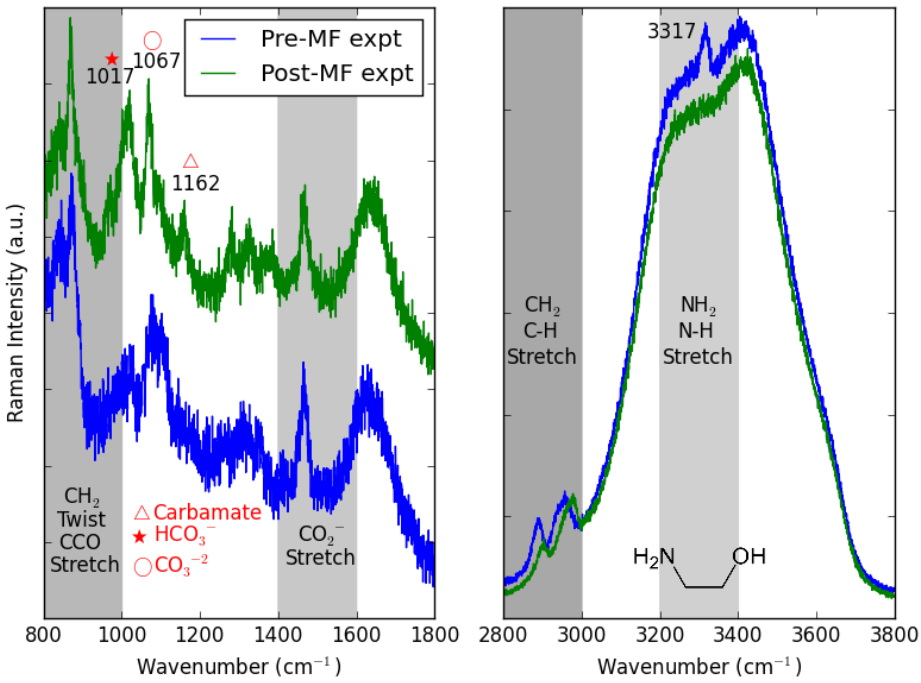

Figure 4.7: Raman Spectra for MEA.

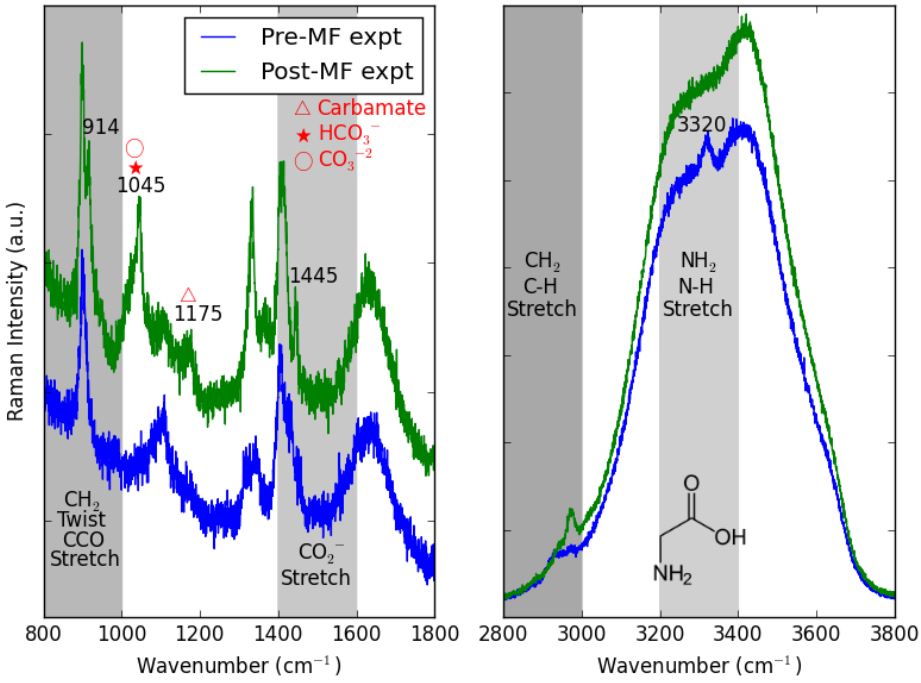

Figure 4.8: Raman Spectra for GLY.

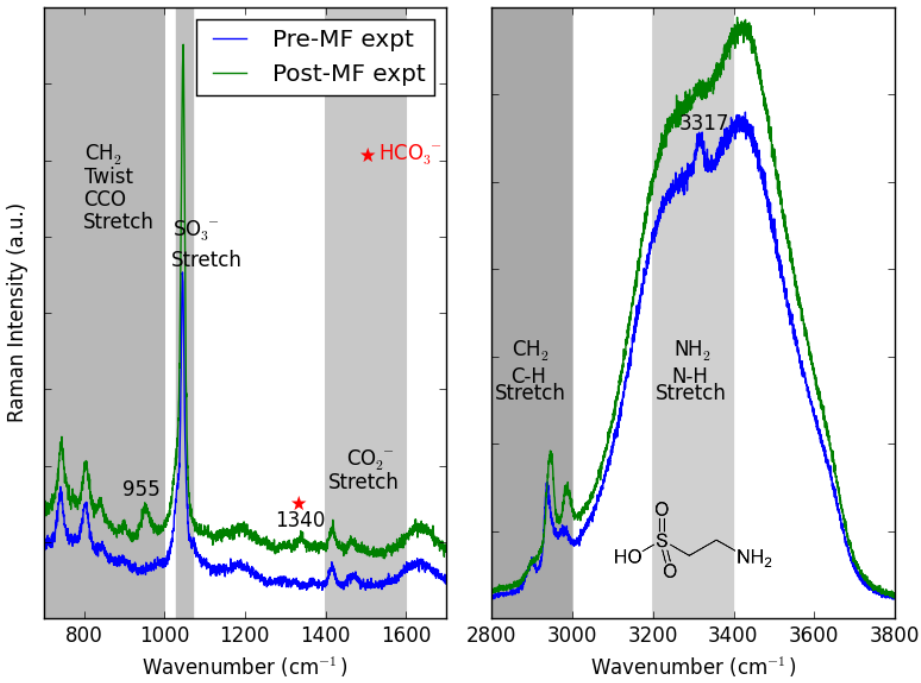

Figure 4.9: Raman Spectra for TAU.

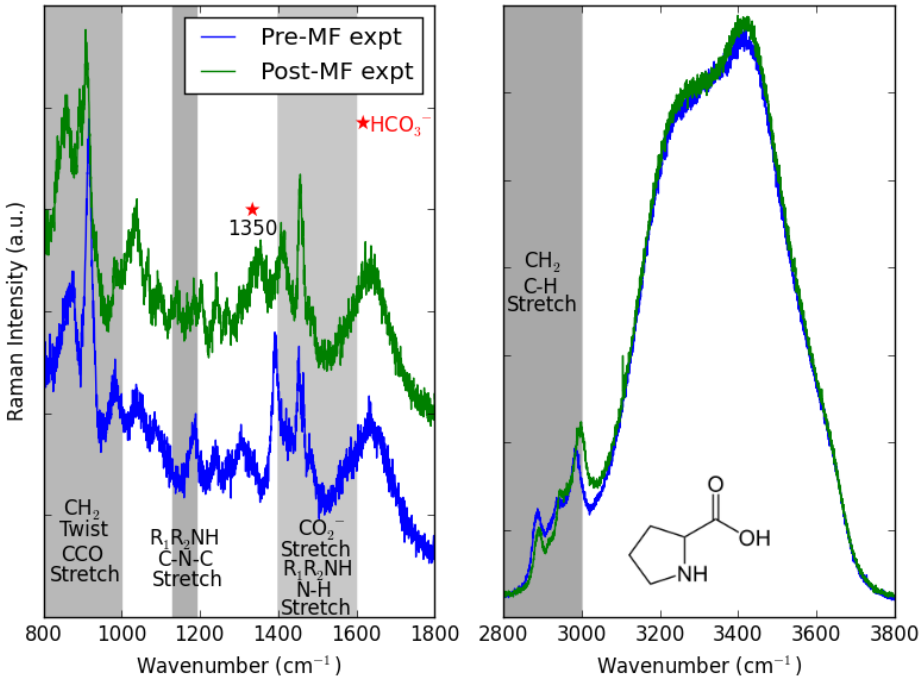

Figure 4.10: Raman Spectra for PRO.

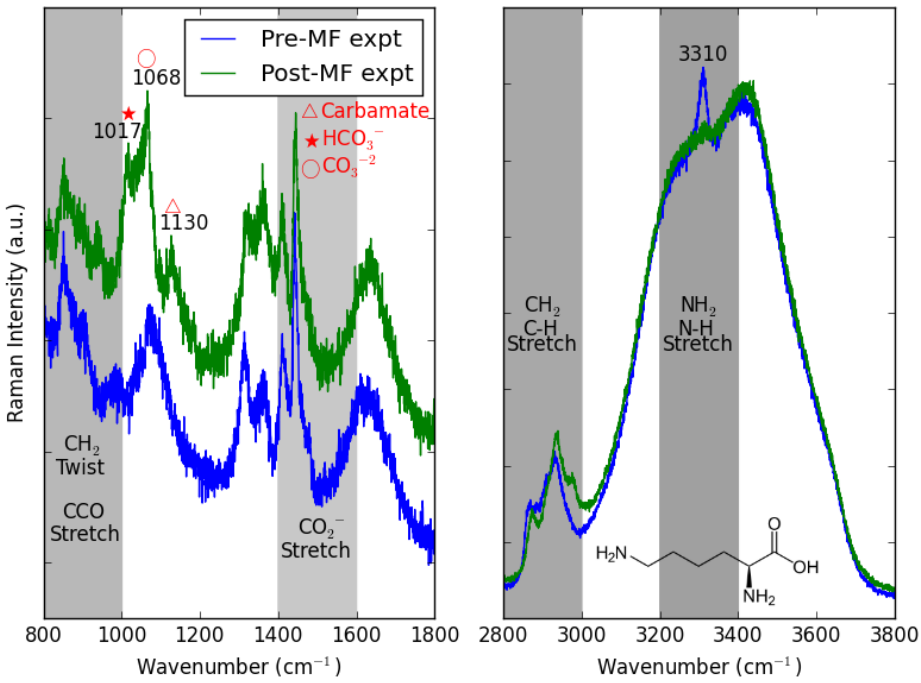

Figure 4.11: Raman Spectra for LYS.

4.4 Discussion

Microfluidic absorption experiments provide a rapid, low-volume, and direct quantitative comparison of the CO_2 absorption capacity and absorption rate between several absorbent solutions. The results of this set of experiments shows that the potassium salt of lysine absorbs more CO_2 than the potassium salts of glycine, taurine, or proline as well as more than MEA at the same molar absorbent concentration. This result suggests that the additional primary amine in lysine's side chain contributes additional CO_2 capacity through additional reaction with CO_2 over the solutions containing a solitary amine group per absorbent molecule. However, comparison between lysine and glycine shows that doubling the number of primary amine groups in the amino acid molecule results in less than a doubling in CO_2 uptake. This is not surprising due to the high pK_a(10.53) of the lysine

side chain, so as CO_2 is absorbed the decrease in solution pH (initially 11.58) can result in protonation of some of the amine groups and decrease the availability for reaction with CO_2. Never the less the potassium salt of lysine has exhibited a rich CO_2 loading >50% greater than MEA. Consequently we suggest that lysine should receive more attention than the small number of studies[66] it has been included in to date. The potassium salts of glycine and taurine exhibited similar capacity to MEA, while prolinate exhibited the lowest CO_2 capacity. This suggests that the secondary amine group of proline does not lead to an increase in the amount of bicarbonate versus carbamate formed over the cases of the primary amines. Steric hindrance effects may be a contributing factor to the lower rich CO_2 loading of PRO.

While LYS exhibited a slightly longer time to reach its maximum CO_2 loading than the other solutions in this study, the initial absorption rate of LYS was significantly faster than the other amino acid salts and slightly higher than MEA. Which solvent would exhibit the fastest absorption rate in an absorber would vary based on the residence time of CO_2 and the solvent. Certainly at very low residence times, LYS would be an attractive option. The absorption fluxes measured using the microfluidic apparatus are significantly faster than those reported for wetted-wall column experiments (on the order 10^{-5} to 10^{-3} mol/m^{2}s).[16] However that the flux is significantly greater at the microfluidic length scale is not surprising and consistent with past CO_2 absorption results at similar microfluidic length scales that report fluxes in the range of 0.98-1.8 mol/m^{2}s depending on the gas space velocity.[75] This highlights the need to limit the comparison of absolute absorption rates to data collected with the same experimental setup.

LYS also exhibited a higher equilibrium CO_2 absorption capacity than MEA in the CSTR experiments. At the same solvent concentrations as in

the microfluidic experiments, 1.32 mol CO_2/mol lysine was absorbed compared with only 0.68 mol CO_2/mol MEA. These capacities were measured at a higher (40 vs 23 °C) temperature and lower CO_2 gas pressure than in the microfluidic experiments. The fact that both capacities were found to be significantly higher in the CSTR experiment could be an indication that CO_2 plug volume reduction in the microfluidic reactor is partly controlled by mass-transfer. As is the case with comparing the absorption rates, the absolute values of the CO_2 loadings should only be compared between solutions with the same testing method. However, it is most important that the qualitative trend in the absorption capacity between different solvents (LYS and MEA) that was observed in the microfluidic experiment was also observed in the CSTR experiments. Consequently, the microfluidic experiments described in this work provide a volume and time-efficient means to screen several solvents and identify which ones are the most promising candidates based on absorption capacity prior to more time and volume intensive testing, such as in a CSTR, being done. This advantage is particularly relevant for novel solvents that may be costly to produce in liter-scale quantities prior to their CO_2 capture potential being experimentally investigated.

The results in Table 4.4 shows that the trends in CO_2 absorption capacity is dependent on whether the solvents are compared on a constant moles of amine/amino acid basis or constant mass fraction of water basis. Due to the higher molecular weight of lysine vs. MEA, when the molar concentration of lysine and MEA are constant (0.53 M) LYS absorbs more CO_2 than MEA, while when the combined lysine/KOH mass fraction is kept at 30 wt% to match the MEA benchmark, MEA absorbs more CO_2 than LYS. In order to match the CO_2 absorption capacity of 30 wt% MEA, a higher concentration than 1.48

M of potassium lysinate is needed. At higher concentrations, precipitation may introduce additional complexity and to determine the overall effect of replacing MEA with LYS an in-depth analysis would have to be done to take in account the benefits of LYS over MEA (lower volatility, lower corrosivity, lower toxicity, higher CO_2 absorption at same molar concentration of solvent) as well as the drawbacks (higher molecular weight, precipitation of solids). While LYS certainly presents several advantages over MEA, this work also suggests further research into all these competing factors as well as further thermodynamic information regarding regeneration should be done.

Inspection of the Raman spectra of the MEA and amino acid salt solutions before and after CO_2 absorption confirms the occurrence of a reaction and the formation of carbamate, bicarbonate, and carbonate as products. For the primary amines in this study, the occurrence of reaction between CO_2 and the primary amine group is confirmed by the disappearance of the peak at 3310-3320 cm^{-1} which is indicative of N-H stretching in the NH_2 species. In MEA solutions, carbamate, bicarbonate, and carbonate result in peaks at 1162 cm^{-1}, 1017 cm^{-1}, and 1067 cm^{-1} respectively.[78] All three of these peaks are absent in the pre-MF experiment spectrum for MEA and present in the post-MF experiment spectrum. While peaks in the same region appear in some of the post-MF experiment spectra for the amino acid salts, peaks in other areas appear as well. Post-MF GLY exhibits new peaks at 914 and 1445 cm^{-1} in addition to a broad peak (1045 cm^{-1}) in the region of bicarbonate/carbonate in MEA and a 1175 cm^{-1} peak in the region of carbamate in MEA. Post-MF TAU does not exhibit new peaks in the same region as bicarbonate/carbonate/carbamate in MEA or GLY but exhibits only two new peaks at 955 cm^{-1}, in the expected range of 930-1100 cm^{-1} for NH_3^+ rocking and/or the C-N stretch for NH_3^+,[79] and 1340

cm^{-1}. A peak in the similar range of 1340-1360 cm^{-1} also appears for the case of post-MF PRO and is in a similar region as the CO symmetric stretch of bicarbonate.[80,81] The spectrum of prolinate undergoes considerable changes in peak positions as a result of CO_2 absorption and is consequently difficult to interpret further. LYS exhibits very similar new Raman peaks in the post-MF experiment spectrum as MEA and GLY with peaks in the 1010-1070 cm^{-1} region indicative of C-OH stretching in bicarbonate and the symmetric stretch of carbonate[81] as well as at 1130 cm^{-1} indicative of carbamate. The shift of the carbamate peak from 1162 cm^{-1} in MEA and 1175 cm^{-1} in GLY to 1130 cm^{-1} in LYS may indicate a lower bond energy for carbamate in LYS and consequently an equilibrium that favors bicarbonate/carbonate more for the case of LYS than for MEA or GLY.

4.5 Conclusions

The CO_2 absorption capacity and rate of four amino acid salt solutions was evaluated and compared with MEA through analysis of segmented flow in a microfluidic channel. The CO_2 loading of the absorbent solutions was calculated from the decrease in volume of an entrained CO_2 plug as it traveled through the microfluidic reactor using image analysis. The potassium salt of lysine exhibited the highest rich CO_2 loading, >50% higher than MEA. The potassium salts of glycine and taurine exhibited similar rich loadings to MEA, while the potassium salt of proline exhibited the lowest rich CO_2 loading.

The CO_2 absorption capacity of the potassium salt of lysine was then further investigated and compared with MEA in a CSTR. The CSTR results showed that when the molar concentration of MEA and LYS was kept constant at 0.53 M, the LYS solution exhibited a >90% higher CO_2 absorption capacity than MEA. However, when the solvents were compared at a constant mass

fraction instead of constant molar concentration, MEA absorbed more CO_2 due to its lower molecular weight than LYS. Consequently, the effect of differing molecular weights should always be considered when designing experiments to screen the CO_2 absorption capacity of several absorbents.

Raman spectroscopy was used to confirm the occurrence of a reaction and to identify the reaction products. The Raman spectrum of each absorbent solution before the microfluidic experiment was compared with the absorbent solution after exiting the microfluidic reactor. Spectral features consistent with the formation of bicarbonate, carbonate, and carbamate were found for all solutions. The results of this work suggest that the potassium salt of lysine should be further investigated as a post-combustion CO_2 capture solvent since it would enable a greater amount of CO_2 to be absorbed for the same moles of absorbent molecule than is the case for MEA, and it has been largely overlooked in previous amino acid salt solution studies. Due to lysine's large molecular weight, the combined mass fraction of lysine/koh would need to be higher than the 30% that is customary for MEA in order to achieve the same rich CO_2 loading. Determining the optimal capture solution composition for a potassium lysinate process is beyond the scope of the present work. Future investigation of LYS should include regeneration studies, thermal conductivity measurements, and the effect of precipitation in particular. This work also highlights the experimental efficiency and speed of microfluidic reactors as screening tools for evaluating CO_2 absorbents. Trends in CO_2 absorption capacity consistent with those observed in a CSTR can be determined with less than a mL and in substantially shorter time by analyzing images of CO_2 plug dissolution in segmented flow in a microfluidic channel. The measurement of both kinetics and the equilibrium absorption capacity from a single microfluidic experiment was demonstrated in this

chapter for post-combustion capture solvents. For the case of pre-combustion solvents, Chapter 3 demonstrated a microfluidic measurement of CO_2 solubility, i.e. absorption capacity, and Chapter 5 will demonstrate that the same high pressure silica capillary cell can be used to measure CO_2 diffusivity, i.e. absorption rate.

5 Quantitative Measurement of CO_2-Solvent Diffusivity Using Raman Spectroscopy

5.1 Introduction

The design of a pre-combustion CO_2 capture process requires knowledge of several CO_2 absorption characteristics of the solvent. The solvent's CO_2 solubility and the enthalpy of CO_2 dissolution in the solvent was investigated in Chapter 3. The focus of the present chapter is on the diffusivity of CO_2 in the solvent. The diffusivity of CO_2 is not just an important quantity for pre-combustion CO_2 capture, because it directly represents the rate of CO_2 absorption in a physical solvent without a chemical reaction, but also is an important quantity for post-combustion CO_2 capture and CO_2 sequestration as well. In a post-combustion capture solvent that captures CO_2 through a chemical reaction, the diffusivity of CO_2, along with the reaction kinetics, is a contributing variable to the overall mass transfer rate. For the case of CO_2 sequestration through solubility trapping, the diffusivity of CO_2 in the reservoir fluid influences the security and storage capacity of the sequestration site.

A commonly employed method of measuring the diffusion of gases into liquids is through the pressure decay technique using a macroscale pressure-

volume-temperature (PVT) cell.[82] The main advantage of this approach is its simplicity, but there are disadvantages. The required large volumes of solvent would be impractical for acquiring diffusivity data on new solvents which are first only synthesized in very small volumes. The PVT approach also does a poor job in separating diffusive and convective effects in solvents whose density can vary significantly with increased CO_2 concentration (e.g. water) meaning that the measured diffusivity often needs to be reported as an apparent diffusivity that is dependent on the measurement equipment and configuration.[83] Furthermore the pressure decay method also requires long run times on the order of hours due to the large lengths over which diffusion has to occur. The use of a microliter-scale method would address all of these disadvantages of the PVT method.

Recently there has been significant research conducted on microfluidic techniques for measuring the diffusivity of CO_2 in reservoir liquids.[70,84,85] Past literature encompasses several unique microfluidic methods developed for measuring CO_2 diffusivity in a physical solvent. Sell et. al. measured the diffusion coefficient of CO_2 in water and in brine based on the imaging of fluorescence quenching of a pH-dependent dye in the microchannel.[84] Fadaei et. al. measured CO_2 diffusivity in bitumen oil by injecting a plug of bitumen into a CO_2 filled channel and imaging the one-dimensional oil-swelling that occurred in response to CO_2 diffusion using 1 nL plug of oil sample and in approximately 10 minutes.[85] Lefortier et. al. measured CO_2 diffusivity in various physical solvents by imaging segmented flow generated by a T-junction in a similar manner as was done for amine solvents in Chapter 4.[70] The aim of the current chapter is the development of a microliter-scale method for the measurement of CO_2 diffusivity in a physical solvent using Raman spectroscopy and the fused-silica capillary cell method

and apparatus desribed in Chapter 3. This method is first applied to water, a solvent whose CO_2 diffusivity is known in the literature, and then to three polydimethylsiloxane (PDMS) derivatives of varying molecular weight, density, and viscosity.

5.2 Methods

The methodology of measuring CO_2 solubility quantitatively using Raman spectroscopy and a fused silica capillary cell was demonstrated in Chapter 3. This chapter extends this methodology to measuring the evolution of CO_2 solubility through time. A capillary is prepared as in Chapter 3 and the Swagelok apparatus is pressurized to a fixed pressure. The capillary is then opened to the apparatus and Raman spectra of the solvent is acquired at a fixed location away from the gas-liquid interface at known points in time after the head space of the capillary has been pressurized. As CO_2 diffusion into the solvent occurs, the Raman peak of dissolved CO_2 grows in intensity until the equilibrium concentration of CO_2 is reached at the location of spectral acquisition.

The evolution of the dissolved CO_2 peak intensity can be related to the diffusivity of CO_2 in the solvent through a simple analytical model. The radial symmetry of the capillary allows for the diffusion of CO_2 across the gas-liquid interface and into the liquid to be accurately modeled as 1-D Fickian diffusion. Consequently the change in the concentration of dissolved CO_2 as a function of time and distance from the interface can be modeled through Fick's second law (Equation 5.1). The boundary conditions are that initially the CO_2 concentration in the solution is assumed to be zero everywhere (i.e. $C(x,0)=0$), the concentration of CO_2 at the interface is the equilibrium concentration (i.e. $C(0,t>0)=C_0$), and the concentration infinitely far away from the gas-liquid

interface is assumed to be zero for all times (i.e. C(∞,t)=0).

$$\frac{\partial C}{\partial t} = D * \frac{\partial^2 C}{\partial x^2} \tag{5.1}$$

As soon as t>0, CO_2 concentration at the interface instantly changes from 0 to the saturation concentration, C_0, based on the gas phase pressure. The model also assumes that the diffusivity does not vary significantly in response to changes in the CO_2 concentration since the solution is assumed to be sufficiently dilute. Equation 5.1 can be solved by applying the above boundary conditions to yield a concentration profile along the capillary (Equation 5.2).

$$C = C_0 erfc(\frac{x}{\sqrt{4Dt}}) \tag{5.2}$$

The Raman measurements are related through the linear relation, A = σC, where A is the area underneath the dissolved CO_2 Raman peak, and σ is the Raman cross-section of the CO_2 molecule as mentioned in Chapter 3. The motorized microscope stage and fused silica capillary cell allows for the measurement of A(x,t). Equation 5.2 can be simplified to Equation 5.3 provided that the cross-section is kept constant for all spectra (i.e. incident laser intensity, focal length, acquisition exposure time are constant by design).

$$A = A_0 erfc(\frac{x}{\sqrt{4Dt}}) \tag{5.3}$$

A_0 is the Raman peak area of the dissolved CO_2 molecule at equilibrium conditions, and along with D is a fitted parameter. Equation 5.3 is fitted to the A(x,t) data using a 2 parameter non-linear least squares method using the nlinfit MATLAB function.

Raman spectroscopy was carried out on a Horiba LabRamHR spectrometer using a Spectra Physics 532 nm Nd:Yag laser with an operating power of 0.2 W as the excitation source. Spectra were taken using an Olympus 50xLWD objective and were recorded as the average of eight one-second exposures.

5.3 Results and Discussion

5.3.1 Water

The diffusion of CO_2 in water was studied in order to determine the accuracy of the method by comparing the measurements with the literature value of 1.77 *10^{-9} m^2/s at 20 °C.[86] An example of the evolution of the CO_2 peak in water during the course of one experiment can be seen below in Figure 5.1. The stronger of the two peaks of the CO_2 Fermi dyad appears at 1383 cm^{-1} and it is the change in the area underneath this peak as a function of time and distance from the interface that is used to fit a diffusivity.

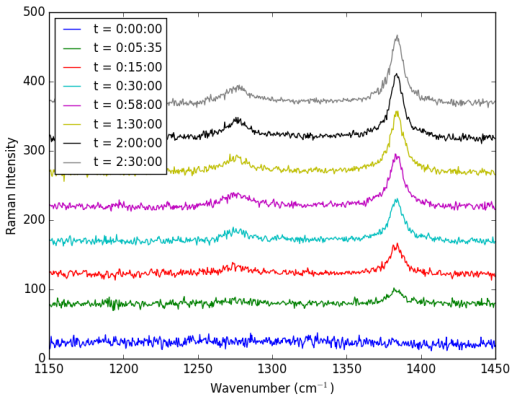

Figure 5.1: Raman Spectra of dissolved CO_2 in water as a function of time (P=40.33 bar,1.12 mm away from gas-liquid interface)

The area underneath the 1383 cm^{-1} peak was determined through numerical integration and Equation 5.3 was applied to fit a diffusivity as can be seen in Figure 5.2.

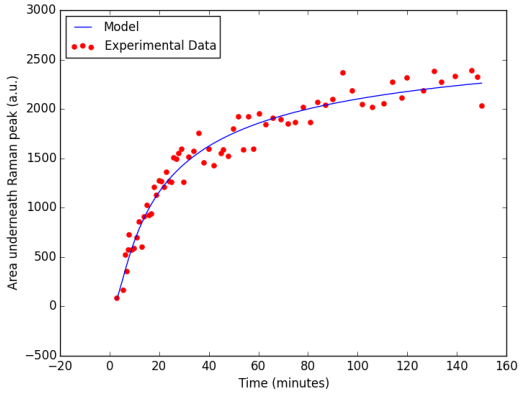

Figure 5.2: Raman Peak Area as a function of time for water (D calculated to be 6.93*10^{-10} m^2/s) (P=40.33 bar,1.12 mm away from gas-liquid interface)

This experiment was repeated a total of 9 times to determine the reproducibility of the diffusivity measurement and the sensitivity of the diffusivity to experimental parameters (pressure, length of liquid sample, measurement location in relation to interface). Figures analogous to Figures 5.1 and 5.2 can be found in Appendix 9. A summary of the results is presented in Table 5.1.

Table 5.1: Calculated Diffusivities of CO_2 in Water (Literature value: 1.77 *10^{-9} m^2/s). Errors are reported as 95% confidence intervals

Appendix #	P (bar)	$L_{solvent}$ (cm)	x (mm)	D (m^2/s) (error)	Fitted A_0
1	30.2	2.41	1.36	5.49*10^{-10} (0.27*10^{-10})	10685
2	20.82	0.95	1.07	2.42*10^{-9} (0.50*10^{-9})	2553
3	40.33	0.57	1.12	6.93*10^{-10} (0.72*10^{-10})	3011
4	20.55	0.44	0.77	2.54*10^{-10} (0.20*10^{-10})	3950
5	19.79	0.43	0.55	1.92*10^{-10} (0.21*10^{-10})	3200
6	20.27	0.49	0.94	2.89*10^{-10} (0.33*10^{-10})	3200
7	20.34	0.95	0.85	3.66*10^{-10} (0.43*10^{-10})	2850
8	20.06	1.11	0.79	3.72*10^{-10} (0.60*10^{-10})	2000
9	20.34	1.22	0.70	3.24*10^{-10} (0.35*10^{-10})	3750

The average calculated diffusivity of CO_2 in water from these experiments was 6.06 * 10^{-10} m^2/s with a standard deviation of 6.97 * 10^{-10} m^2/s. This is 34% of the the literature value. Previous work suggests that in the range of

5-50 bar, the diffusivity of CO_2 in water does not vary.[84] The results presented here are consistent with that conclusion. Additionally, the measured diffusivity values are not highly sensitive to the sample length or measurement position within the range of experimental conditions examined in this study. This error in the measured value is systematic in that it consistently predicts a slower diffusion rate than the previously measured rate for CO_2 in water at 20 °C. The measured diffusivity is higher than the literature value in only one case. Sources of error include a low signal-noise ratio in the Raman spectra, a lack of precise temperature control due to laser heating of the solvent, and the lack of spatially variable data. The last error is necessitated by the fact that a change in the position of the capillary sample in the xy-plane would also change the z-position of the Raman spectra acquisition location resulting in the Raman spectra at different locations not being comparable. Consequently the data in (x,t) coordinate space is restricted to a single x data point and variable in t.

5.3.2 PDMS

The diffusivity of CO_2 in three PDMS derivatives of 550, 1250, and 2000 molecular weight was compared using the Raman spectroscopy-based method. These solvents also vary in density and viscosity as can be seen in Table 5.2.

Table 5.2: Physical Properties of PDMS Solvents

Molecular Weight (g/mol)	Viscosity (cSt)	Density (kg/m^3)
550	3	898
1250	10	935
2000	20	950

For the case of gas diffusion in liquids, the diffusivity is inversely proportional to solvent viscosity (i.e. CO_2 should diffuse faster with decreasing PDMS molecular weight).[87,88] An example of the evolution of the

CO_2 Raman peak in PDMS 550 during the course of one experiment can be seen below in Figure 5.3.

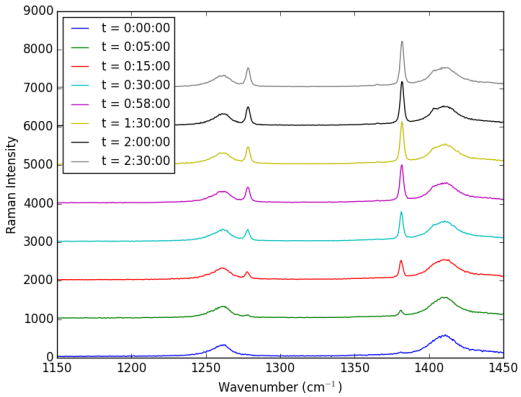

Figure 5.3: Raman Spectra of dissolved CO_2 in PDMS 550 as a function of time (P=20.4 bar,2.0 mm away from gas-liquid interface)

The area underneath the 1382 cm^{-1} peak was determined through numerical integration and Equation 5.3 was applied to fit a diffusivity as can be seen in Figure 5.4.

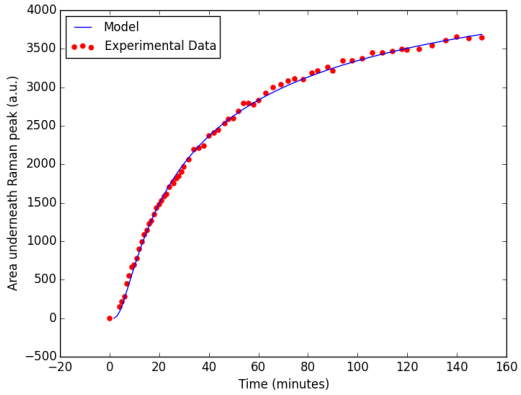

Figure 5.4: Raman Peak Area as a function of time for PDMS 550 (D calculated to be 1.41*10^{-9} m^2/s) (P=20.4 bar,2.0 mm away from gas-liquid interface)

These experiments were conducted twice for PDMS 550, and three times each for PDMS 1250 and 2000. Summaries of these experiments can be seen below.

Table 5.3: Measured Diffusivity for PDMS 550

Appendix #	P (bar)	$L_{solvent}$ (cm)	x (mm)	D (m^2/s)	Fitted A_0
10	20.1	0.77	1.6	$7.94 * 10^{-10}$	6322
11	20.4	1.32	2.0	$1.41 * 10^{-9}$	5321
				Average: $1.10 * 10^{-9}$	

Table 5.4: Measured Diffusivity for PDMS 1250

Appendix #	P (bar)	$L_{solvent}$ (cm)	x (mm)	D (m^2/s)	Fitted A_0
12	20.1	1.26	1.8	$1.45 * 10^{-9}$	4673
13	20.5	1.26	1.9	$1.41 * 10^{-9}$	6344
14	20.4	1.26	1.9	$1.72 * 10^{-9}$	5526
				Average: $1.53 * 10^{-9}$	

Table 5.5: Measured Diffusivity for PDMS 2000

Appendix #	P (bar)	$L_{solvent}$ (cm)	x (mm)	D (m^2/s)	Fitted A_0
15	20.2	1.41	1.9	$6.83 * 10^{-10}$	1661
16	21.0	1.41	1.9	$1.83 * 10^{-9}$	5943
17	20.7	1.41	1.9	$1.27 * 10^{-9}$	4650
				Average: $1.26 * 10^{-9}$	

These results do not indicate a strong trend in the diffusivity with change in the molecular weight of the PDMS. The diffusion coefficient for CO_2 in PDMS has previously been experimentally measured as $2.6 * 10^{-9}$ m^2/s at 35 °C.[89] Therefore, it is not surprising that the diffusivity measurements in this study are lower since they were conducted at 10-15 °C cooler temperatures.

5.4 Conclusions

A microliter-scale method for the determination of the diffusivity of CO_2 in a non-reacting solvent was developed based on the time dependent measurement of the Raman spectra of dissolved CO_2 and the application of a 1-D Fickian diffusion model. The diffusion coefficient was determined at room temperature (20-25 °C) and pressures of 20-40 bar for CO_2 in water

and in three PDMS derivatives of molecular weights of 550, 1250, and 2000 g/mol. The diffusion coefficient of CO_2 in water was determined to be 6.06 * 10^{-10} m^2/s as the average of nine experiments. This value is 34% of the literature value and indicates a systematic underestimation of the diffusion rate.

This error may be caused by a number of things. One limitation is a lack of precise temperature control due to sample heating by the laser. This error would cause an overestimation of the diffusivity due to the elevated temperature of the sample. Since our measurements in water are systematically underestimating the diffusivity, this error due to sample heating by the laser can be regarded as not significant. Another limitation is that the spectra acquisition process itself takes approximately 10 seconds to complete, so the time for each data point is taken as the time of the start of the acquisition and is thus approximate. Also the quality of the fit of the analytical model to the data is very sensitive to the signal-noise ratio in the Raman spectra, which is evident by comparing the fit for the cases of water with the cases of PDMS. Lastly, as the concentration of CO_2 increases in the solvent, the density of the solvent changes causing movement of the gas-liquid interface in the capillary, the position of which in relation to the acquisition position must be known precisely to fit the Fickian model. For the case of the three PDMS derivatives with viscosities varying from 3 to 20 cSt, no significant trend in the CO_2-PDMS diffusion coefficient was observed. Further improvements to the method's accuracy must be made in order for the value of this approach to extend beyond evaluation of trends in solvents with diffusivities that vary by greater than one order of magnitude.

6 Estimation of the Heat of Absorption for Amine-CO_2 Systems using Raman Spectroscopy

6.1 Introduction

Chapter 4 addressed the microfluidic measurement of CO_2 absorption capacity of PCC chemical solvents. Image analysis of segmented flow was demonstrated to be a highly effective method of determining the rich CO_2 loadings of amine solutions. The issue of the amine's desorption capacity and consequently the working capacity of the amine was not included in that study. The current chapter aims to address the regeneration of CO_2-loaded amine solutions by developing a method utilizing Raman spectroscopy and fused capillary cells analogous to the thermodynamic measurements conducted in Chapter 3. A method for the measurement of the heat of absorption which is the sum of the heat of physical CO_2 dissolution and the heat of CO_2-amine reaction is developed. The most reliable means for obtaining the heat of absorption utilize gas-liquid calorimetry which is expensive and done infrequently in the literature, as well as impractical to conduct with μL-scale solvent volumes. The heat of absorption is frequently obtained from vapor-liquid equilibrium (VLE) experiments using the Gibbs-Helmholtz equation.[90–92] The Gibbs-Helmholtz equation in its most general form can be seen in Equation 6.1.[90]

$$\Delta H_{0,i} = R\left(\frac{\partial ln(f_i)}{\partial \frac{1}{T}}\right)_{\sigma,x_0} - \frac{V_{0,i}}{T}\left(\frac{\partial P}{\partial \frac{1}{T}}\right)_{\sigma,x_0} \tag{6.1}$$

The second term on the right-hand side of the equation is typically small and negligible relative to the first term.[90] The simplified Gibbs-Helmholtz equation as it is most commonly implemented can be seen in Equation 6.2 after assuming ideal conditions.

$$\Delta H_{0,i} = R(\frac{\partial ln(P_i)}{\partial \frac{1}{T}})_{\sigma,x_0} \tag{6.2}$$

The present work is focused on the design of a fused silica capillary-based μL-scale VLE experiment and the development and application of a thermodynamic model similar to the Gibbs-Helmholtz equation to obtain the heat of absorption from Raman spectra of the capillary system. Two alkanolamines, MEA and methyldiethanolamine (MDEA) (Figure 6.1), are used as validation cases. The tertiary structure of MDEA means that MDEA undergoes reaction with CO_2 to form bicarbonate and does not undergo the carbamate reaction pathway due to the lack of a N-H bond. Consequently, previous literature measurements demonstrate that CO_2 absorption in MDEA is less exothermic than CO_2 absorption in primary alkanolamines, such as MEA.

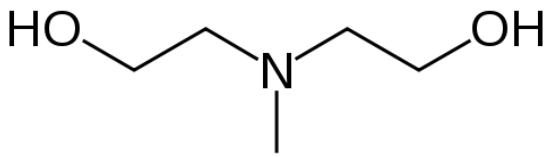

Figure 6.1: Chemical structure of MDEA

6.2 Methods

The methodology for estimating the heat of absorption for an amine solvent involves the heating of a pre-CO_2-loaded solvent sample contained in a closed silica capillary containing the solvent and a head space. A Raman spectrum of the head space is acquired at each temperature. As the temperature increases,

the amine-CO_2 reaction equilibrium is shifted so that CO_2 is released from the solvent into the head space resulting in an increase in the concentration of gaseous CO_2 and an increase in the intensity of the Raman peaks of gaseous CO_2. The area underneath the main CO_2 peak at 1388 cm^{-1} can be related to the CO_2 pressure in the head space through this relation: $A = \sigma * \frac{P}{RT}$ with σ being the Raman cross-section of the CO_2 molecule as mentioned in Chapters 3 and 5. This equation is substituted into Equation 6.2 to obtain Equation 6.3.

$$\frac{\partial ln(A_{CO_2}T)}{\partial \frac{1}{T}} = \frac{\Delta H_{abs}}{R} \tag{6.3}$$

The heat of absorption can be obtained from Equation 6.3 by plotting $ln(A_{CO_2}T)$ against $1/T$ and fitting a linear regression to obtain the slope.

The amine solution is first pre-loaded with CO_2 either through a direct line from the gas cylinder or by mixing the amine solution with CO_2 in the microfluidic reactor as described in Chapter 4. Partial CO_2 loadings (less than the equilibrium amount) of the microfluidic reactor's effluent can be achieved by varying the initial gas plug and liquid slug lengths so that the gas plugs completely dissolve into the amine solution before the amine solution reaches CO_2 saturation. Image analysis, as described in Chapter 4, enables the CO_2 loading of the amine solution effluent to be precisely measured prior to Raman experiments. This is important due to the dependence of the heat of absorption on CO_2 loading.[93] A section of the silica capillary (approximately 2.5-2.7 cm in length) used in Chapters 3 and 5 is cut and the polyimide protective coating is completely removed from the capillary surface. The capillary is then partially filled from one open end with the CO_2-loaded amine solution via capillary action. The opposite open end is flame-sealed with an acetylene torch and the solvent is forced into the closed end through centrifugation. The other end is then also flame-sealed with an acetylene torch leaving a completely closed

silica capillary containing a single liquid slug and head space 1.5-2.3 cm(1.2-1.8 μL liquid volume) and 0.4-1 cm in length respectively.

Raman spectroscopy was carried out on a Horiba LabRamHR spectrometer using a Spectra Physics 532 nm Nd:Yag laser with an operating power of 0.2 W as the excitation source. Spectra were taken using an Olympus 50xLWD objective and were recorded as the average of ten three-second exposures. The capillary sample was heated using the same Linkam Cap500 heating stage used in Chapter 3. The sample was allowed to equilibrate at each temperature for a minimum of 2 hours prior to Raman spectra acquisition. In order to assure that the intensities of Raman spectrum at each temperature be comparable, a z-scan focusing procedure was performed at each temperature and the highest-intensity Raman spectrum at each temperature was selected to be included in the analysis. The area underneath the Raman peak of CO_2 at 1388 cm^{-1} is obtained through numerical integration after baseline-substraction of the background intensity.

6.3 Results and Discussion

6.3.1 MEA

Three samples of MEA were prepared using the microfluidic reactor to prepare them with CO_2 loadings of 0.15, 0.3, and 0.18 mol CO_2/mol MEA. A fourth sample of MEA was prepared by bubbling CO_2 directly from a gas cylinder until saturation (i.e. $\approx$ 0.5 mol CO_2/mol MEA). The temperature-dependent Raman spectra of the head space in the 0.18 mol CO_2/mol MEA sample can be seen in Figure 6.2.

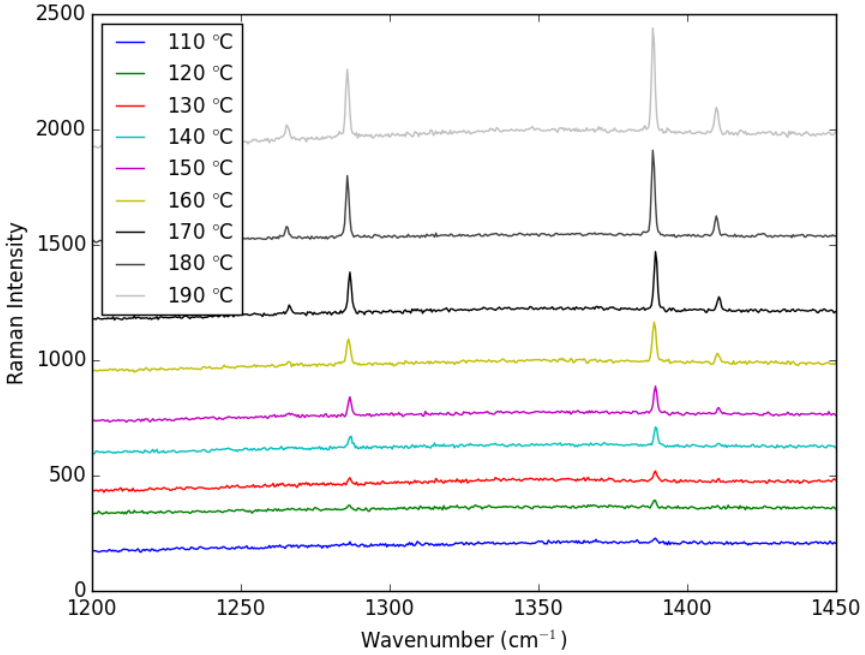

Figure 6.2: Raman Spectra of gas-phase CO_2 in headspace of capillary containing 30 wt% MEA

The largest peak of the CO_2 Fermi dyad at 1388 cm^- was not detected at all below a stage temperature of 110 °C in this experiment. This peak grows in intensity as the temperature is increased from 110 °C to 190 °C. The heat of absorption was calculated based on the linear regression shown in Figure 6.3. The heat of absorption for this particular sample was determined to be -62 kJ/mol with a 95% confidence interval of +/- 4 kJ/mol.

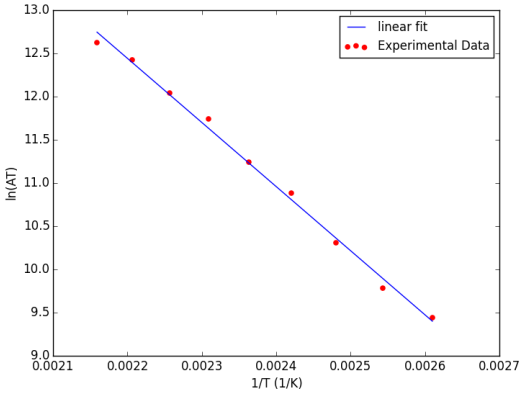

Figure 6.3: Data and linear regression used to determine heat of absorption for 30 wt% MEA (linear regression: y= -7422x + 28.77 with r^2 = 0.995)

Figures analogous to 6.2 and 6.3 for the other MEA samples can be found in Appendix 10. A summary of the results obtained for each MEA sample can be found in Table 6.1.

Table 6.1: Calculated Heat of CO_2 Absorption for 30wt% MEA. Errors are reported as 95% confidence intervals

CO_2 loading (mol CO_2/mol MEA)	-ΔH_{abs}(error) (kJ/mol)
0.15	62 (35)
0.18	62 (4)
0.30	35 (5)
Saturated	28 (2)

As the CO_2 loading of the sample increases, the calculated ΔH_{abs} decreases which is consistent with the trends evident in literature calorimetric data and previous estimates based on the Gibbs-Helmholtz equation.[93] However, the calculated values of -ΔH_{abs} in Table 6.1 are approximately 20 kJ/mol less than the average reported literature values.[93,94] This underestimation of the heat of absorption is due to several limitations of both the Gibbs-Helmholtz method, as well as its application to the closed capillary system that is discussed below.

6.3.2 MDEA

As mentioned above, MDEA, is a tertiary amine that absorbs CO_2 through bicarbonate formation as it is unable to undergo carbamate formation. Svensson et.al. used calorimetry to measure the absorption enthalpy of 27 wt% MDEA at 0-0.4 mol CO_2/mol MDEA and 35 °C to 65 °C.[95] They report an average value of -61.4 kJ/mol for ΔH_{abs}.[95] In order to make a comparison with this value, a 27 wt% MDEA solution was prepared and partially loaded to 0.21 mol CO_2/mol MDEA in the microfluidic reactor. The change in the Raman spectrum of the head space with increasing temperature is illustrated in Figure 6.4.

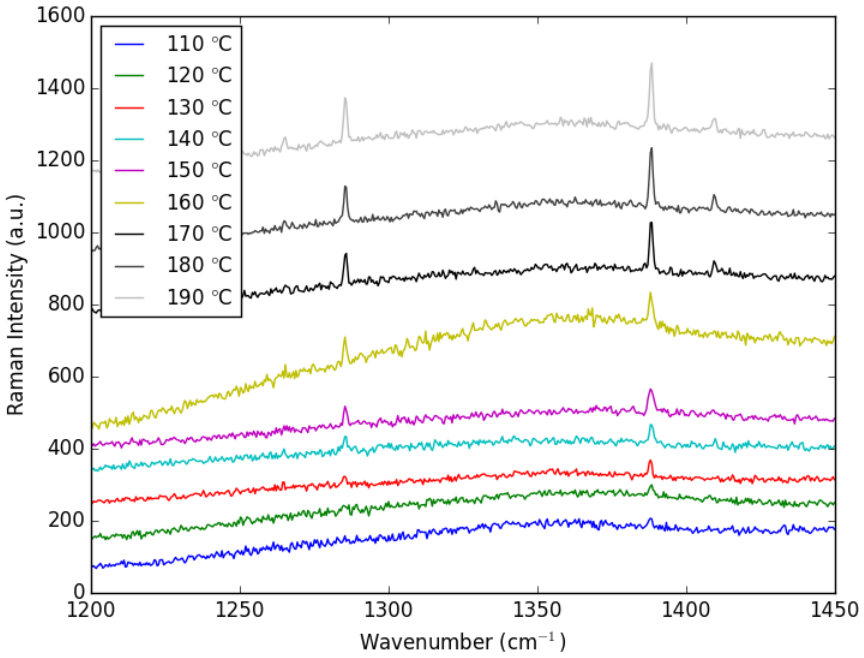

Figure 6.4: Raman Spectra of gas-phase CO_2 in headspace of capillary containing 27 wt% MDEA

The heat of absorption was determined to be -39 +/- 5 kJ/mol from the linear regression shown in Figure 6.5.

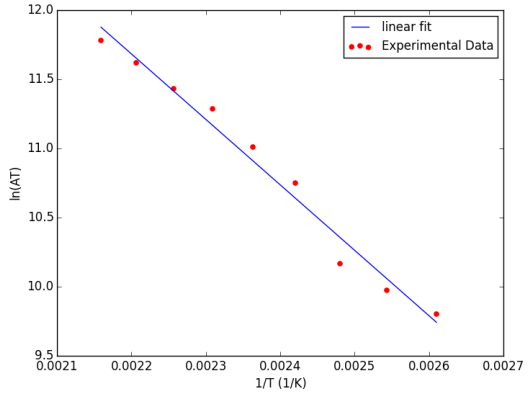

Figure 6.5: Data and linear regression used to determine heat of absorption for 27 wt% MDEA (linear regression: y= -4735x + 22.10 with $r^2 = 0.979$)

The calculated heat of absorption for MDEA differs from the literature values by a similar amount and in the same direction as the values for MEA. This indicates that there is a systematic offset between literature calorimetric data and the heat of absorption as calculated in the present work. The calculated $-\Delta H_{abs}$ value for MDEA is lower than MEA by the approximate amount that is observed in previous literature. Consequently, differences between solvents with heats of absorption differing on the order of > 10 kJ/mol can be observed rapidly and with $<2\mu$L of solvent with the method presented here. The precise reason for the discrepancy between the literature heats of absorption for MEA and MDEA and those calculated in the present work is unidentified. However, several potential sources of error are discussed below.

6.3.3 Method Limitations

There are a number of limitations that contribute to the inaccuracy of the present Gibbs-Helmholtz Raman spectroscopic method. The traditional application of the Gibbs-Helmholtz equation to VLE experiments are known to be imprecise, particularly with regards to temperature effects.[90,94] There

are also several critical differences in the experimental design of traditional VLE experiments and the closed capillary experimental apparatus used in the present work that may influence the appropriate modeling of the data and were neglected in the above analysis. First, the Gibbs-Helmholtz equation is almost exclusively applied to VLE data collected under isobaric conditions. The measurements for 30 wt% in Aronu et. al. were all conducted at atmospheric pressure.[93] This is quite different than the closed capillary system which can be considered isochoric (at least with regards to the total capillary volume as the liquid undergoes thermal expansion with increasing temperature) instead of isobaric. One interpretation of this is that the heats of absorption above should be considered internal energies of absorption rather than enthalpies of absorption. The Gibbs-Helmholtz equation is also rarely applied to VLE data at temperatures above 120 °C as it is done in the present work. Furthermore, the standard form of the Gibbs-Helmholtz equation relies on the assumption of ideality implying low pressures and also a constant loading of CO_2 in the solvent. Depending on the geometries of the head space and liquid slug in the capillary, these assumptions may not be valid. A Raman area-CO_2 pressure calibration experiment was performed with an empty capillary and the swagelok apparatus used in Chapters 3 and 5. The calibration estimates that the pressure inside the headspace during the MEA and MDEA Gibbs-Helmholtz experiments reaches up to 24 and 10 bar respectively. This suggests that the activity coefficients for CO_2 and the amine are not unity under all conditions of the experiment as is assumed in the derivation of the Gibbs-Helmholtz equation. Another effect that was neglected from the present analysis is that at high temperatures, the amine solution slugs undergo a significant

volumetric expansion in the capillary due to a decrease in the solution density such that the head space is reduced in length to <1 mm.

6.4 Conclusions

A μL-scale method for determining the heat of CO_2 absorption of a PCC chemical solvent was discussed. The method relies on Raman spectroscopic measurements of a heated closed capillary cell partially filled with pre-CO_2-loaded amine solution. The commonly-used Gibbs-Helmholtz equation was applied by relating the area underneath the gas-phase CO_2 Raman peak to the gas-phase CO_2 pressure. The heat of absorption was calculated for samples of MEA varying in CO_2 loading from 0.15 mol CO_2/mol MEA up to CO_2 saturation. The heat of absorption was found to decrease (i.e. the absorption becomes less exothermic) with increasing CO_2 loading of the amine solution. This conclusion is consistent with previous literature. Additionally the heat of absorption was found to be ≈20 kJ/mol lower (less negative) for MDEA than for MEA. This conclusion is also consistent with previous literature and suggests potential for distinguishing between PCC solvents whose CO_2 absorption mechanisms differ. However, the simplified Gibbs-Helmholtz model was shown to be inadequate in reflecting the thermodynamics of the closed capillary experiment and inadequate in matching the accuracy of calorimetric measurements. It is determined that either some modifications of the Gibbs-Helmholtz model must be applied to reflect the thermodynamic conditions of the capillary system, or the capillary experiment itself must be redesigned in order to improve the accuracy of the calculation of the heat of absorption from Raman spectra.

7 Conclusions

The characterization of CO_2 capture materials as substitutes for MEA in a PCC process and for Selexol® in a pre-combustion CO_2 capture process involves the measurement of many CO_2 capture characteristics. Additionally there are a wide range of candidate materials that have been proposed. The high throughput screening of their CO_2 capture efficacy is dependent on the development of low-volume rapid experimental measurement techniques for obtaining thermodynamic and kinetic information. The work presented in this thesis illustrates the effectiveness of microfluidic techniques in acquiring a variety of thermodynamic and kinetic data pertaining to both PCC and pre-combustion CO_2 capture. Chapters 2, 4, and 6 investigated amine-based PCC systems and identified critical material selection criteria such as SO_2-resistance as well as oxidative stability, amine molecular structure and molecular weight, as well as the reaction mechanism's impact on the heat of absorption. Chapters 3 and 5 illustrate the application of quantitative analysis methods to Raman spectra to enable the measurement of variables pertaining to pre-combustion CO_2 capture with μL-scale volumes.

Chapter 2 investigated the O_2 and SO_2 tolerance of a primary amine-functionalized polymeric solid sorbent using a packed-bed reactor. The working capacity of the sorbent was measured through the course of several adsorption/desorption cycles carried out via a thermal swing between 50 and 127 °C with continuous exposure to a simulated flue gas stream containing 12% CO_2, 4% O_2, 84% N_2 and with a 12.5% CO_2, 4% O_2, 431ppm SO_2, balance N_2 gas stream. The working capacity of the sorbent remained constant over 17 cycles in the presence of O_2 and absence of SO_2. However, the addition of 431ppm SO_2 resulted in rapid and irreversible poisoning of the amine sorbent which exhibited an SO_2 adsorption of 0.98 mol / kg

sorbent and a decrease in CO_2 capacity of 1.31 mol / kg sorbent after only 9 temperature swing cycles. The SO_2-poisoned resin was not thermally regenerable, although treating the poisoned resin with NaOH resulted in partial regeneration of the amine sorbent. While SO_2 removal is conducted at many PC power plants, many do not remove SO_2 and SO_2 levels can be as high as 2000 ppm. Any level of SO_2 in the CO_2 capture gas stream will, gradually over time irreversibly and competitively react with primary amines resulting in a loss of CO_2 capture capacity.

Chapter 4 continued the discussion of PCC material characterization with a focus on liquid amine-based solvents. Specifically the aqueous potassium salts of glycine, taurine, proline, and lysine were investigated and compared with MEA. The CO_2 absorption capacity and rate were measured through image analysis of segmented gas-plug/liquid-slug flow in a microfluidic channel. The potassium salt of lysine exhibited the highest rich CO_2 loading, $> 50\%$ higher than MEA. This increased CO_2 capacity was explained by the additional primary amine functional group present in the side-chain of lysine. The accuracy of the microfluidic experiments in predicting trends in absorption capacity in a CSTR was confirmed through independent CSTR measurements of the equilibrium CO_2 absorption capacity of potassium lysinate and MEA solutions. The performance of MEA and LYS was evaluated by comparing solutions of each prepared with the same molar concentration, and also with the same weight fraction of water (70 wt%). The higher stoichiometry of the CO_2-LYS reaction was offset by the lower molecular weight of MEA. This is reflected by the fact that the 0.5M LYS solution absorbed more CO_2 than the 0.5M MEA solution, but the 30 wt% MEA solution absorbed more CO_2 than the 1.48 M LYS solution.

Chapter 6 concluded the discussion of PCC material characterization with a description of a μL-scale method for determining the heat of CO_2 absorption for an amine solvent using Raman spectroscopy and the Gibbs-Helmholtz equation. The method was applied to a 30 wt% MEA solution and a 27 wt% MDEA solution. The heat of absorption of the 30 wt% MEA solution was measured for a range of CO_2 loading from 0.15 mol CO_2/mol MEA up to CO_2 saturation and the heat of absorption was found to decrease (become less negative) with increasing CO_2 loading, which confirmed the trend in the literature calorimetric data. The heat of absorption for the 27 wt% MDEA solution was calculated to be ≈20 kJ/mol lower (less negative) than the 30 wt% MEA solution, which is consistent with previous MDEA calorimetric measurements. A systematic underestimation of the heat of absorption by ≈ 20-30% was observed for both amines and indicates further inquiry into the appropriate thermodynamic modeling of the closed capillary system should be conducted.

Chapters 3 and 5 addressed the μL-scale characterization of pre-combustion CO_2 capture solvents. Chapter 3 compared the CO_2 solubility, CO_2/H_2 selectivity, at room temperature up to 100 °C and the heat of CO_2 solution of a hydrophobic PDMS-PEGDME hybrid solvent with Selexol® using Raman spectroscopy and a silica capillary-stainless steel pressure assembly. The CO_2 solubility of the PDMS-PEGDME hybrid was found to be significantly greater than that of PDMS and comparable with that of Selexol® at room temperature. The solubility of H_2 in the hybrid was found to be quite low and also similar in magnitude to the solubility of H_2 in Selexol®. A van't Hoff expression was used to calculate the heat of CO_2 solution for the hybrid using the dimensionless Henry's Law constant at varying temperature. The heat of CO_2 solution was found to be -8.14 +/-

0.91 kJ/mol for the hybrid solvent which is lower than reported values for Selexol® indicating that CO_2 absorption with the PDMS-PEGDME hybrid is less exothermic than CO_2 absorption in Selexol®. Chapter 5 introduced a method to measure the diffusivity of CO_2 in a physical solvent using Raman spectroscopy and the same silica capillary-stainless steel pressure assembly used in Chapter 3. This method was used to measure the diffusion coefficient of CO_2 in water and in three PDMS derivatives of 550, 1250, and 2000 g/mol molecular weight. Multiple measurements of the diffusivity of CO_2 in water revealed a systematic underestimation of the reported literature value. It was determined that while the diffusivity of CO_2 in a physical solvent can be determined by this method within an order of magnitude, the method lacked the precision to distinguish between diffusion in the three PDMS derivatives, which did not exhibit any apparent trend in CO_2 diffusivity.

Throughout the course of this thesis work a wide variety of both PCC and pre-combustion CO_2 capture material parameters were investigated using primarily μL-scale measurement techniques. CO_2 capture materials that were investigated include: a primary amine-functionalized solid sorbent, aqueous amino acid salt solutions, alkanolamines including MEA and MDEA, Selexol®, PDMS, and a hydrophobic PDMS-PEGDME hybrid physical solvent. There is considerable room for further research to address several of the unresolved issues of this work as well as opportunity for advancing the microfluidic techniques demonstrated in this work. The microfluidic measurement of the thermodynamics of the reaction between CO_2 and an amine solvent remains a challenge that was not adequately addressed in Chapter 6 and is certainly an important task for evaluating PCC materials for a specific set of process conditions. The development of heating capability for the y-junction microfluidic reactor used in Chapter 4 is

an alternative, and potentially easier, approach to determining the working capacity of an amine solution at a combination of absorption and desorption temperatures. A couple microchip heating strategies include the use of a water or oil-bath as well as surface heating elements such as indium tin-oxide (ITO) heaters.[71] Further research should also focus on the closer integration between the CO_2 capture process design and the experimental characterization of the CO_2 capture material with the goal of the direct measurement of the solvent or sorbent parameters necessary to predict the overall efficiency of the CO_2 capture process designed using the specific material in question. Micro-scale approaches to the measurement of CO_2 capture thermodynamics and kinetics are well-suited to the high throughput screening of the extensive material design space that is continuing to grow.

References

[1] IGCC. Climate change 2013: The physical science basis, fith assessment report of the IGCC. Technical report, Intergovernmental panel on climate change, 2013.

[2] U.S. Environmental Protection Agency. Draft inventory of U.S. greenhouse gas emissions and sinks: 1990-2014. Technical report, U.S. EPA, 2016.

[3] International Energy Agency. Key world energy statistics. Technical report, IEA, 2015.

[4] Timothy Fout. DOE/NETL's carbon capture R&D program for existing coal-fired power plants. Technical report, DOE/NETL, 2009.

[5] Edward S. Rubin, Hari Mantripragada, Aaron Marks, Peter Versteeg, and John Kitchin. The outlook for improved carbon capture technology. *Progress in Energy and Combustion Science*, 38(5):630 – 671, 2012.

[6] Xiaochun Xu, Chunshan Song, Ronald Wincek, John M. Andresen, Bruce G. Miller, and Alan W. Scaroni. Separation of CO_2 from power plant flue gas using a novel CO_2 "molecular basket" adsorbent. *Fuel Chemistry Division Preprints*, 48:162–163, 2003.

[7] Gary T. Rochelle. Amine scrubbing for CO_2 capture. *Science*, 325(5948):1652–1654, 2009.

[8] Nichola McCann, Duong Phan, Xiaoguang Wang, William Conway, Robert Burns, Moetaz Attalla, Graeme Puxty, and Marcel Maeder. Kinetics and mechanism of carbamate formation from CO_2(aq), carbonate species, and monoethanolamine in aqueous solution. *The Journal of Physical Chemistry A*, 113(17):5022–5029, 2009. PMID: 19338322.

[9] Michael Caplow. Kinetics of carbamate formation and breakdown. *Journal of the American Chemical Society*, 90(24):6795–6803, 1968.

[10] P.V. Danckwerts. The reaction of CO_2 with ethanolamines. *Chemical Engineering Science*, 34(4):443 – 446, 1979.

[11] John E. Crooks and J. Paul Donnellan. Kinetics and mechanism of the reaction between carbon dioxide and amines in aqueous solution. *J. Chem. Soc., Perkin Trans. 2*, pages 331–333, 1989.

[12] James T. Yeh, , Henry W. Pennline, and Kevin P. Resnik. Study of CO_2 absorption and desorption in a packed column. *Energy & Fuels*, 15(2):274–278, 2001.

[13] Alexander K. Voice and Gary T. Rochelle. Oxidation of amines at absorber conditions for CO_2 capture from flue gas. *Energy Procedia*, 4:171 – 178, 2011. 10th International Conference on Greenhouse Gas Control Technologies.

[14] Itoro J. Uyanga and Raphael O. Idem. Studies of SO_2- and O_2-induced degradation of aqueous MEA during CO_2 capture from power plant flue gas streams. *Industrial & Engineering Chemistry Research*, 46(8):2558–2566, 2007.

[15] Victor Darde, Kaj Thomsen, Willy J.M. van Well, and Erling H. Stenby. Chilled ammonia process for CO_2 capture. *International Journal of Greenhouse Gas Control*, 4(2):131 – 136, 2010. The Ninth International Conference on Greenhouse Gas Control Technologies.

[16] Gary Rochelle, Eric Chen, Stephanie Freeman, David Van Wagener, Qing Xu, and Alexander Voice. Aqueous piperazine as the new standard for CO_2 capture technology. *Chemical Engineering Journal*, 171(3):725 – 733, 2011. Special Section: Symposium on Post-Combustion Carbon Dioxide Capture.

[17] J.Tim Cullinane and Gary T. Rochelle. Carbon dioxide absorption with aqueous potassium carbonate promoted by piperazine. *Chemical Engineering Science*, 59(17):3619 – 3630, 2004.

[18] Ujjal K. Ghosh, Sandra E. Kentish, and Geoff W. Stevens. Absorption of carbon dioxide into aqueous potassium carbonate promoted by boric acid. *Energy Procedia*, 1(1):1075 – 1081, 2009. Greenhouse Gas Control Technologies 9Proceedings of the 9th International Conference on

Greenhouse Gas Control Technologies (GHGT-9), 16-20 November 2008, Washington DC, {USA}.

[19] Hanna Knuutila, Hallvard F. Svendsen, and Olav Juliussen. Kinetics of carbonate based CO_2 capture systems. *Energy Procedia*, 1(1):1011 – 1018, 2009. Greenhouse Gas Control Technologies 9Proceedings of the 9th International Conference on Greenhouse Gas Control Technologies (GHGT-9), 16-20 November 2008, Washington DC, {USA}.

[20] Tobias Jockenhoevel, Ruediger Schneider, and Helmut Rode. Development of an economic post-combustion carbon capture process. *Energy Procedia*, 1(1):1043 – 1050, 2009. Greenhouse Gas Control Technologies 9Proceedings of the 9th International Conference on Greenhouse Gas Control Technologies (GHGT-9), 16-20 November 2008, Washington DC, {USA}.

[21] J. van Holst, G.F. Versteeg, D.W.F. Brilman, and J.A. Hogendoorn. Kinetic study of CO_2 with various amino acid salts in aqueous solution. *Chemical Engineering Science*, 64(1):59 – 68, 2009.

[22] Subham Paul and Kaj Thomsen. Kinetics of absorption of carbon dioxide into aqueous potassium salt of proline. *International Journal of Greenhouse Gas Control*, 8:169 – 179, 2012.

[23] Eva Sanchez Fernandez, Katarzyna Heffernan, Leen V. van der Ham, Marco J. G. Linders, Emma Eggink, Frank N. H. Schrama, D. W. F. Brilman, Earl L. V. Goetheer, and Thijs J. H. Vlugt. Conceptual design of a novel CO_2 capture process based on precipitating amino acid solvents. *Industrial & Engineering Chemistry Research*, 52(34):12223–12235, 2013.

[24] Yamini Sudha Sistla and Ashok Khanna. Carbon dioxide absorption studies using amine-functionalized ionic liquids. *Journal of Industrial and Engineering Chemistry*, 20(4):2497 – 2509, 2014.

[25] Arunkumar Samanta, An Zhao, George K. H. Shimizu, Partha Sarkar, and Rajender Gupta. Post-combustion CO_2 capture using solid sorbents: A review. *Industrial & Engineering Chemistry Research*, 51(4):1438–1463, 2012.

[26] Patricia Luis, Tom Van Gerven, and Bart Van der Bruggen. Recent developments in membrane-based technologies for CO_2 capture. *Progress in Energy and Combustion Science*, 38(3):419 – 448, 2012.

[27] C. Descamps, C. Bouallou, and M. Kanniche. Efficiency of an integrated gasification combined cycle (IGGC) power plant including CO_2 removal. *Energy*, 33(6):874 – 881, 2008. {PRES} 2006. 9th Conference of Process Integration, Modelling and Optimisation for Energy Saving and Pollution Reduction - {PRES} 2006PRES 2006.

[28] Keith Burnard and Sankar Bhattacharya. Power generation from coal: Ongoing developments and outlook. Technical report, International Energy Agency, 2011.

[29] Eliane Blomen, Chris Hendriks, and Filip Neele. Capture technologies: Improvements and promising developments. *Energy Procedia*, 1(1):1505 – 1512, 2009. Greenhouse Gas Control Technologies 9Proceedings of the 9th International Conference on Greenhouse Gas Control Technologies (GHGT-9), 16-20 November 2008, Washington DC, {USA}.

[30] Abass A. Olajire. CO_2 capture and separation technologies for end-of-pipe applications - a review. *Energy*, 35(6):2610 – 2628, 2010.

7th International Conference on Sustainable Energy Technologies7th International Conference on Sustainable Energy Technologies.

[31] Matthew B. Miller, David R. Luebke, and Robert M. Enick. CO_2-philic oligomers as novel solvents for CO_2 absorption. *Energy & Fuels*, 24(11):6214–6219, 2010.

[32] Cesar Cadena, Jennifer L. Anthony, Jindal K. Shah, Timothy I. Morrow, Joan F. Brennecke, and Edward J. Maginn. Why is CO_2 so soluble in imidazolium-based ionic liquids? *Journal of the American Chemical Society*, 126(16):5300–5308, 2004. PMID: 15099115.

[33] M. Hasib ur Rahman, M. Siaj, and F. Larachi. Ionic liquids for CO_2 capture-development and progress. *Chemical Engineering and Processing: Process Intensification*, 49(4):313 – 322, 2010.

[34] James C. Fisher, Ranjani V. Siriwardane, and Robert W. Stevens. Zeolite-based process for CO_2 capture from high-pressure, moderate-temperature gas streams. *Industrial & Engineering Chemistry Research*, 50(24):13962–13968, 2011.

[35] Trevor C. Drage, James M. Blackman, Cova Pevida, and Colin E. Snape. Evaluation of activated carbon adsorbents for CO_2 capture in gasification. *Energy & Fuels*, 23(5):2790–2796, 2009.

[36] Wen Li, Sunho Choi, Jeffery H. Drese, Marc Hornbostel, Gopala Krishnan, Peter M. Eisenberger, and Christopher W. Jones. Steam-stripping for regeneration of supported amine-based CO_2 adsorbents. *ChemSusChem*, 3(8):899–903, 2010.

[37] T.C. Drage, K.M. Smith, A. Arenillas, and C.E. Snape. Developing strategies for the regeneration of polyethylenimine based CO_2 adsorbents.

Energy Procedia, 1(1):875 – 880, 2009. Greenhouse Gas Control Technologies 9Proceedings of the 9th International Conference on Greenhouse Gas Control Technologies (GHGT-9), 16-20 November 2008, Washington DC, {USA}.

[38] W. Richard Alesi and John R. Kitchin. Evaluation of a primary amine-functionalized ion-exchange resin for CO_2 capture. *Industrial & Engineering Chemistry Research*, 51(19):6907–6915, 2012.

[39] ML Gray, Y Soong, KJ Champagne, HW Pennline, J Baltrus, RW Jr, R Khatri, and SSC Chuang. Capture of carbon dioxide by solid amine sorbents. *International journal of environmental technology and management*, 4(1-2):82–88, 2004.

[40] W. Richard Alesi, McMahan Gray, and John R. Kitchin. CO_2 adsorption on supported molecular amidine systems on activated carbon. *ChemSusChem*, 3(8):948–956, 2010.

[41] Robert S. Franchi, Peter J. E. Harlick, and Abdelhamid Sayari. Applications of pore-expanded mesoporous silica. 2. development of a high-capacity, water-tolerant adsorbent for CO_2. *Industrial & Engineering Chemistry Research*, 44(21):8007–8013, 2005.

[42] Youssef Belmabkhout and Abdelhamid Sayari. Isothermal versus non-isothermal adsorption-desorption cycling of triamine-grafted pore-expanded mcm-41 mesoporous silica for CO_2 capture from flue gas. *Energy & Fuels*, 24(9):5273–5280, 2010.

[43] Rajesh A. Khatri, Steven S. C. Chuang, Yee Soong, and McMahan Gray. Thermal and chemical stability of regenerable solid amine sorbent for CO_2 capture. *Energy & Fuels*, 20(4):1514–1520, 2006.

[44] Alexander P. Hallenbeck and John R. Kitchin. Effects of O_2 and SO_2 on the capture capacity of a primary-amine based polymeric CO_2 sorbent. *Industrial & Engineering Chemistry Research*, 52(31):10788–10794, 2013.

[45] Richard Alesi. *Amine Based Sorbents: Developing a Quantitative Framework for Understanding CO_2 capture.* PhD thesis, Carnegie Mellon University, 2012.

[46] Stephen Brunauer, P. H. Emmett, and Edward Teller. Adsorption of gases in multimolecular layers. *Journal of the American Chemical Society*, 60(2):309–319, 1938.

[47] Elliott P. Barrett, Leslie G. Joyner, and Paul P. Halenda. The determination of pore volume and area distributions in porous substances. i. computations from nitrogen isotherms. *Journal of the American Chemical Society*, 73(1):373–380, 1951.

[48] Alicia J. Reynolds, T. Vincent Verheyen, Samuel B. Adeloju, Erik Meuleman, and Paul Feron. Towards commercial scale postcombustion capture of CO_2 with monoethanolamine solvent: Key considerations for solvent management and environmental impacts. *Environmental Science & Technology*, 46(7):3643–3654, 2012. PMID: 22324566.

[49] Sharon Sjostrom and Holly Krutka. Evaluation of solid sorbents as a retrofit technology for CO_2 capture. *Fuel*, 89(6):1298 – 1306, 2010. Advanced Fossil Energy Utilization.

[50] Stephen A. Bedell. Oxidative degradation mechanisms for amines in flue gas capture. *Energy Procedia*, 1(1):771 – 778, 2009. Greenhouse Gas Control Technologies 9Proceedings of the 9th International Conference on

Greenhouse Gas Control Technologies (GHGT-9), 16-20 November 2008, Washington DC, USA.

[51] Abdelhamid Sayari and Youssef Belmabkhout. Stabilization of amine-containing CO_2 adsorbents: Dramatic effect of water vapor. *Journal of the American Chemical Society*, 132(18):6312–6314, 2010. PMID: 20405941.

[52] Anamaria Padurean, Calin-Cristian Cormos, and Paul-Serban Agachi. Pre-combustion carbon dioxide capture by gas-liquid absorption for integrated gasification combined cycle power plants. *International Journal of Greenhouse Gas Control*, 7:1 – 11, 2012.

[53] R. M. Enick, P. Koronaios, C. Stevenson, S. Warman, B. Morsi, H. Nulwala, and D. Luebke. Hydrophobic polymeric solvents for the selective absorption of CO_2 from warm gas streams that also contain H_2 and H_2O. *Energy & Fuels*, 27(11):6913–6920, 2013.

[54] H. Nulwala and D. Luebke. High performance hydrophobic solvent, carbon dioxide capture, April 30 2015. US Patent App. 14/525,011.

[55] Anita S. Lee. *A Multi-Scale Approach to Understanding CO_2-Solvent Systems for the Development of CO_2 Capture Technologies*. PhD thesis, Carnegie Mellon University, 2013.

[56] Andrew J. Berger, Yang Wang, David M. Sammeth, Irving Itzkan, Katrin Kneipp, and Michael S. Feld. Aqueous dissolved gas measurements using near-infrared raman spectroscopy. *Appl. Spectrosc.*, 49(8):1164–1169, Aug 1995.

[57] Amr Henni, Paitoon Tontiwachwuthikul, and Amit Chakma. Solubilities of carbon dioxide in polyethylene glycol ethers. *The Canadian Journal of Chemical Engineering*, 83(2):358–361, 2005.

[58] Aravind V. Rayer, Amr Henni, and Paitoon Tontiwachwuthikul. High pressure physical solubility of carbon dioxide (CO_2) in mixed polyethylene glycol dimethyl ethers (genosorb 1753). *The Canadian Journal of Chemical Engineering*, 90(3):576–583, 2012.

[59] Jin ah Lim, Dong Hyun Kim, Yeoil Yoon, Soon Kwan Jeong, Ki Tae Park, and Sung Chan Nam. Absorption of CO_2 into aqueous potassium salt solutions of l-alanine and l-proline. *Energy & Fuels*, 26(6):3910–3918, 2012.

[60] Robert J. Hook. An investigation of some sterically hindered amines as potential carbon dioxide scrubbing compounds. *Industrial & Engineering Chemistry Research*, 36(5):1779–1790, 1997.

[61] A.F. Portugal, P.W.J. Derks, G.F. Versteeg, F.D. Magalhães, and A. Mendes. Characterization of potassium glycinate for carbon dioxide absorption purposes. *Chemical Engineering Science*, 62(23):6534 – 6547, 2007.

[62] Quanzhen Huang, Saloni Bhatnagar, Joseph E. Remias, John P. Selegue, and Kunlei Liu. Thermal degradation of amino acid salts in CO_2 capture. *International Journal of Greenhouse Gas Control*, 19:243 – 250, 2013.

[63] P. S. Kumar, J. A. Hogendoorn, G. F. Versteeg, and P. H. M. Feron. Kinetics of the reaction of CO_2 with aqueous potassium salt of taurine and glycine. *AIChE Journal*, 49(1):203–213, 2003.

[64] Hanna Knuutila, Ugochukwu E. Aronu, Hanne M. Kvamsdal, and Actor Chikukwa. Post combustion CO_2 capture with an amino acid salt. *Energy Procedia*, 4:1550 – 1557, 2011. 10th International Conference on Greenhouse Gas Control Technologies.

[65] Ho-Jun Song, Sangwon Park, Hyuntae Kim, Ankur Gaur, Jin-Won Park, and Seung-Jong Lee. Carbon dioxide absorption characteristics of aqueous amino acid salt solutions. *International Journal of Greenhouse Gas Control*, 11:64 – 72, 2012.

[66] Benedict Mai Lerche. *CO_2 Capture from Flue gas using Amino acid salt solutions*. PhD thesis, Technical University of Denmark, August 2012.

[67] Milad Abolhasani, Mayank Singh, Eugenia Kumacheva, and Axel Gunther. Automated microfluidic platform for studies of carbon dioxide dissolution and solubility in physical solvents. *Lab Chip*, 12:1611–1618, 2012.

[68] Ruopeng Sun and Thomas Cubaud. Dissolution of carbon dioxide bubbles and microfluidic multiphase flows. *Lab Chip*, 11:2924–2928, 2011.

[69] A. Gunther M. Abolhasani, E. Kumacheva. Model-predictive strategy for exploration of carbon dioxide dissolution and mass transfer.

[70] Stephanie G. R. Lefortier, Peter J. Hamersma, Andre Bardow, and Michiel T. Kreutzer. Rapid microfluidic screening of CO_2 solubility and diffusion in pure and mixed solvents. *Lab Chip*, 12:3387–3391, 2012.

[71] Wei Li, Kun Liu, Ryan Simms, Jesse Greener, Dinesh Jagadeesan, Sascha Pinto, Axel Günther, and Eugenia Kumacheva. Microfluidic study of fast gas-liquid reactions. *Journal of the American Chemical Society*, 134(6):3127–3132, 2012. PMID: 22176612.

[72] Chunying Zhu, Chunfang Li, Xiqun Gao, Youguang Ma, and Dongzhi Liu. Taylor flow and mass transfer of CO_2 chemical absorption into MEA aqueous solutions in a t-junction microchannel. *International Journal of Heat and Mass Transfer*, 73:492 – 499, 2014.

[73] Lu Yang, Jing Tan, Kai Wang, and Guangsheng Luo. Mass transfer characteristics of bubbly flow in microchannels. *Chemical Engineering Science*, 109:306 – 314, 2014.

[74] Dan Voicu, Milad Abolhasani, Rachelle Choueiri, Gabriella Lestari, Caroline Seiler, Gabriel Menard, Jesse Greener, Axel Guenther, Douglas W. Stephan, and Eugenia Kumacheva. Microfluidic studies of CO_2 sequestration by frustrated lewis pairs. *Journal of the American Chemical Society*, 136(10):3875–3880, 2014. PMID: 24555752.

[75] Chunbo YE, Guangwen CHEN, and Quan YUAN. Process characteristics of CO_2 absorption by aqueous monoethanolamine in a microchannel reactor. *Chinese Journal of Chemical Engineering*, 20(1):111 – 119, 2012.

[76] Alexander P. Hallenbeck, Adefemi Egbebi, Kevin P. Resnik, David Hopkinson, Shelley L. Anna, and John R. Kitchin. Comparative microfluidic screening of amino acid salt solutions for post-combustion CO_2 capture. *International Journal of Greenhouse Gas Control*, 43:189 – 197, 2015.

[77] Ethanolamines. Technical report, DOW Chemical Company, 2003.

[78] P.A. Gamunu L. Samarakoon, Niels H. Andersen, Cristina Perinu, and Klaus-J. Jens. Equilibria of MEA, DEA and AMP with bicarbonate and carbamate: A raman study. *Energy Procedia*, 37:2002 – 2010, 2013. GHGT-11 Proceedings of the 11th International Conference on Greenhouse Gas Control Technologies, 18-22 November 2012, Kyoto, Japan.

[79] *Infrared and Raman Characteristic Group Frequencies: Tables and Charts*. John Wiley & Sons Ltd., 2001.

[80] Nanping Wen and Murray H. Brooker. Ammonium carbonate, ammonium bicarbonate, and ammonium carbamate equilibria: A Raman study. *The Journal of Physical Chemistry*, 99(1):359–368, 1995.

[81] John D. Frantz. Raman spectra of potassium carbonate and bicarbonate aqueous fluids at elevated temperatures and pressures: Comparison with theoretical simulations. *Chemical Geology*, 152(3-4):211 – 225, 1998.

[82] Mohammad R. Riazi. A new method for experimental measurement of diffusion coefficients in reservoir fluids. *Journal of Petroleum Science and Engineering*, 14(3-4):235 – 250, 1996.

[83] Ho Teng and Akihiro Yamasaki. Solubility of liquid CO_2 in synthetic sea water at temperatures from 278 K to 293 K and pressures from 6.44 Mpa to 29.49 Mpa, and densities of the corresponding aqueous solutions. *Journal of Chemical & Engineering Data*, 43(1):2–5, 1998.

[84] Andrew Sell, Hossein Fadaei, Myeongsub Kim, and David Sinton. Measurement of CO_2 diffusivity for carbon sequestration: A microfluidic approach for reservoir-specific analysis. *Environmental Science & Technology*, 47(1):71–78, 2013. PMID: 23092110.

[85] Hossein Fadaei, Brent Scarff, and David Sinton. Rapid microfluidics-based measurement of CO_2 diffusivity in bitumen. *Energy & Fuels*, 25(10):4829–4835, 2011.

[86] *Mass-Transfer Operations*. McGraw-Hill Book Company, 1980.

[87] Christina Cruickshank Miller. The stokes-einstein law for diffusion in solution. *Proceedings of the Royal Society of London A: Mathematical, Physical and Engineering Sciences*, 106(740):724–749, 1924.

[88] C. R. Wilke and Pin Chang. Correlation of diffusion coefficients in dilute solutions. *AIChE Journal*, 1(2):264–270, 1955.

[89] S. G. Charati and S. A. Stern. Diffusion of gases in silicone polymers: Molecular dynamics simulations. *Macromolecules*, 31(16):5529–5535, 1998.

[90] Paul M. Mathias and John P. O'Connell. The Gibbs-Helmholtz equation and the thermodynamic consistency of chemical absorption data. *Industrial & Engineering Chemistry Research*, 51(13):5090–5097, 2012.

[91] Randal L. Perry, John C. Telotte, and John P. O'Connell. Solution thermodynamics for "reactive" components. *Fluid Phase Equilibria*, 5(3):245 – 277, 1981.

[92] Thomas W. Copeman and Fred P. Stein. On the derivation and application of solution thermodynamics for reactive components. *Fluid Phase Equilibria*, 9(2):149 – 165, 1982.

[93] Ugochukwu E. Aronu, Shahla Gondal, Erik T. Hessen, Tore Haug-Warberg, Ardi Hartono, Karl A. Hoff, and Hallvard F. Svendsen. Solubility of CO_2 in 15, 30, 45 and 60 mass% MEA from 40 to 120 °C and model representation using the extended UNIQUAC framework. *Chemical Engineering Science*, 66(24):6393 – 6406, 2011. Novel Gas Conversion Symposium- Lyon 2010, C1-C4 Catalytic Processes for the Production of Chemicals and Fuels.

[94] Inna Kim, Karl Anders Hoff, and Thor Mejdell. Heat of absorption of CO_2 with aqueous solutions of MEA: New experimental data. *Energy Procedia*, 63:1446 – 1455, 2014. 12th International Conference on Greenhouse Gas Control Technologies, GHGT-12.

[95] Helena Svensson, Christian Hulteberg, and Hans T. Karlsson. Heat of absorption of CO_2 in aqueous solutions of n-methyldiethanolamine and piperazine. *International Journal of Greenhouse Gas Control*, 17:89 – 98, 2013.

8 Appendix A: Supporting information for Chapter 2

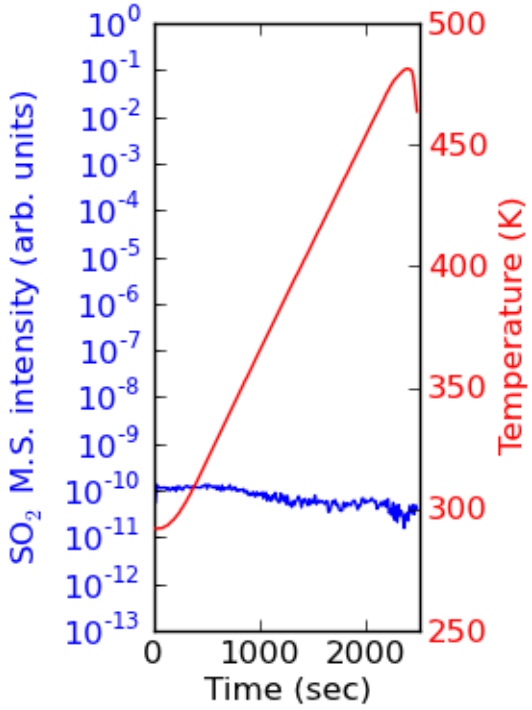

Figure 8.1: Temperature swing desorption of SO_2-poisoned resin under inert N_2 gas stream

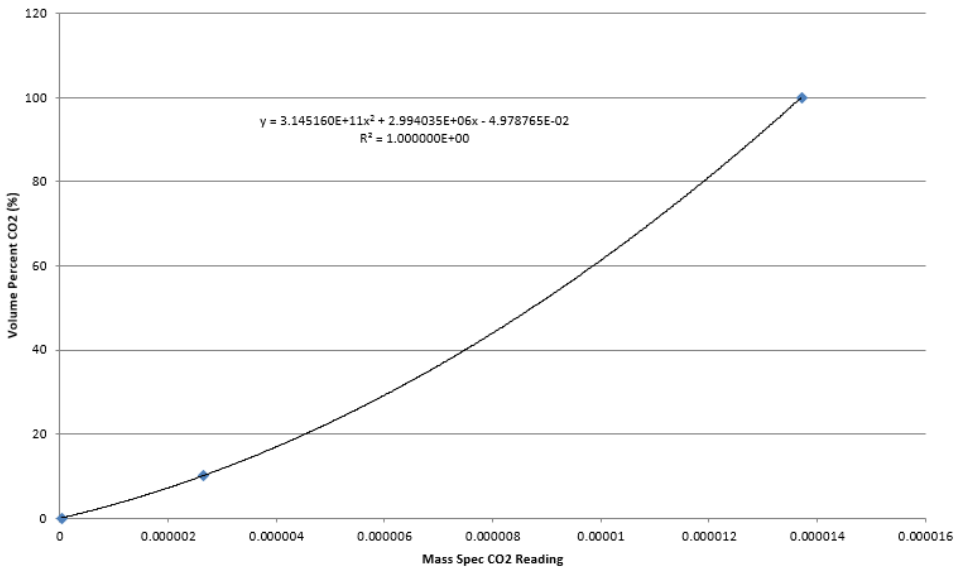

Figure 8.2: Mass spectrometer CO_2 concentration calibration example

9 Appendix B: Supporting information for Chapter 5

9.1 1

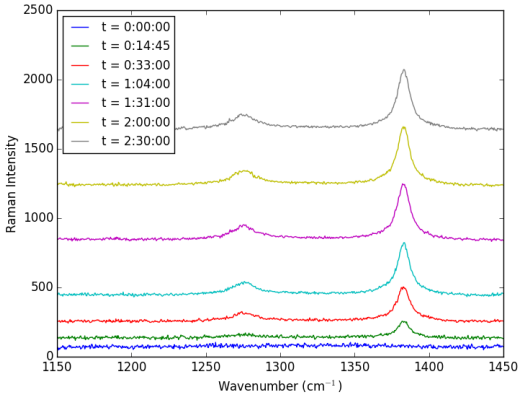

Figure 9.1: Raman Spectra of dissolved CO_2 in water as a function of time (P=30.2 bar,1.36 mm away from gas-liquid interface)

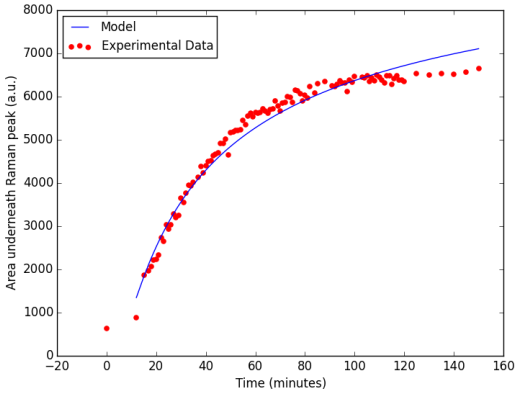

Figure 9.2: Raman Peak Area as a function of time for water (D calculated to be 5.49*10^{-10} m^2/s) (P=30.2 bar,1.36 mm away from gas-liquid interface)

9.2 2

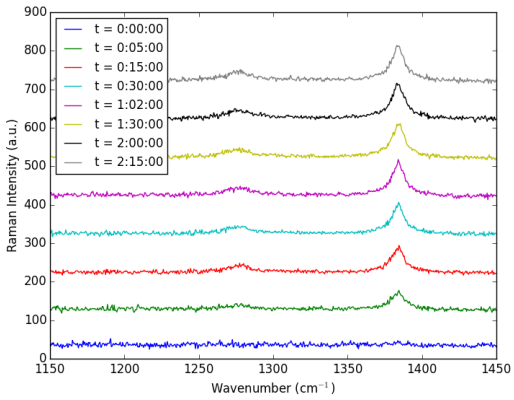

Figure 9.3: Raman Spectra of dissolved CO_2 in water as a function of time (P=20.82 bar,1.07 mm away from gas-liquid interface)

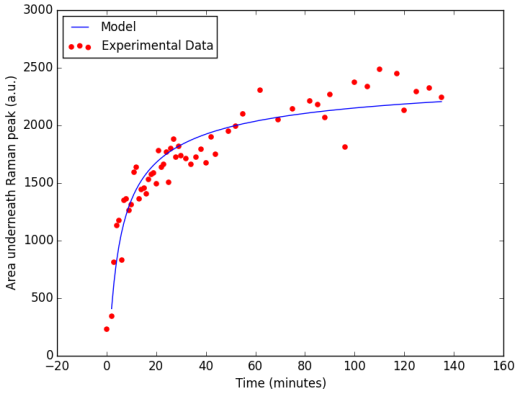

Figure 9.4: Raman Peak Area as a function of time for water (D calculated to be 2.42*10^{-9} m^2/s) (P=20.82 bar,1.07 mm away from gas-liquid interface)

9.3 3

See Chapter 5

9.4 4

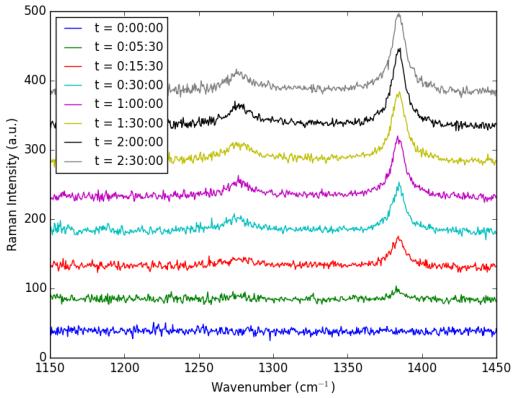

Figure 9.5: Raman Spectra of dissolved CO_2 in water as a function of time (P=20.55 bar,0.77 mm away from gas-liquid interface)

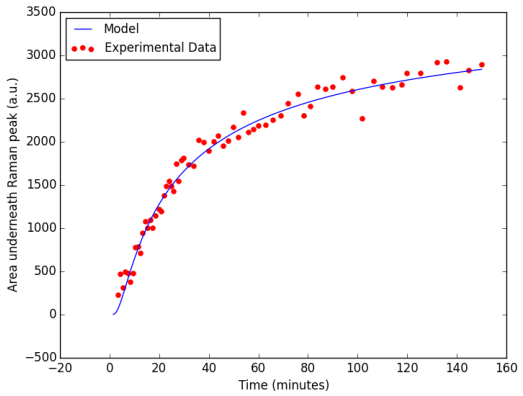

Figure 9.6: Raman Peak Area as a function of time for water (D calculated to be 2.54*10^{-10} m^2/s) (P=20.55 bar,0.77 mm away from gas-liquid interface)

9.5 5

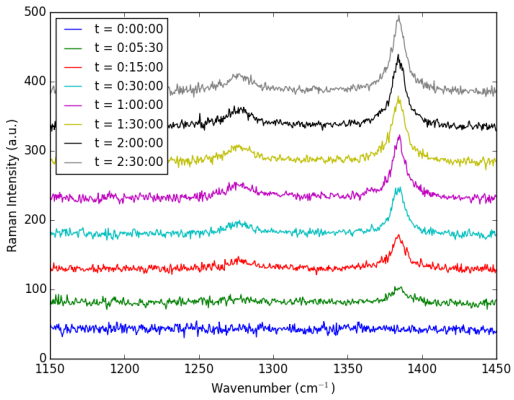

Figure 9.7: Raman Spectra of dissolved CO_2 in water as a function of time (P=19.79 bar,0.55 mm away from gas-liquid interface)

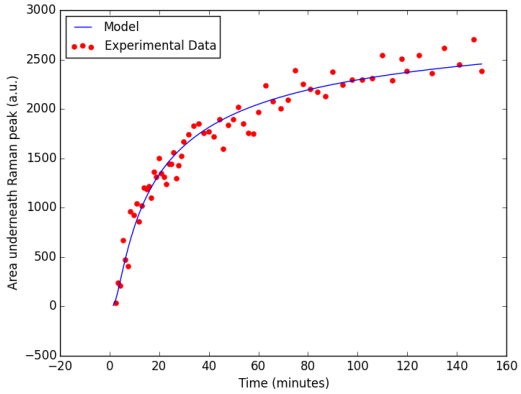

Figure 9.8: Raman Peak Area as a function of time for water (D calculated to be $1.92*10^{-10}$ m^2/s) (P=19.79 bar,0.55 mm away from gas-liquid interface)

9.6 6

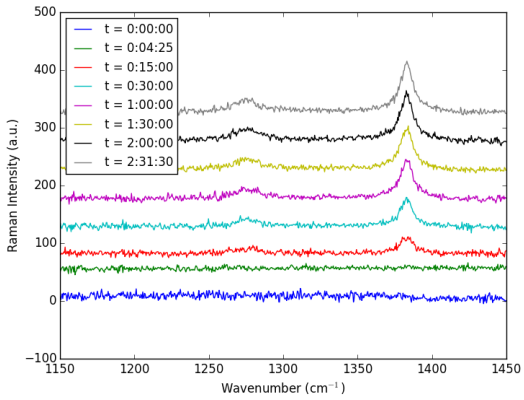

Figure 9.9: Raman Spectra of dissolved CO_2 in water as a function of time (P=20.27 bar,0.94 mm away from gas-liquid interface)

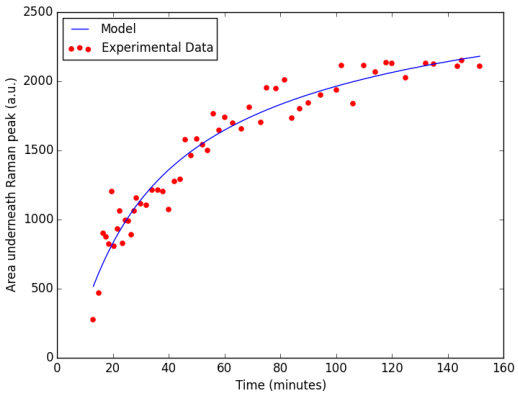

Figure 9.10: Raman Peak Area as a function of time for water (D calculated to be 2.89*10^{-10} m^2/s) (P=20.27 bar,0.94 mm away from gas-liquid interface)

9.7 7

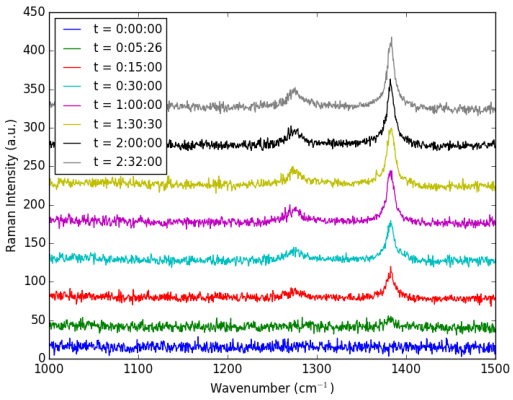

Figure 9.11: Raman Spectra of dissolved CO_2 in water as a function of time (P=20.34 bar,0.85 mm away from gas-liquid interface)

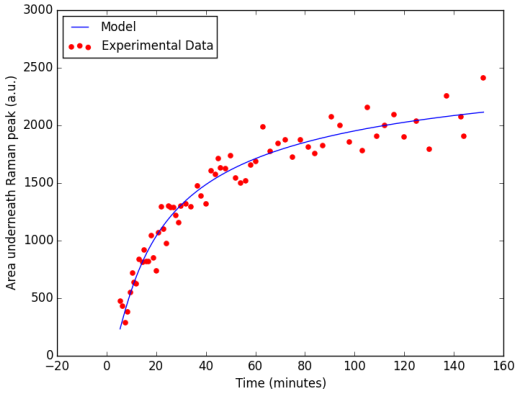

Figure 9.12: Raman Peak Area as a function of time for water (D calculated to be $3.66*10^{-10}$ m^2/s) (P=20.34 bar,0.85 mm away from gas-liquid interface)

9.8 8

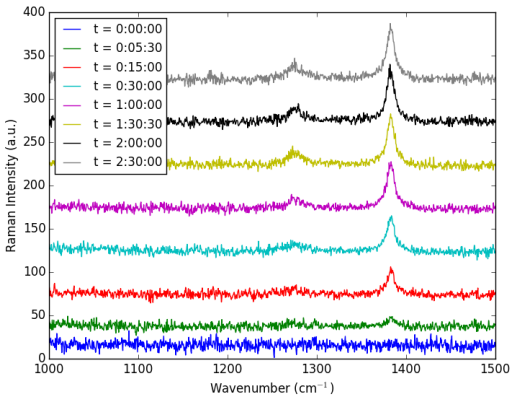

Figure 9.13: Raman Spectra of dissolved CO_2 in water as a function of time (P=20.06 bar,0.79 mm away from gas-liquid interface)

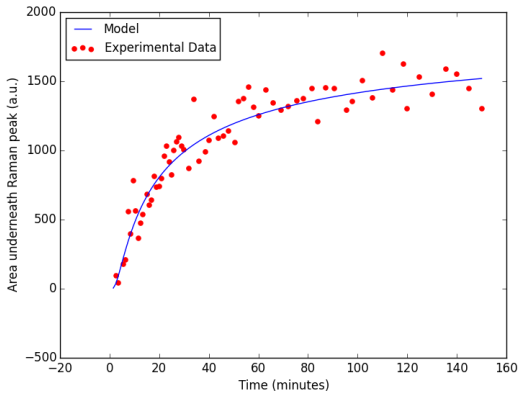

Figure 9.14: Raman Peak Area as a function of time for water (D calculated to be $3.72*10^{-10}$ m^2/s) (P=20.06 bar,0.79 mm away from gas-liquid interface)

9.9 9

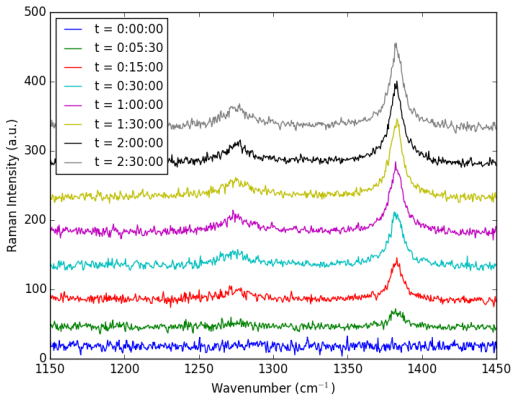

Figure 9.15: Raman Spectra of dissolved CO_2 in water as a function of time (P=20.34 bar,0.70 mm away from gas-liquid interface)

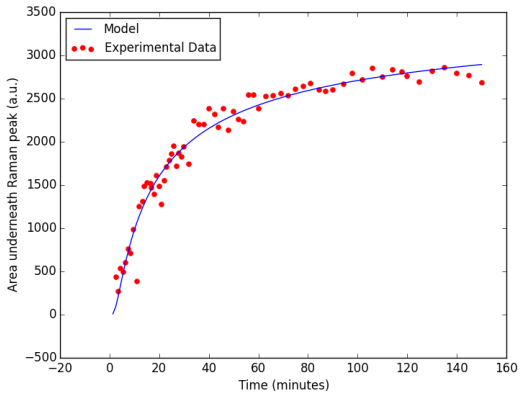

Figure 9.16: Raman Peak Area as a function of time for water (D calculated to be $3.24*10^{-10}$ m^2/s) (P=20.34 bar,0.70 mm away from gas-liquid interface)

9.10 10

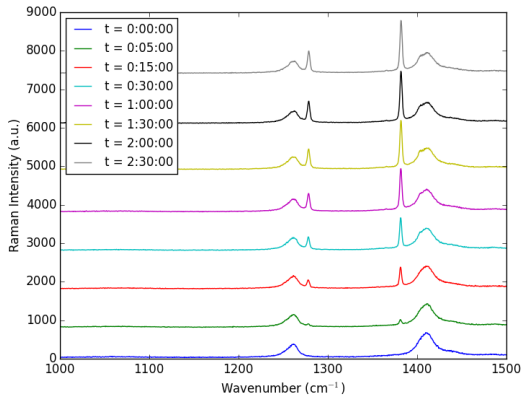

Figure 9.17: Raman Spectra of dissolved CO_2 in PDMS 550 as a function of time (P=20.1 bar,1.6 mm away from gas-liquid interface)

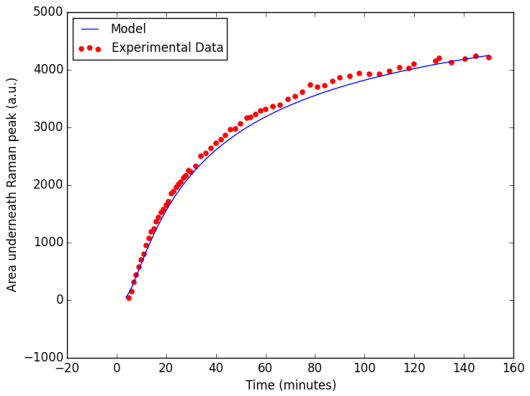

Figure 9.18: Raman Peak Area as a function of time for PDMS 550 (D calculated to be 7.94*10^{-10} m^2/s) (P=20.1 bar,1.60 mm away from gas-liquid interface)

9.11 11

See Chapter 5

9.12 12

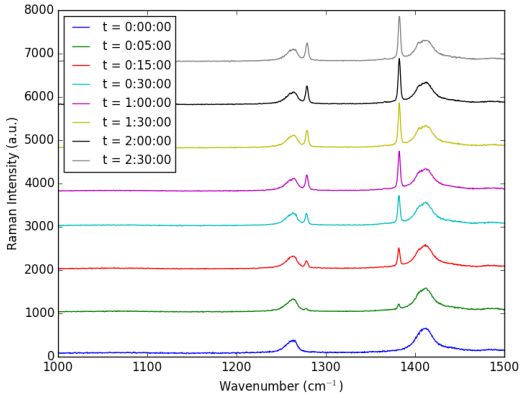

Figure 9.19: Raman Spectra of dissolved CO_2 in PDMS 1250 as a function of time (P=20.1 bar,1.8 mm away from gas-liquid interface)

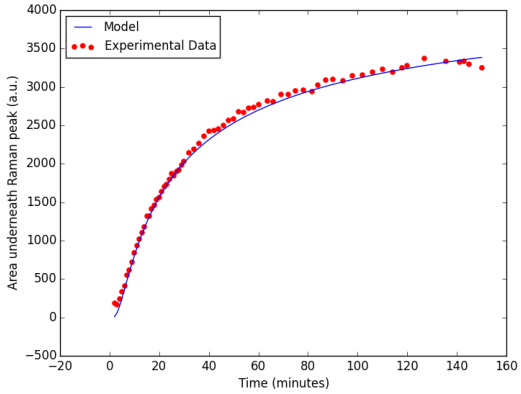

Figure 9.20: Raman Peak Area as a function of time for PDMS 1250 (D calculated to be 1.45*10^{-9} m^2/s) (P=20.1 bar,1.80 mm away from gas-liquid interface)

9.13 13

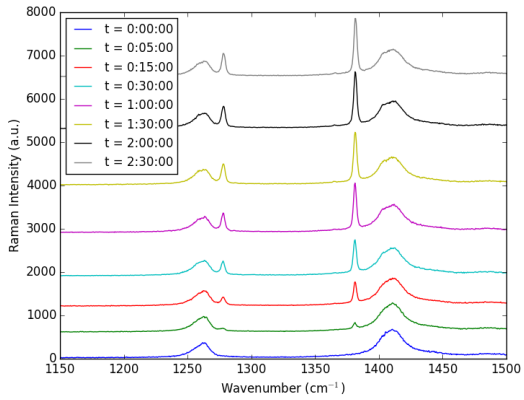

Figure 9.21: Raman Spectra of dissolved CO_2 in PDMS 1250 as a function of time (P=20.5 bar,1.9 mm away from gas-liquid interface)

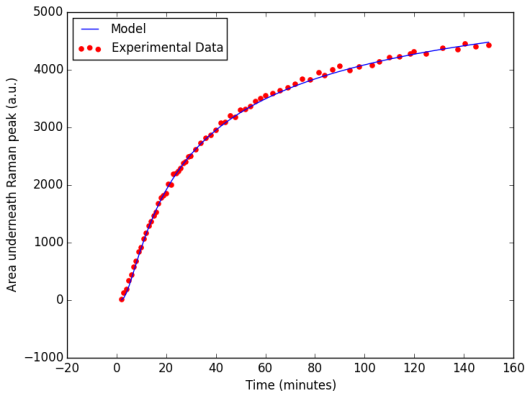

Figure 9.22: Raman Peak Area as a function of time for PDMS 1250 (D calculated to be 1.41*10^{-9} m^2/s) (P=20.5 bar,1.90 mm away from gas-liquid interface)

9.14 14

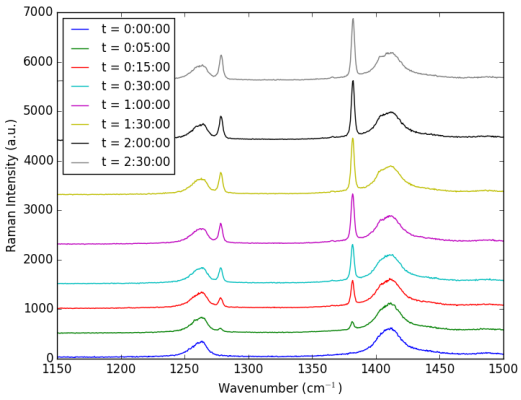

Figure 9.23: Raman Spectra of dissolved CO_2 in PDMS 1250 as a function of time (P=20.4 bar,1.9 mm away from gas-liquid interface)

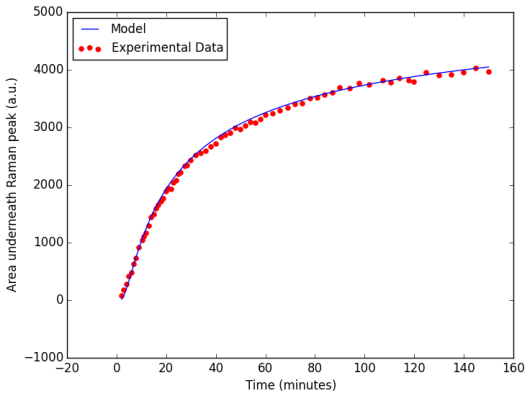

Figure 9.24: Raman Peak Area as a function of time for PDMS 1250 (D calculated to be 1.72*10^{-9} m^2/s) (P=20.4 bar,1.9 mm away from gas-liquid interface)

9.15 15

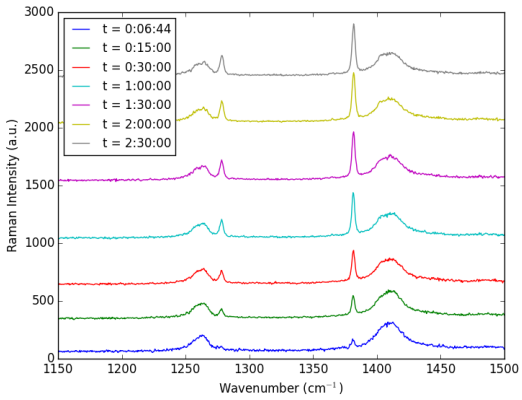

Figure 9.25: Raman Spectra of dissolved CO_2 in PDMS 2000 as a function of time (P=20.2 bar,1.9 mm away from gas-liquid interface)

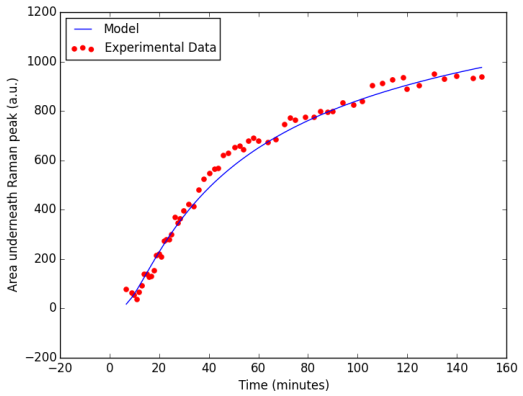

Figure 9.26: Raman Peak Area as a function of time for PDMS 2000 (D calculated to be $6.83*10^{-10}$ m^2/s) (P=20.2 bar,1.9 mm away from gas-liquid interface)

9.16 16

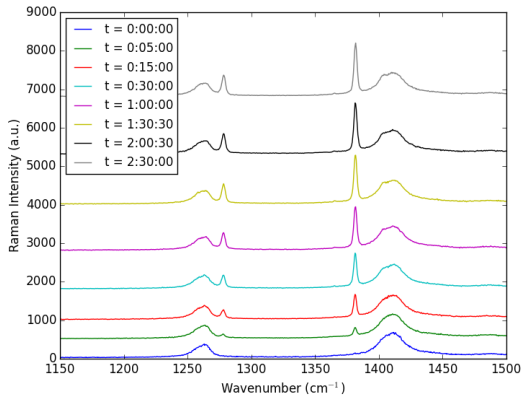

Figure 9.27: Raman Spectra of dissolved CO_2 in PDMS 2000 as a function of time (P=21.0 bar,1.9 mm away from gas-liquid interface)

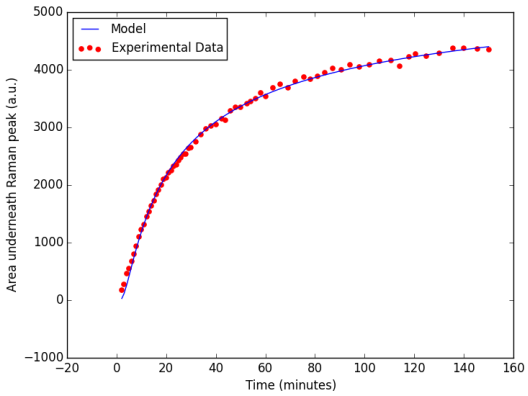

Figure 9.28: Raman Peak Area as a function of time for PDMS 2000 (D calculated to be 1.83*10^{-9} m^2/s) (P=21.0 bar,1.9 mm away from gas-liquid interface)

9.17 17

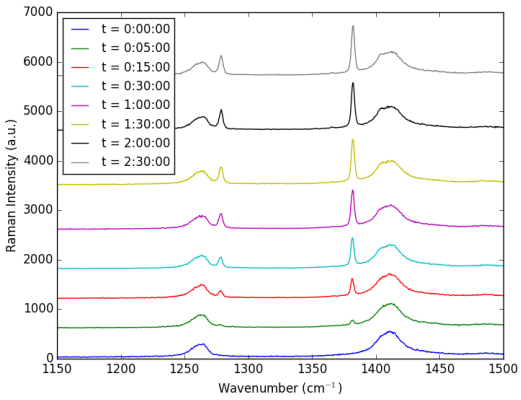

Figure 9.29: Raman Spectra of dissolved CO_2 in PDMS 2000 as a function of time (P=20.7 bar,1.9 mm away from gas-liquid interface)

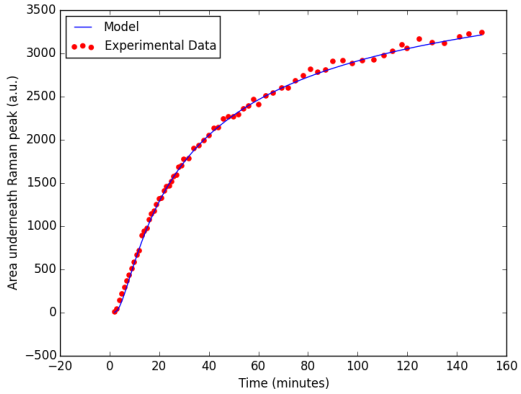

Figure 9.30: Raman Peak Area as a function of time for PDMS 2000 (D calculated to be 1.27*10^{-9} m^2/s) (P=20.7 bar,1.9 mm away from gas-liquid interface)

10 Appendix C: Supporting information for Chapter 6

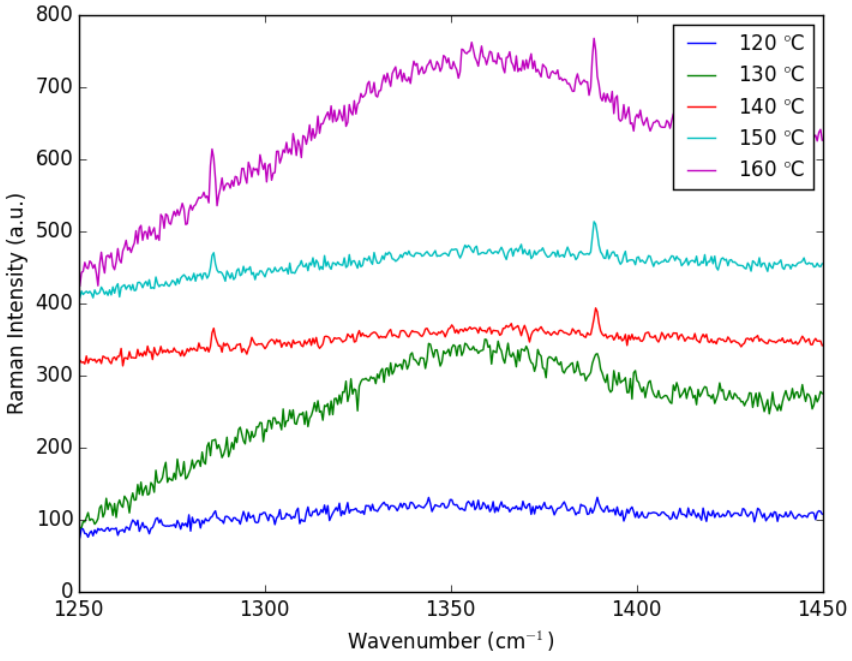

Figure 10.1: Raman Spectra of gas-phase CO_2 in headspace of capillary containing 30 wt% MEA at a loading of 0.15 mol CO_2/mol MEA

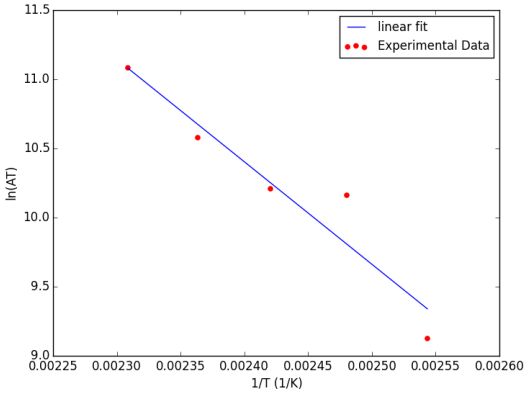

Figure 10.2: Data and linear regression used to determine heat of absorption for 30 wt% MEA with a loading of 0.15 mol CO_2/mol MEA (linear regression: y= -7414x + 28.20 with r^2 = 0.913)

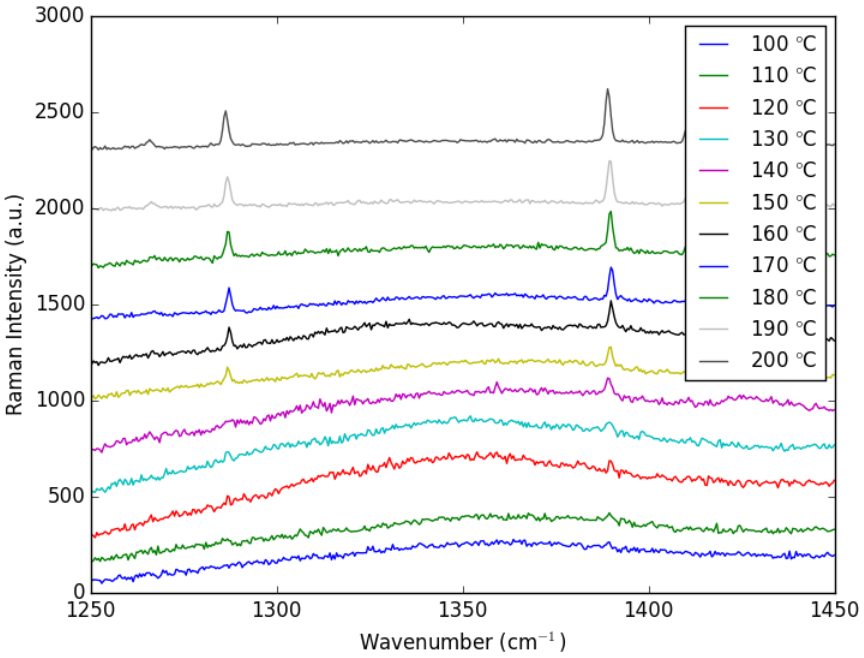

Figure 10.3: Raman Spectra of gas-phase CO_2 in headspace of capillary containing 30 wt% MEA at a loading of 0.30 mol CO_2/mol MEA

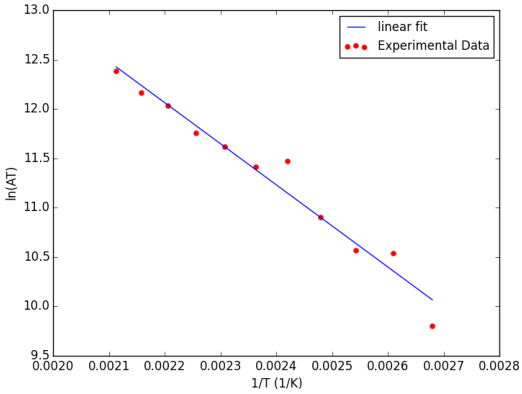

Figure 10.4: Data and linear regression used to determine heat of absorption for 30 wt% MEA with a loading of 0.30 mol CO_2/mol MEA (linear regression: y= -4162x + 21.22 with r^2 = 0.965)

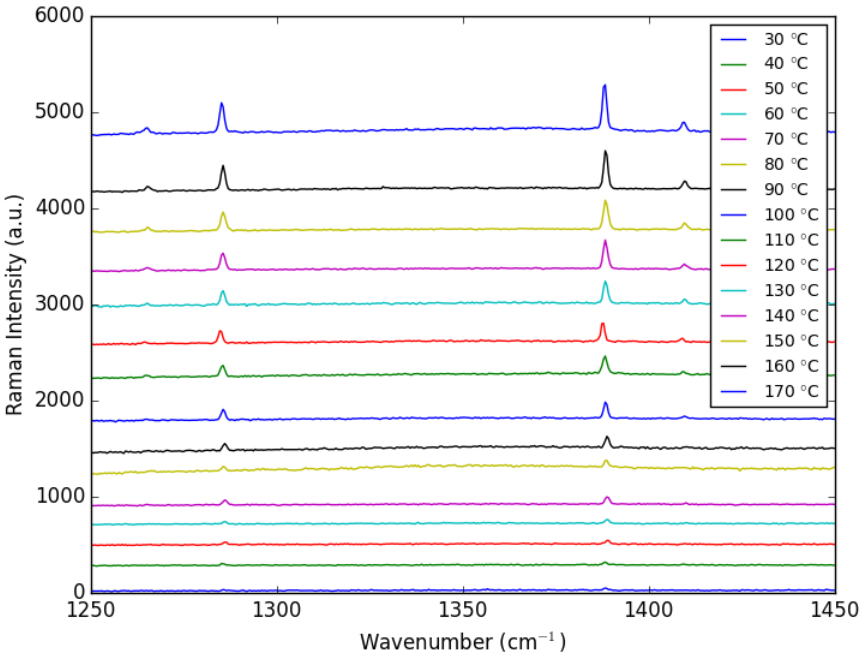

Figure 10.5: Raman Spectra of gas-phase CO_2 in headspace of capillary containing 30 wt% MEA saturated with CO_2

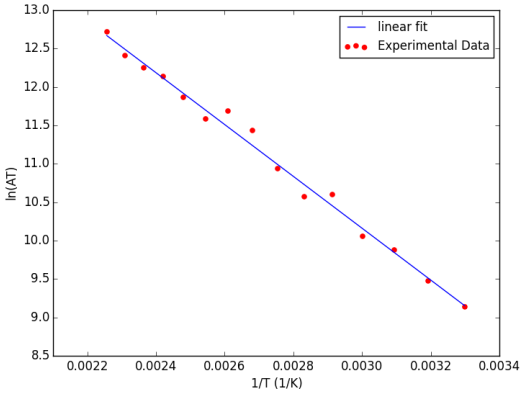

Figure 10.6: Data and linear regression used to determine heat of absorption for 30 wt% MEA saturated with CO_2 (linear regression: y= -3374x + 20.28 with $r^2 = 0.990$)